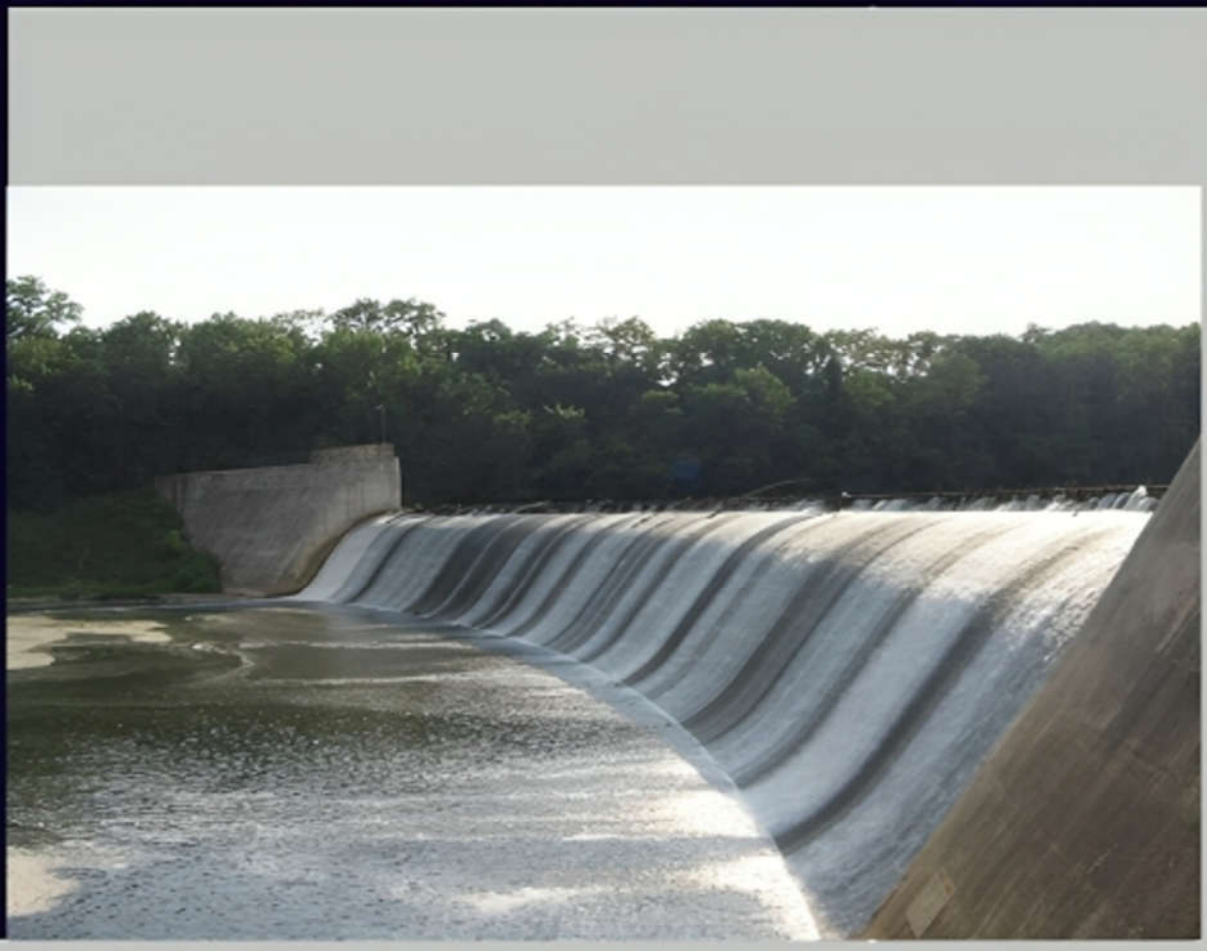
Iranian Hydraulic Association

Shahid Chamran University of Ahvaz

Journal of
Hydraulic Structures

Scientific Professional Journal



October 2026
Volume 12, Issue 4

ISSN (Online): 2345-4156
https://jhs.scu.ac.ir/

Aims and Scope

Journal of Hydraulic Structures is an interdisciplinary journal which publishes high-quality peer-reviewed articles addressing the latest developments and applied methods in analysis and design, construction, maintenance, management, and operation policy of Hydraulic Structures.

The Journal aims at providing an efficient route to fast-track publication, within 10-12 weeks after manuscript submission.

The general areas covered by the Journal include:

- Advances in numerical and analytical methods applicable to hydraulic structures
- Hydro informatics and soft computing
- Hydraulic aspects of hydraulic structures
- Applied surface and subsurface hydrology and hydrometeorology
- Forecasting approaches in water resources engineering
- Economic and social aspects of hydraulic structures
- Uncertainty analysis and risk management in hydraulics and water resources engineering
- Application of Nanotechnology in hydraulic structures
- Geotechnics of hydraulic structures
- Damage detection techniques
- Technical and methodological advances in application, design/selection, production, construction materials of hydraulic structures.
- Application of Artificial Intelligence techniques in all aspects of hydraulic structures.

General Information:

Title: Journal of Hydraulic Structures

Publisher: Shahid Chamran University of Ahvaz

ISSN (Print): 2345-413X

ISSN (Online): 2345-4156

Website: jhs.scu.ac.ir

Address: Faculty of Civil Engineering and Architecture, Shahid Chamran University of Ahvaz, Ahvaz, Iran

Email: jhs@scu.ac.ir

Journal of Hydraulic Structures

Department of Civil Engineering

Shahid Chamran University of Ahvaz

Journal of

Hydraulic Structures

Shahid Chamran University of Ahvaz

Director-in-Charge: Prof. Ali Haghighi

Editor-in-Chief: Prof. Hamid R. Ghafouri

Managing Editor: Dr. Amir H. Shafiee

Contents:

01

Local scour downstream of compound weirs under free and submerged flow conditions

Mohamed Abdelrazek Zidan; Ahmed Abouelfetouh; Ahmed Shwaky; Tarek Hemdan; Fahmy Abdelhaleem

14

Meander Bend Evolution and Bank Erosion Modeling of a reach of Brahmaputra River, India using MIKE 21C Model

Kuldeep Pareta; Upasana Pareta

42

Optimization of Static Operating Rule curves for Gated Spillways of Dams Under Flood Conditions

Mohammadreza Masoudimoghaddam; Saman Espahbodinia; Jafar Yazdi; Maedeh Behifar, Jamal Aghayari

60

Risk Analysis of Internal Erosion in Earth Dams Considering Uncertainties in the Permeability Coefficient of Materials

Samane Manafi; Jafar Yazdi

75

Experimental Investigation of Local Scour Around Twin Cylindrical Bridge Piers: Effects of Pier Spacing and Skew Angle

Morteza Shokri; AmirHossein Topal; Majid Fazli

91

Reduction of Scour Around Bridge Piers using Combined Cylindrical Protector and Riprap

Ferdous Mirsalari; Mahmood S. Bajestan; Seyed Mahmood Kashefipour; Mohammad Bahrami Yarahmadi; Kheirollah Khodemi

Local scour downstream of compound weirs under free and submerged flow conditions

Mohamed Zidan[1], Ahmed Abouelfetouh[2], Ahmed Shwaky[2], Tarek Hemdan[2], Fahmy Abdelhaleem[2]

1. Department of Civil Engineering, MISR High Institute for Eng. & Tech., Mansoura, Egypt, (C. O.).
2. Department of Civil Engineering, Benha Faculty of Engineering, Benha University, Benha, Egypt.

***Corresponding Author:**
Mohamed Zidan,

Email: mohamed.zidan9999@gmail.com
Received: 2025.01.02
Accepted: 2025.04.24
J. Hydraul. Struct., 2026; 12(4):1-13
DOI: 10.22055/jhs.2026.51451.1373

ABSTRACT

Local scour downstream of hydraulic structures poses a significant threat to bed stability in alluvial channels. This experimental study investigates the impact of compound weir geometry on flow dynamics and scouring characteristics. Four distinct cross-sectional configurations were tested Rectangular, Trapezoidal, Semicircular, and Triangular under varying hydraulic conditions and a constant discharge of 21 l/s. The results demonstrate that weir geometry plays a pivotal role in energy dissipation and jet trajectory. Among the primary shapes, the triangular configuration (127°) exhibited superior performance in mitigating downstream erosion compared to traditional rectangular designs. Furthermore, an optimization of the triangular apex angle was conducted, testing angles of 127°, 110°, 96° and 85°. The findings reveal that reducing the apex angle significantly enhances hydraulic control; the 85° triangular weir recorded the minimum scour depth of 4.8 cm, representing a 36% reduction compared to the 127° section. Strong correlations were established between the tailwater Froude number (Frt), longitudinal jet length (Ljet), and maximum scour depth (Zmax). These results suggest that optimizing the compound weir geometry to an 85° triangular shape provides a cost-effective and efficient strategy for bed protection in hydraulic engineering applications.

KEYWORDS

Energy dissipation, Local scour, Compound weirs, Sharp-crested weirs, Apex angle, Alluvial channels.

1. Introduction

Local scour in open channels represents a critical hydraulic phenomenon that significantly threatens the stability and longevity of water infrastructure. As emphasized by [1, 2], understanding the mechanics of sediment mobilization and scour development is paramount for the design of resilient and durable hydraulic structures. While early research established the fundamental principles of erosion, recent advancements have further elucidated the dynamics of this process. For instance, [3] demonstrated that local scour holes maintain a degree of shape similarity throughout their evolution, while [31] introduced modified prediction equations for scour parameters considering the impact of nonuniform sediment, which is essential for accurate field applications.

The dynamics of scour downstream of compound weirs are particularly complex, governed by a multifaceted interplay of variables. Geometry plays a pivotal role in this process; as noted by [6] and [13], the cross-sectional configuration significantly dictates the extent of scouring. To address these challenges, various mitigation and optimization strategies have been proposed. For instance, [27] demonstrated that optimizing trapezoidal labyrinth weir designs can enhance scour mitigation in straight channels. Other innovative configurations include combined triangular sharp-crested weirs with inverted V-shaped gates, as investigated by [28], and the use of slit weirs which provide unique discharge characteristics [32].

Energy dissipation and the influence of tailwater conditions are also crucial factors in controlling downstream bed morphology. [30] highlighted the effects of tailwater depth on scour cavity formation downstream of grade control structures, while [29] investigated the time evolution of scour characteristics downstream of sluice gates under submerged hydraulic jump conditions. Additionally, the use of structural features such as floor water jets [7, 8, 10, 25] and orifice-equipped gates [20, 26] has proven effective in improving hydraulic stability. Despite these extensive studies, a knowledge gap persists regarding the optimal geometric design of triangular compound weirs, particularly concerning the influence of the apex angle on scour minimization.

Despite the extensive literature on scour downstream of standard weirs, there is a notable lack of optimization studies focusing on the geometric apex angles of triangular compound configurations in alluvial channels. The primary objective of the current research is to fill this gap by experimentally investigating the hydrodynamic efficiency of four different compound weir shapes (Rectangular, Trapezoidal, Semicircular, and Triangular). Furthermore, this study aims to identify the optimum apex angle for triangular sections that minimizes downstream local scour. By providing a comparative analysis of flow patterns and bed morphology, this work offers practical design recommendations for more stable and cost-effective hydraulic structures.

2. Experimental Setup and Methodology

The experimental campaign was conducted at the Hydraulics and Irrigation Laboratory, Faculty of Engineering, Benha University, Egypt. All tests were carried out in a high-precision, tilting recirculating flume with a total length of 15.0 m, a width of 0.4 m, and a depth of 0.65 m. To ensure a fully developed, uniform flow distribution and to mitigate upstream turbulence, a gravel-filled stabilization box was strategically positioned at the flume's inlet. Flow depth and tailwater conditions were precisely regulated using a calibrated tailgate located at the flume's terminus. The discharge was maintained at a constant rate of 21 l/s, monitored via a pre-calibrated ultrasonic flow meter to ensure steady flow conditions during all experimental runs.

2.1. Test Section and Sediment Properties

The experimental models were installed at the flume’s midsection, approximately 7.0 m from the entrance. A movable sand bed section was established 1.0 m downstream of the weir structures, extending for a length of 3.0 m with a thickness of 0.25 m. The bed material consisted of non-cohesive sand characterized by a median particle size d_{50} of 0.8 mm, d_{90} of 1.95 mm, and a geometric standard deviation σ_g of 2.45. To eliminate the influence of sediment size on the scouring process and avoid scale effects, the ratio of channel width (D) to median grain size d_{50} was maintained at $D/d_{50} > 50$, in accordance with the criteria proposed by **Ettema (1980)**.

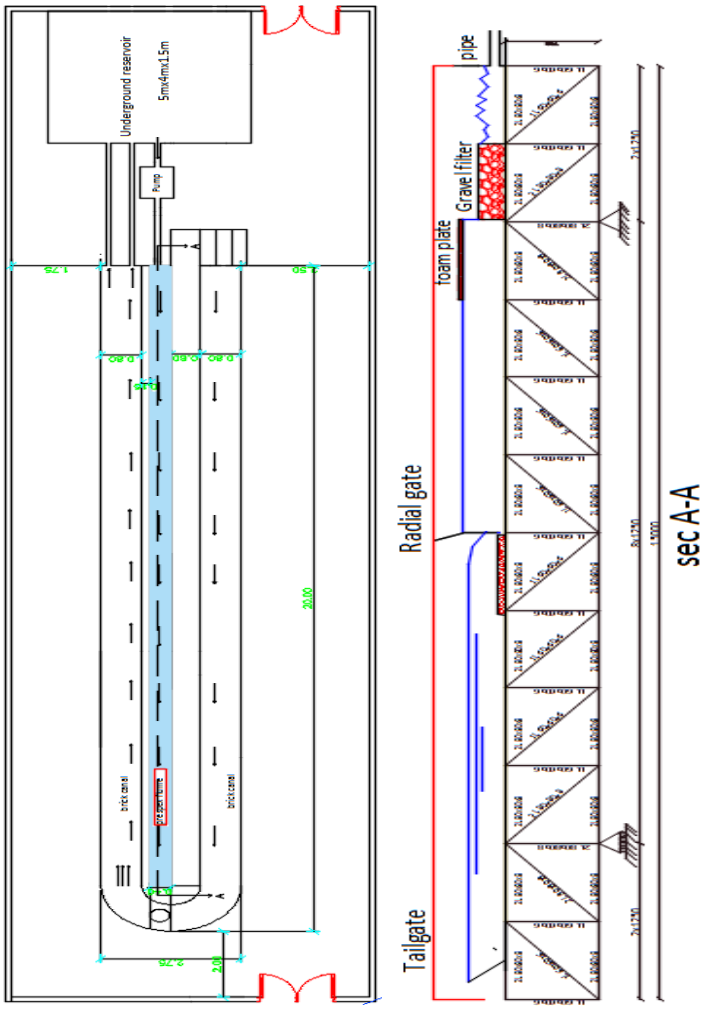


Figure 1. Layout of the experimental flume at Laboratory

2.2. Compound Weir Models and Stilling Basin

Four distinct geometric configurations of compound weirs were fabricated from high-quality timber and tested under a constant discharge of 21 l/s. Each weir was integrated with a 1.0 m long wooden stilling basin located immediately downstream. The tested geometries, as illustrated in **Figure (1)**, were designed as follows:

- **Shape (1) Rectangular (Rec.):** A primary rectangular section (26 cm wide, 10 cm deep) with the crest positioned 30 cm above the channel bed, superimposed over a smaller rectangular notch (10 cm wide, 5 cm deep).
- **Shape (2) Trapezoidal (Trap.):** The same primary rectangular section combined with a lower trapezoidal notch (top width 15 cm, bottom width 5 cm, and height 5 cm).
- **Shape (3) Semicircular (Cir.):** The primary rectangular section integrated with a lower semicircular opening (14 cm wide, 5 cm high).
- **Shape (4) Triangular (Tria.):** The primary rectangular section combined with a lower V-notch. This configuration was further investigated by varying the apex angle across four values: 127°, 110°, 96°, and 85°

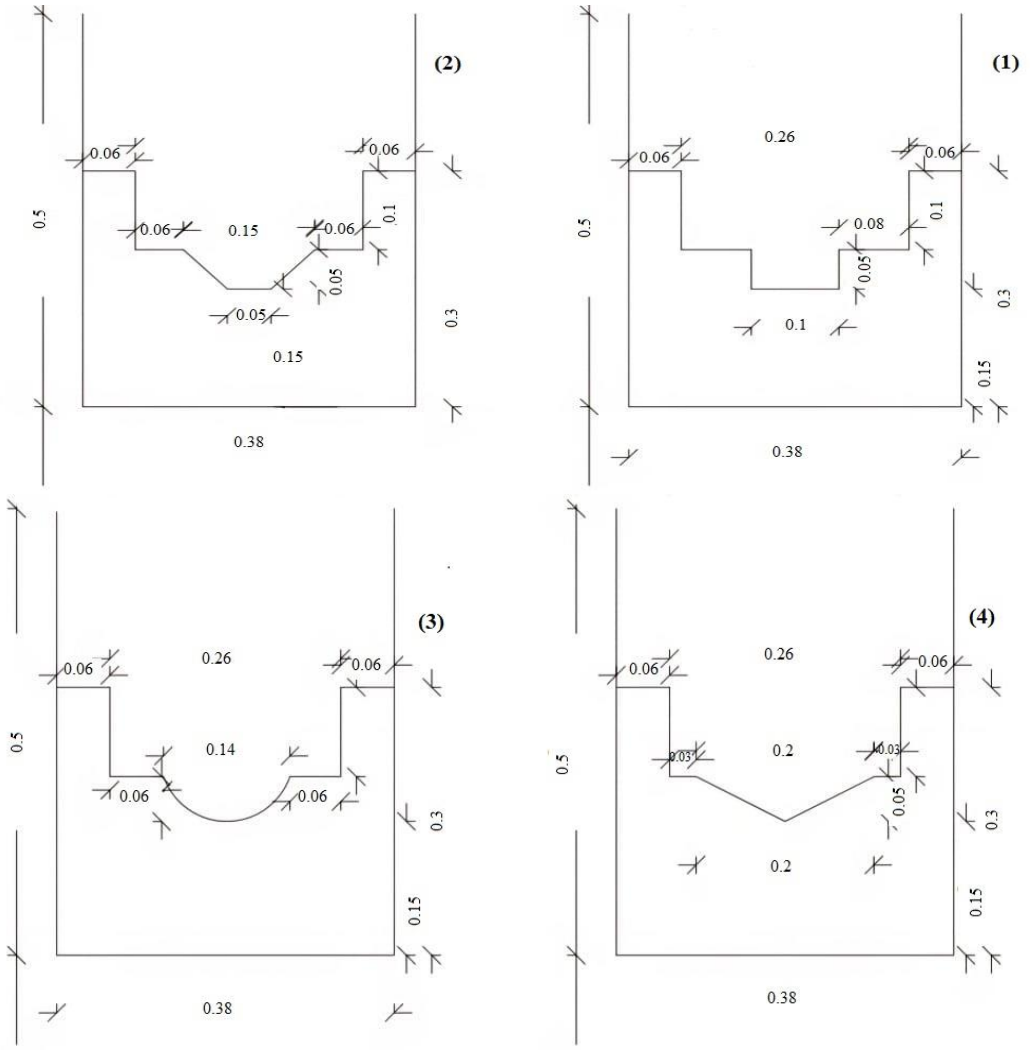


Figure 2. Different shapes of compound weirs

3. Theoretical Formulation (Dimensional analysis)

To generalize the experimental results and establish a functional relationship for the maximum scour depth (Z_{max}), dimensional analysis was performed using the **Buckingham π-theorem**. The maximum scour depth downstream of the compound weirs is influenced by several physical variables representing the fluid properties, flow conditions, sediment characteristics, and weir geometry:

$$Z_{max} = f\begin{pmatrix} V, y, \rho, \mu, g, \rho_S, D_{50}, \\ \sigma_g, B, b, h, \theta, Y_t, Ljet \end{pmatrix} \quad (1)$$

Where:

V = flow velocity; y = upstream flow depth; ρ= fluid density; μ = dynamic viscosity; g = gravitational acceleration; ρs = sediment density; d_{50} = median grain size; σ_g = geometric standard deviation of sediment; B = channel width; b = weir opening width; h = weir height; θ = apex angle; Yt= tailwater depth; and Ljet = longitudinal jet length.

By selecting ρ (density), V (velocity), and y (flow depth) as the repeating variables, the primary dimensionless groups (π -terms) were derived. After rearranging and combining these groups to reflect standard hydraulic parameters, the functional relationship is expressed as:

$$\frac{Zmax}{y} = f\left(Fr, Re, \frac{\rho s}{y\rho}, \frac{d50}{y}, \sigma_g, \frac{b}{h}, \frac{B}{y}, \theta, \frac{Yt}{y}, \frac{Ljet}{y}\right) \quad (2)$$

3.1. Simplification of the Functional Relationship

To refine the analysis and focus on the most influential parameters, several simplifications were applied:

- **Viscous Effects:** The Reynolds number (Re = ρVy/ μ) was neglected as the flow in the flume is characterized by high turbulence (Re > 10^4) where inertial forces dominate.
- **Sediment Properties:** Since a consistent soil sample was used (σ_g = 2.45), the density ratio (ρ_s/ρ) and sediment grading remained constant and were excluded from the variable parameters.
- **Geometric Constants:** The channel width (B) and median grain size (d_{50}) were constant throughout the experiments.

The final simplified non-dimensional relationship used for the analysis is:

$$\frac{Zmax}{y} = f\left(\mathrm{Fr_t}, \theta, \frac{b}{h}, \frac{Yt}{y}, \frac{Ljet}{y}\right) \quad (3)$$

Where:

- **$\mathbf{Fr_t = V/\sqrt{gy}}$:** Tailwater Froude number (representing inertial vs. gravitational forces).
- **$\mathbf{Z_{max}/y}$**: Relative maximum scour depth.
- **$\boldsymbol{\theta}$** : Apex angle (for triangular configurations).
- **$\mathbf{Y_t/y}$**: Relative tailwater depth (submergence ratio).
- **$\mathbf{L_{jet}/y}$**: Relative longitudinal jet length.

4. Results and Discussion

The experimental measurements were systematically recorded for all weir configurations. Table(1) presents a representative sample of the collected data and calculated dimensionless parameters for the trapezoidal compound weir, while the complete comparative analysis is illustrated in the subsequent figures.

Table 1. Experimental data and dimensionless parameters for the trapezoidal compound weir.

Trapezoidal section						
Y_u (cm)	Y_t(cm)	L_{jet}(cm)	Z_{max}(cm)	Fr_t	L_{jet}/Y_t	Z_{max}/Y_t
31	22	16	7	0.162439	0.727273	0.318182
31	20	17.4	6.8	0.187404	0.87	0.34
31	18.5	18.6	7.1	0.210653	1.005405	0.383784
31	17	19	7.2	0.23914	1.117647	0.423529
31	16	19.5	7.4	0.261906	1.21875	0.4625
31	14.5	20.9	7.5	0.30358	1.441379	0.517241
31	13.5	22.5	7.7	0.337928	1.666667	0.57037
31	12	23	8	0.40323	1.916667	0.666667
31	10.5	24.2	8.9	0.492653	2.304762	0.847619
31	9	25.5	9	0.620813	2.833333	1

4.1. Influence of Compound Weir Geometry on Relative Scour Depth

The impact of varying compound weir geometries specifically rectangular, trapezoidal, semicircular, and triangular (127°) on the relative maximum scour depth Z_{max}/Y_t is illustrated in Figure (2). The experimental results demonstrate a direct correlation between the tail Froude number Fr_t and the relative scour depth; as Fr_t increases, the erosive power of the flow intensifies, leading to a deeper scour hole.

Notably, at lower Fr_t values, the difference in scour depth between the four shapes is minimal, with the results converging as the flow remains relatively stable. However, as the Fr_t rises (indicating higher inertial forces), the geometric configuration of the weir becomes a dominant factor in governing the scour morphology.

- **Rectangular Configuration:** Conversely, the rectangular weir produced the maximum relative scour depth. The abrupt edges of the rectangular section likely induce greater local turbulence and stronger vortices, which accelerate the sediment removal process downstream.
- **Trapezoidal and Semicircular Shapes:** These configurations exhibited intermediate performance, with their scour depth values converging as Fr_t increased, suggesting a similar degree of hydraulic resistance and turbulence induction.

As illustrated in **Figure 3**, a consistent increase in the relative maximum scour depth (Z_{max}/Y_t) is observed with the increment of the tail Froude number (Fr_t). This is attributed to the enhanced kinetic energy and turbulence intensity associated with higher flow velocities. Notably, the triangular configuration effectively mitigates the erosive impact by promoting a more concentrated and streamlined flow transition, which leads to better energy dissipation compared to the abrupt edges of the rectangular weir.

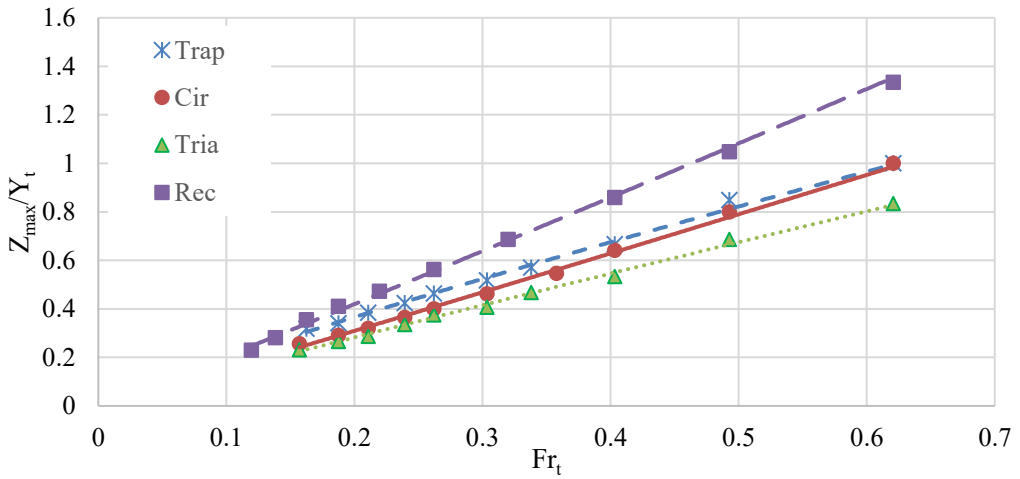


Figure 3. Relationship between relative scour depth (Z_{max}/Y_t) and tail Froude number (Fr_t) for different shapes of compound weirs

Key observations from the data include:

- **Triangular Configuration (127°):** This shape consistently yielded the minimum relative scour depth Z_{max}/Y_t across all high-velocity runs. This performance can be attributed to the triangular geometry's ability to promote smoother flow transitions and potentially more effective energy dissipation compared to other shapes.

4.2. Influence of Weir Geometry on the Relative Length of Jet

The characteristic behavior of the relative jet length L_{jet}/Y_t as a function of the tail Froude number Fr_t for the four investigated weir configurations is depicted in Figure (4). Consistent with hydraulic principles, an increase in Fr_t results in a corresponding expansion of the relative jet length across all geometries. This trend is driven by the increased kinetic energy and momentum associated with higher flow velocities.

Similar to the observations made for scour depth, the influence of the weir's cross-sectional shape becomes significantly more pronounced and divergent at higher Fr_t values. At lower flow intensities, the hydraulic response of the different shapes tends to converge, suggesting that geometric nuances have a diminished impact under subcritical or low-velocity conditions.

The comparative analysis reveals distinct performance patterns:

- **Triangular Configuration (127°):** This geometry achieved the minimum relative jet length L_{jet}/Y_t. The triangular notch appears to facilitate a more controlled energy dissipation and a more concentrated flow distribution, which effectively limits the longitudinal extent of the jet.
- **Rectangular Configuration:** Conversely, the rectangular weir produced the maximum relative jet length. This is likely due to the uniform crest width which allows a broader, less-obstructed flow sheet to travel further downstream before dissipating its energy.
- **Circular and Trapezoidal Sections:** The data shows that the values for circular and trapezoidal sections tend to converge at higher flow intensities, following an intermediate path between the rectangular and triangular extremes.

The experimental results depicted in **Figure 4** indicate a positive correlation between the tail Froude number (Fr_t) and the relative jet length (L_{jet}/Y_t). As (Fr_t) increases, the kinetic energy of the flow over the compound weir intensifies, propelling the jet further downstream before it strikes the channel bed. It is observed that the **Triangular configuration** (127°) produces the shortest jet length, which suggests a higher rate of internal energy dissipation within the weir structure itself. In contrast, the **rectangular weir** allows for a broader, less obstructed flow, resulting in the maximum longitudinal extent of the jet. Minimizing the jet length is a critical design objective, as a shorter jet reduces the footprint of the stilling basin required and concentrates the energy dissipation closer to the structure, thereby protecting the downstream reach from extensive local scour.

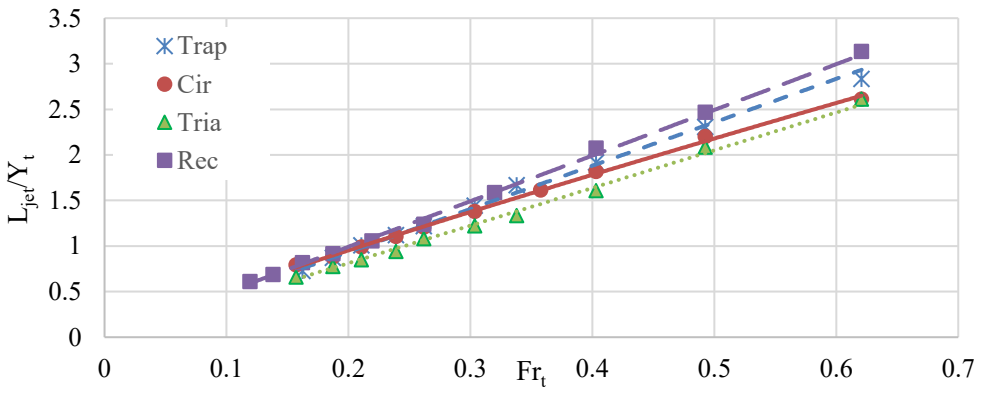


Figure 4. Relationship between relative length of jet (L_{jet}/Y_t) and tail Froude number (Fr_t) for different shapes of compound weirs

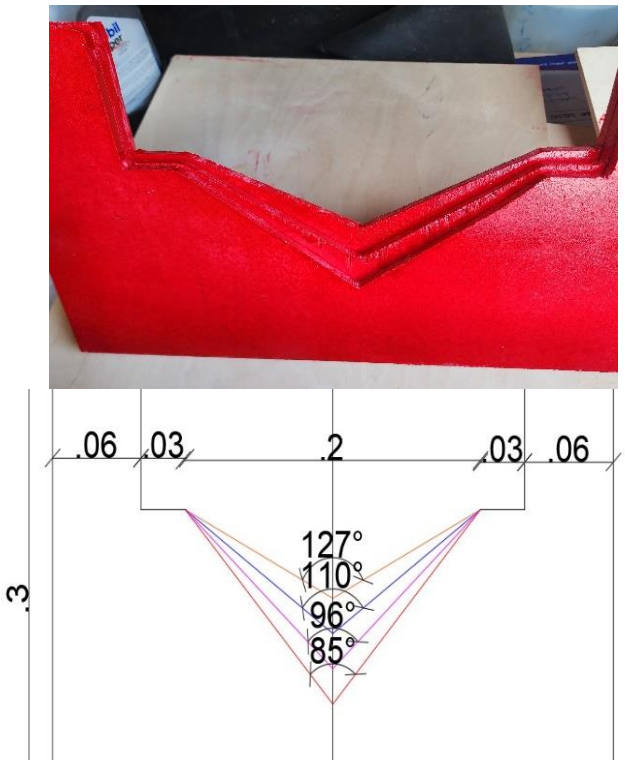


Figure 5. Different angles of triangular compound weir

4.3. Effect of Triangular Apex Angle on Relative Scour Depth

The influence of the triangular apex angle on the relative maximum scour depth Z_{max}/Y_t is analyzed in Figure (6). Four distinct angles (127°, 110°, 96°, and 85°) were tested across a range of tail Froude numbers Fr_t at a constant discharge of 21 l/s. Consistent with previous observations, an upward trend in Fr_t correlates with a systematic increase in Z_{max}/Y_t for all apex angles.

The results indicate that the sensitivity of the scour depth to the apex angle is highly dependent on the flow regime. At lower Fr_t values, the scour depths for all four angles converge, suggesting that geometric variations have a negligible impact under low-velocity conditions. However, a significant divergence occurs at higher Fr_t values, where the hydraulic efficiency of the triangular notch becomes more apparent.

Key findings from the angular analysis include:

- **The 85° Apex Angle:** This configuration yielded the minimum relative scour depth Z_{max}/Y_t throughout the high-velocity experimental runs. The narrower angle (85°) likely provides a more gradual flow transition and higher energy dissipation efficiency, which in turn reduces the intensity of the downstream turbulence responsible for bed erosion.
- **The 127° Apex Angle:** Conversely, the widest angle (127°) resulted in the maximum relative scour depth. As the apex angle increases, the weir behavior begins to approach that of a rectangular configuration, leading to a broader jet and more aggressive scouring.
- **Effect of Angle Reduction:** It is evident that decreasing the apex angle of the triangular section leads to a proportional reduction in Z_{max}/Y_t. This suggests that sharper triangular profiles are superior for protecting the channel bed from localized erosion.

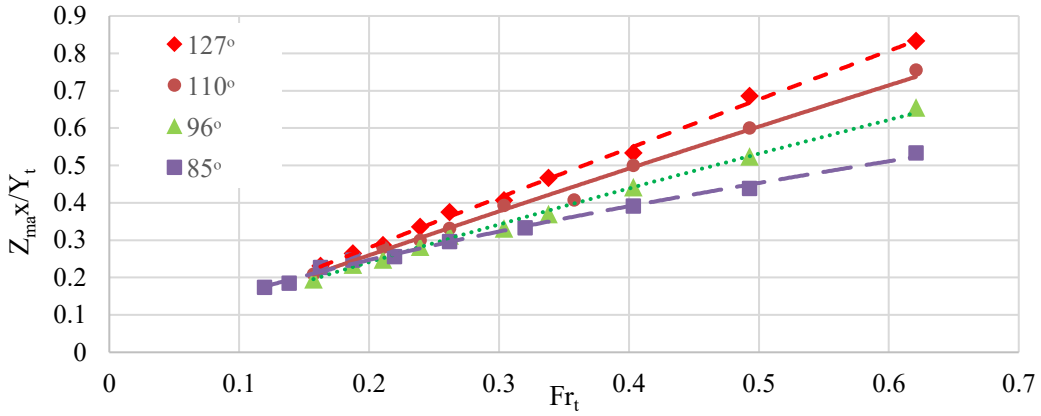


Figure 6. Relationship between relative scour depth (Z_{max}/Y_t) and tail Froude number (Fr_t) for different angles of triangular compound weir

A detailed comparison between different apex angles of the triangular weir is presented in **Figure 6**. The results demonstrate a significant reduction in the relative scour depth as the apex angle decreases. Specifically, the **85° triangular weir** exhibited the most superior performance, achieving a reduction in local scour by approximately **36%** compared to the 127° angle. This phenomenon can be physically explained by the Jet Concentration effect; a sharper apex angle 85° forces the flow into a narrower, more vertical jet structure. This concentration promotes a more controlled impact on the channel bed and increases the air entrainment, which significantly dissipates the flow's erosive energy before it reaches the alluvial bed. Consequently, the 85° angle provides a more stable hydraulic condition, making it the most effective geometric configuration for protecting downstream reaches in alluvial channels.

4.4. Effect of Triangular Apex Angle on the Relative Length of Jet

The relationship between the relative length of the jet L_{jet}/Y_t and the tail Froude number Fr_t for various triangular apex angles is presented in Figure (7). A consistent trend is observed where the relative jet length increases proportionally with Fr_t across all tested angles (85°, 96°, 110°, and 127°).

At lower flow intensities low Fr_t, the values of L_{jet}/Y_t tend to converge, indicating that the geometric variations of the triangular notch have a limited impact on the jet trajectory under tranquil flow conditions. Conversely, as Fr_t increases, a significant divergence occurs, highlighting the sensitivity of the jet's longitudinal extent to the weir's apex angle.

Key insights from this analysis include:

- **The 85° Apex Angle:** This configuration consistently yielded the minimum relative jet length. The narrower apex angle promotes a more streamlined and hydraulically efficient discharge, which effectively dissipates energy more rapidly and limits the downstream reach of the jet.
- **The 127° Apex Angle:** This wider angle produced the maximum relative jet length, as the flow behavior begins to mimic a wider rectangular crest, allowing the jet to maintain its momentum over a greater distance.
- **Physical Justification:** It is evident that decreasing the apex angle of the triangular section optimizes the flow concentration. By narrowing the flow passage, the weir enhances the hydraulic control over the discharging jet, thereby reducing its relative length and, consequently, its erosive potential on the downstream bed.

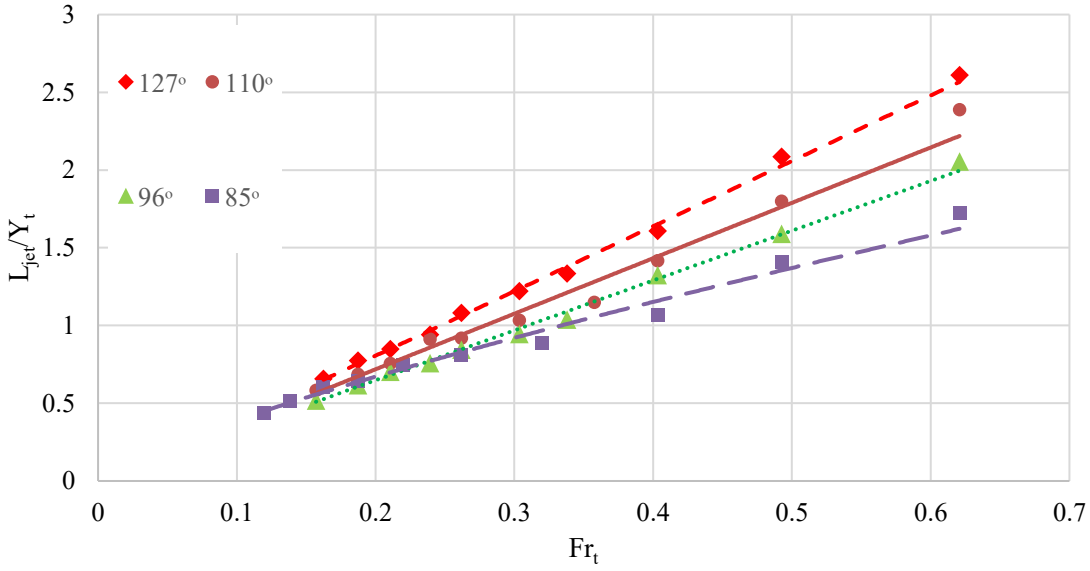


Figure 7. Relationship between relative length of jet (L_{jet}/Y_t) and tail Froude number (Fr_t) for different angles of triangular compound weir

The spatial characteristics of the scour hole, specifically the relative scour length (L_{jet}/Y_t), are illustrated in **Figure 7** for varying apex angles. The data reveals that the **85° triangular weir** not only minimizes the scour depth but also significantly restricts the longitudinal extent of the scour hole. This localized scouring pattern is a direct result of the improved flow alignment and the reduced turbulence at the bed-water interface. By confining the scour hole to a smaller area, the 85° configuration ensures higher structural stability for the channel bed and reduces the volume of eroded sediment that could be deposited further downstream. This comprehensive reduction in both scour depth and length confirms that optimizing the weir geometry to an 85° triangular shape is a highly effective strategy for sustainable sediment management in alluvial streams.

5. Conclusions

- **Flow Dynamics and Scour:** A strong correlation was established between tailwater conditions and scour morphology. The results indicate that the maximum scour depth (Z_{max}) and longitudinal jet length (L_{jet}) are highly sensitive to the tailwater Froude number (Fr_t).
- **Geometric Influence:** The cross-sectional geometry plays a pivotal role in energy dissipation. The rectangular configuration (traditional shape) exhibited the lowest hydraulic efficiency, resulting in the most aggressive scour profiles.
- **Superiority of the Triangular Section:** Among the primary shapes tested, the triangular compound weir (127°) proved to be the most effective in minimizing downstream erosion compared to rectangular, trapezoidal, and semicircular designs.
- **Optimization of the Apex Angle:** The apex angle is a critical design parameter. Reducing the angle significantly enhances hydraulic control; the **85° angle** recorded the absolute minimum scour depth (4.8 cm), achieving a **36% reduction** compared to the 127° section.
- **Design Implications:** To ensure adequate bed protection, the stilling basin length must be proportionally adjusted based on the predicted jet length, which increases with higher Froude numbers.

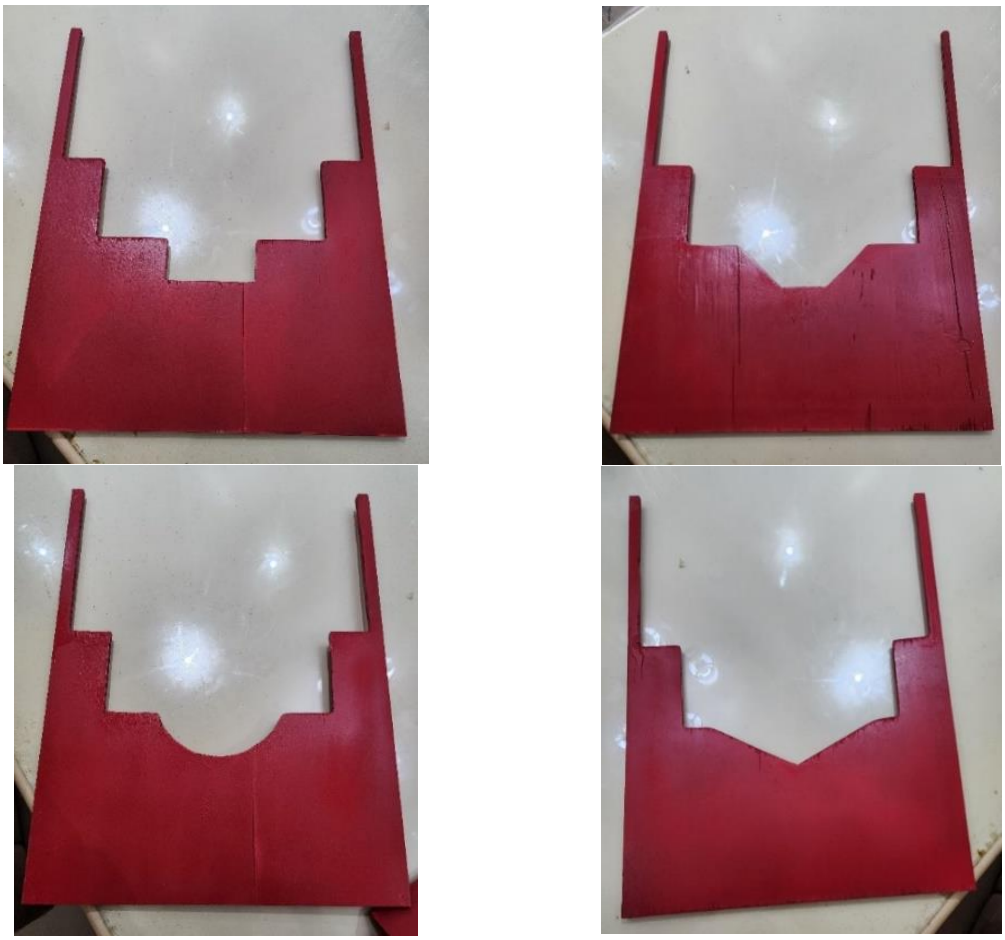


Figure 8. Different models of compound weirs



Figure 9. Different shapes of experimental works

6. Recommendations for Future Research

- While this study optimizes the geometric shape of compound weirs, the following areas are suggested for further exploration:
- **Sediment Diversity:** Evaluating these optimized geometries in cohesive soils and graded sediment beds to assess the universality of the 85° apex angle.
- **Hybrid Mitigation Measures:** Investigating the combined effect of the 85° triangular weir with floor jets or baffle blocks to further enhance scour reduction.
- **Numerical Modeling (CFD):** Utilizing 3D Computational Fluid Dynamics (CFD) to visualize the complex turbulence structures and vortex dynamics, facilitating the scaling of these results to full-scale prototypes.

Declarations

- **Conflict of Interest:** The authors declare that they have no known competing financial interests or personal relationships that could have appeared to influence the work reported in this paper.
- **Funding:** This research did not receive any specific grant from funding agencies in the public, commercial, or not-for-profit sectors**.**
- **Data Availability Statement:** The data that support the findings of this study are available from the corresponding author upon reasonable request.
- **Authors' Contributions:** All authors contributed equally to the conceptualization, methodology, and writing of the original draft

6. References

1. Raudkivi AJ, Ettema R. Clear-water scour at cylindrical piers. Journal of Hydraulic Engineering. 1983;109(3):338-50.
2. Raudkivi AJ. Functional trends of scour at bridge piers. Journal of Hydraulic Engineering. 1986;112(1):1-13.
3. Li J, Qi M. Local scour induced by upstream riverbed level lowering. Natural Hazards. 2015;77:1811-27.
4. Azmi S, Zakwan M. Data Specific Pier Scour Predictors. In: Proc. 3rd Nat. Con. on Sustain. Water Resour. Dev. and Manag., Aurangabad. 2016. p. 326-9.
5. Wu W, Xu Y, He S. Numerical Investigation of Bridge Pier Scour Processes under Steady Flow Conditions. Water Resources Management. 2020;34(14):3809-22.
6. Sharafati A, Haghbin M, Haji Seyed Asadollah SB, Tiwari NK, Al-Ansari N, Yaseen ZM. Scouring depth assessment downstream of weirs using hybrid intelligence models. Applied Sciences. 2020;10(11):3714.
7. Abdelhaleem F. Effect of semi-circular baffle blocks on local scour downstream clear-overfall weirs. Ain Shams Engineering Journal. 2013;4:675-84.
8. Helal E. Minimizing scour downstream of hydraulic structures using single line of floor water jets. Ain Shams Engineering Journal. 2014;5:17-28.
9. Ibrahim MM. Bed profile downstream compound sharp crested V-notch weir. Alexandria Engineering Journal. 2015;54:607-13.
10. Amin A. Physical model study for mitigating local scour downstream of clear over-fall weirs. Ain Shams Engineering Journal. 2015;6:1143-50.
11. Eltoukhy M, Ibrahim M. Velocity Distribution Downstream Compound Weirs. Aust. J. Basic & Appl. Sci. 2015;9(1):238-45.
12. Omran HA, Khassaf SI, Hassan FA. The effect of flow conditions and geometric parameters on the scour value downstream composite structures of Weir and gate. Kufa J. Eng. 2016;7(1):115-28.
13. Jüstrich S, Pfister M, Schleiss A. Mobile Riverbed Scour Downstream of a Piano Key Weir. Journal of Hydraulic Engineering. 2016;142:04016043.
14. Guan D, Melville B, Friedrich H. Local scour at submerged weirs in sand-bed channels. Journal of Hydraulic Research. 2016;54:172-84.
15. Khassaf S, Omran H, Abdulabbas F. The relationship between the coefficient of discharge and the scour hole depth generated due to the combined flow over weir and below gates. MATEC Web of Conferences. 2018;162:03010.
16. Karthik R, Kumar U, Barbhuiya AK. Two-

Dimensional Analysis of Flow Field and Associated Scour Parameters at Downstream of Weir with and without Sloping Apron. International Journal of Engineering and Advanced Technology (IJEAT). 2019.
17. Guan D, Liu J, Chiew Y, Zhou Y. Scour Evolution Downstream of Submerged Weirs in Clear Water Scour Conditions. Water. 2019.
18. Verdugo J, Torres B, Ayala M. Experimental Study of Scouring Downstream of Weirs. In: 38th IAHR World Congress - "Water: Connecting the World". 2019.
19. Eltoukhy M, Abdelhaleem FS, Nasralla TH, Shaban S. Effect of Compound Weir and below Circular Gate Geometric Characteristics on its Discharge Coefficient. International Journal of Scientific & Engineering Research. 2020;11(10).
20. Ibrahim M, Abdelhaleem F. Flow downstream sluice gate with orifice. KSCE J. Civ. Eng. 2020;24(12):3692-702.
21. Suleiman S, Ismael A. Predicting the scour depth downstream single step broad crested weirs. Journal of Physics: Conference Series. 2021;1973.
22. El-Mahdy ME. Experimental method to predict scour characteristics downstream of stepped spillway equipped with V-Notch end sill. Alex. Eng. J. 2021;60(5):4337-46.
23. Kurdistani SM, Varaki ME, Larsari ZK. Scour downstream of stepped-baffle weirs in wide rivers. Sådhanå. 2022;47:178.
24. Lantz W, Crookston B, Palermo M. Evolution of local scour downstream of Type APK weir in non-cohesive sediments. Journal of Hydrology and Hydromechanics. 2022;70:103-13.
25. Elsaeed G, Ali AM, El-Hazek AN, Ibraheem MM. Influence of Using Floor Jets on the Local Scour Downstream Fayoum Type Weir. Asian Journal of Engineering and Technology. 2020;08(01).
26. Namadian B, Asadi E. Investigation of temporal variations of scour depth in combined weir-gate structure using FLOW-3D numerical model. Iranian Journal of Irrigation & Drainage. 2022;16(2):432-45.
27. Shehata, A. H., Youssef, T. F., Hamada, H. A., M, I. M., and Samy, A. (2024). Optimizing Trapezoidal Labyrinth Weir Design for Enhanced Scour Mitigation in Straight Channels. *Water*, *16*(17), 2443
28. Diwedar, A. I., Mamdouh, L., and Ibrahim, M. M. (2022). Hydraulics of combined triangular sharp crested weir with inverted V-shaped gate. *Alexandria Engineering Journal*, *61*(10), 8249-8262.
29. Mahdian Khalili, A., and Hamidi, M. (2023). Time evolution effect on the scour characteristics downstream of the sluice gate with the submerged hydraulic jump in a laboratory model. *Journal of Hydraulic Structures*, *9*(2), 32-47.
30. Bagherzadeh, M., Mohammadi, M., and Ghaderi, A. (2025). Experimental investigation of the effects of tailwater depth on scour cavity formation downstream grade control structures. *Acta Geophysica*, *73*(6), 5991-6004.
31. Mahdian Khalili, A., and Hamidi, M. (2026). Modified prediction equations for scour parameters downstream of sluice gates considering nonuniform sediment. *Acta Geophysica*, *74*(1), 19.
32. Sohrabzadeh Anzani, H., Kantoush, S. A., Mahdian Khalili, A., and Hamidi, M. (2024). Experimental investigation of slit weir discharge. *ISH Journal of Hydraulic Engineering*, *30*(5), 645-654.

© 2025 by the authors. Licensee SCU, Ahvaz, Iran. This article is an open access article distributed under the terms and conditions of the Creative Commons Attribution 4.0 International (CC BY 4.0 license) (http://creativecommons.org/licenses/by/4.0/).

Meander Bend Evolution and Bank Erosion Modeling of a reach of Brahmaputra River, India using MIKE 21C Model

Kuldeep Pareta [1], Upasana Pareta [2]

1. DHI (India) Water & Environment Pvt. Ltd. Unit No. 339, Eighth Floor DLF Prime Tower. Okhla Phase-I, New Delhi - 110020. India.
2. Omaksh Consulting Pvt Ltd. D-632, 7th Avenue, Gaur City-1 Greater Noida, UP.

***Corresponding Author:**
Kuldeep Pareta

Email: kupa@dhigroup.com
Received: 2025.02.03
Accepted: 2025.05.25
J. Hydraul. Struct., 2026;12(4):14-41
DOI: 10.22055/jhs.2026.51623.1376

ABSTRACT

Riverbank erosion and rapid channel migration in large braided alluvial rivers such as the Brahmaputra pose substantial risks to infrastructure, settlements, and ecological systems. This study applies a high-resolution two-dimensional hydrodynamic and morphodynamic modeling framework to investigate meander bend evolution and bank erosion processes in an actively migrating reach near Palasbari, India. Simulations under bankfull and extreme flood conditions reveal pronounced hydraulic asymmetry within the bend, with peak velocities reaching 4.83 m s^{-1}, flow depths exceeding 65 m, and significant secondary circulation generating localized reverse flows greater than 3 m s^{-1}. These high-energy conditions produced deep local scour (>30 m) along the southern outer bank, confirming its high susceptibility to erosion during frequent and extreme flood events. Scenario-based intervention analysis demonstrates that sediment-guided realignment-through dredging of the mid-channel bar and strategic sediment placement along the outer bend-effectively reduces near-bank flow intensity and secondary currents, thereby lowering erosion potential. In contrast, structural flow deflectors intensified reverse flow zones and increased local instability, highlighting the risks associated with poorly evaluated engineering measures. The findings provide new process-based insights into meander morphodynamics under extreme hydraulic forcing and demonstrate the value of integrated hydrodynamic–morphodynamic modeling for evaluating erosion mitigation strategies. The study underscores the importance of adaptive, sediment-oriented river management approaches for sustaining morphological stability in highly dynamic alluvial systems such as the Brahmaputra River.

KEYWORDS

River morphology, erosion forecast, sediment transport, Brahmaputra River, MIKE 21C

1. Introduction

River morphodynamics refers to the interdisciplinary study of the physical processes that govern the evolution of river channels over time, driven by the complex interplay between water flow (hydrodynamics), sediment transport mechanisms, and channel bed and bank morphology [1, 2]. This field integrates principles of fluid mechanics, sedimentology, and geomorphology to understand how rivers respond to natural and anthropogenic forcings across varying spatial and temporal scales [3, 4]. Among river types, braided rivers exhibit the most dynamic morphodynamic behavior due to their network of multiple interlacing channels separated by transient mid-channel bars or islands [5, 6, 7].

These rivers are typically associated with high sediment supply, steep gradients, and variable discharge regimes, which together facilitate frequent channel avulsions, lateral migration, and bar formation or erosion [8, 9]. The inherent instability of braided systems makes them particularly sensitive to fluctuations in flow magnitude, sediment availability, and boundary conditions such as bank erodibility or vegetation cover [10, 11, 12]. Consequently, predicting morphological changes in these systems is a complex task with significant implications for river engineering, infrastructure resilience (e.g., bridge piers, embankments), flood risk management, and habitat conservation [13, 14, 15].

The Brahmaputra River exhibits highly dynamic hydro-sedimentary processes characterized by intense and recurrent channel migration, lateral bank erosion, and floodplain reconfiguration -phenomena that define its morphodynamic behavior [16, 17, 18]. The braided nature of the channel, with constantly shifting mid-channel bars and anastomosing threads, further compounds the river's unpredictability [19]. Satellite imagery observations and field surveys have reported riverbank erosion rates in the Brahmaputra River exceeding 72 m/year in certain reaches, causing significant land loss, population displacement, and damage to infrastructure [20, 21, 22]. Given the Brahmaputra's role in supporting densely populated floodplains, agrarian livelihoods, and key transport corridors, a robust understanding of its morphodynamics is imperative for sustainable river basin management [23, 24, 25, 26]

Historically, river morphodynamics were assessed using empirical techniques and 1D hydraulic models such as HEC-RAS or MIKE+, which, while foundational, are inherently limited in representing the spatial complexity and lateral variability of large braided rivers [11, 27, 28, 29, 30, 31, 32]. Empirical methods often rely on steady-state assumptions and uniform geometries that do not reflect the dynamic, non-linear nature of rivers like the Brahmaputra [33, 34].

Moreover, 1D models, which simulate flow along a longitudinal profile, fail to capture critical morphological processes such as bar formation, bifurcation, eddy formation, and localized bank erosion [10, 35, 36]. These limitations have led to the adoption of two-dimensional (2D) and three-dimensional (3D) models that provide spatially distributed and temporally responsive simulations of sediment dynamics, hydraulic flow, and morphological evolution [37, 38, 39, 40, 41, 42]. Among these, MIKE 21C - developed by DHI - has proven effective for braided and meandering rivers, offering advanced capabilities through its curvilinear orthogonal grid system, which conforms to natural river planforms and enhances model accuracy [43, 44, 45]. MIKE 21C integrates Saint-Venant equations with sediment continuity modules to simulate bed level changes, bar migration, lateral erosion, and sediment partitioning [46, 47, 48, 49, 50]. The model accounts for multiple sediment fractions and bank erosion processes driven by hydraulic shear and has been successfully applied in sediment-rich rivers such as the Brahmaputra, Ganges, and Mekong to support flood risk mitigation, river training design, and long-term morphological forecasting [32, 51, 52, 53].

Two-dimensional (2D) hydrodynamic and morphological modeling tools have proven highly effective for simulating sediment transport, erosion, and channel dynamics across varied riverine and coastal environments. Ramakrishnan [54] utilized the MIKE 21 Mud Transport model in the Gulf of Kachchh, leveraging Oceansat OCM-derived SSC to drive sediment simulations. The study emphasized the importance of tuning parameters such as settling velocity and critical shear stress based on sediment characteristics, revealing the spatial variability driven by tidal currents and seabed morphology. Morianou [43] applied MIKE 21C in the Koiliaris River and successfully reproduced water

levels and sediment transport using high-resolution DEMs and field data. Similarly, Dang [55] demonstrated the robustness of MIKE 21C in the lower Mekong River, capturing seasonal variations and sediment processes with strong calibration performance. In the Brahmaputra River, Karmaker [56] used a 2D model to simulate short-term morphological changes, validating thalweg shifts and evaluating groyne field effectiveness in braided systems. Morianou [57] extended these models to climate impact studies, highlighting that projected increases in rainfall could exacerbate bank erosion. Wang [58] modelled unsteady urban river flows using MIKE 21 FM, showing how cross-sectional irregularities affect hydraulic performance and flood risk. Pareta [59] applied MIKE 21C for predicting morphological evolution in the Brahmaputra, validating simulations with ADCP and flood-level data. These applications collectively highlight the reliability of 2D models in representing complex hydraulic and sediment transport processes for both natural and anthropogenic scenarios.

Recent studies have expanded the use of integrated 1D-2D modeling systems to improve sediment transport predictions and river management strategies. Pareta [32] developed a comprehensive framework combining MIKE Hydro River, MIKE 21 FM, and MIKE 21C to simulate hydrodynamic and sediment transport processes in the Banshadhara River. The model achieved high accuracy (98.3% for water levels, 86.7% for sediment transport), using the Wilcock & Crowe formula for gravel-bed conditions. The simulations revealed bend-induced erosion zones and spatially variable flow dynamics, supporting effective flood risk and channel migration assessments. In the sediment-laden Brahmaputra River, Pareta [53] further employed MIKE 21C to forecast morphological evolution. Validation with ADCP observations confirmed the model's reliability in scenario-based erosion prediction and design of training works. Le [60] assessed coastal morphological responses to breakwaters in the Mekong Delta using MIKE 21 FM, illustrating how optimized breakwater configurations enhance sediment deposition and shoreline stabilization. Sarker [61] combined 1D and 2D techniques to distinguish floodplain from channel flows, improving risk analysis in low-gradient terrains. Samir [62] modelled flow disruptions during bridge rehabilitation on the Nile, showing that reduced cross-sectional areas can alter hydrodynamics, advocating for low-flow period interventions. Jiang [63] introduced the AHMS-SED model in the Yellow River Basin to couple hydrology with sediment transport, successfully reproducing gully erosion trends under climatic and human-induced changes. These efforts underscore the growing sophistication of modeling frameworks in supporting sediment management, infrastructure design, and adaptive river basin planning.

This study aims to employ the MIKE 21C modeling framework to simulate and morphological forecast and bank erosion in a selected reach of the Brahmaputra River. The specific objectives include: (i) development and calibration of a 2D morphological model for the target reach; (ii) analysis of hydraulic behavior and morphological dynamics at the south bank hill bend; (iii) simulation of sediment transport and channel evolution under varying hydrological conditions; (iv) projection of future morphological changes, including general and bend scour development; and (v) identification of erosion-prone zones to inform riverbank protection and management strategies.

2. About the study area

Figure 1 depicts the location of the study reach and highlights the key surrounding locations within the study area.

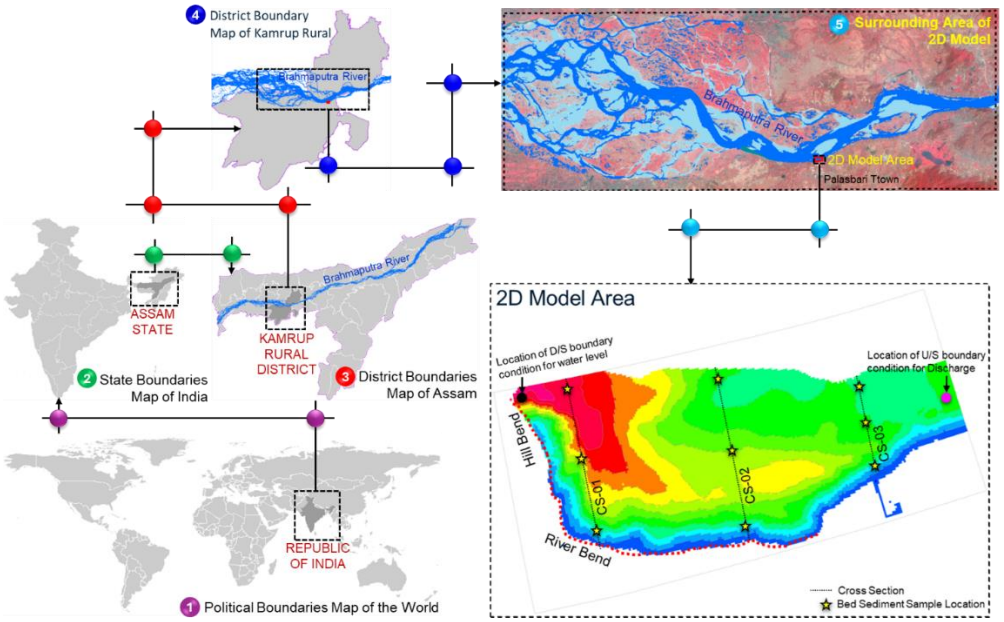
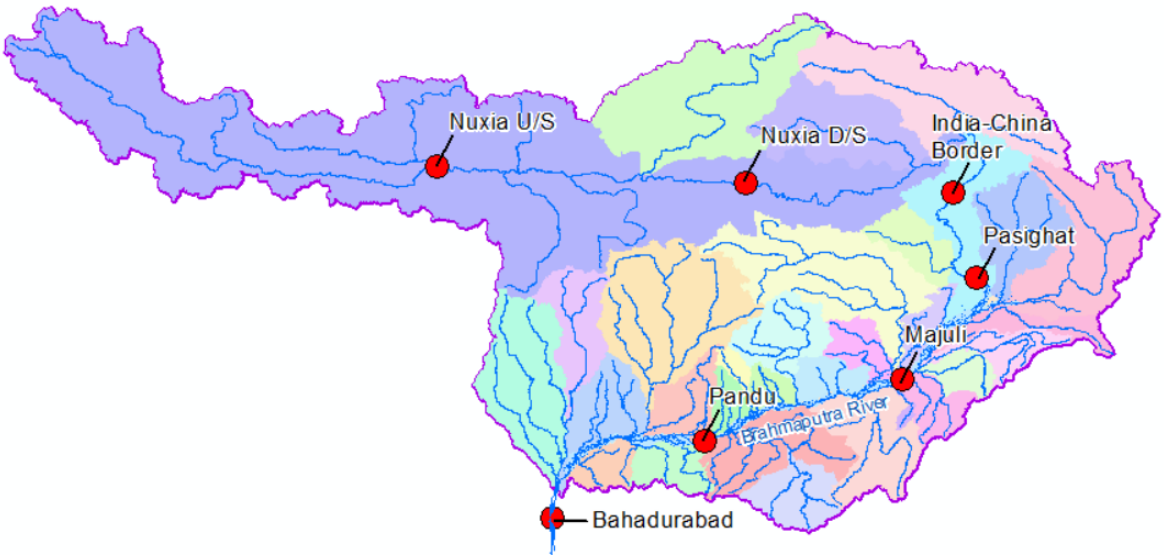


Figure 1. Location map of study area showing hill bend near Palasbari town of Assam state, India

The Brahmaputra River, one of the largest and most sediment-laden rivers in the world, presents a quintessential example of the complexities associated with morphodynamic processes in braided river systems [23, 64, 65]. Originating from the Manasarovar Lake region, near Mount Kailash in the Tibetan Himalayas, the river traverses a highly varied topography and climatic regime as it flows through China (as Yarlung Tsangpo), enters India through Arunachal Pradesh, and meanders through the alluvial plains of Assam before entering Bangladesh [66, 67]. Throughout its course, particularly in the middle reaches across northeastern India, the river is subject to extreme seasonal hydrological variability [68, 69, 70]. This is largely driven by the South Asian monsoon, during which the Brahmaputra experiences substantial increases in discharge, often exceeding 22,000 m^3/s, accompanied by an enormous sediment influx derived from steep, erosion-prone Himalayan catchments [71, 72, 73]. The mean annual flow of the Brahmaputra River system exhibits significant spatial variability across different gauging stations, ranging from approximately 31,200 million cubic meters per year (MCM/yr) to 605,490 (MCM/yr) (Table 1). The annual sediment load of Brahmaputra River has been estimated at over 400 million tonnes / year, placing the river among the highest sediment-yielding systems globally [65, 74, 75].

Table 1. Mean annual flows at key locations along the Yarlung Tsangpo–Brahmaputra–Jamuna River System

S. No.	River reach	Observation site	Mean flow (MCM/yr)	References
1	Yarlung Tsangpo	Nuxia U/S	31,200	[76]
2	Yarlung Tsangpo	Nuxia D/S	60,570	[77]
3	Yarlung Tsangpo	India-China Border	135,900	[77]
4	Siang	Pasighat	185,100	[78]
5	Brahmaputra	Majuli	278,447	[79]
6	Brahmaputra	Pandu	526,100	[80]
7	Jamuna	Bahadurabad	605,490	[76]



Mean annual flow observation sites along the Yarlung Tsangpo–Brahmaputra–Jamuna River System

The hill bend at the study reach is a prominent geomorphological feature along the southern bank of the Brahmaputra River, located in the Kamrup Rural district of Assam, India, near the town of Palasbari. Geographically, the reach spans between 26°07'02.302"N to 26°07'13.661"N latitude and 91°31'06.476"E to 91°31'39.092"E longitude (Figure 1), approximately 20 km southwest of Guwahati. This bend is distinguished by a pronounced curvature adjacent to a stable hill slope, which exerts a substantial influence on the river's hydrodynamic and morphodynamic behavior. The proximity of elevated terrain along the concave (outer) bank confines the channel laterally, enhancing flow acceleration and concentrating shear stress during high discharge events. Consequently, the bend experiences intensified bank erosion and scour development along its outer margin. The restricted lateral mobility due to the hill's presence makes this reach especially vulnerable to hydraulic forces, thereby classifying it as a high-priority zone for riverbank protection and river training interventions. The strategic significance of this bend is further amplified by its proximity to densely populated areas and critical infrastructure, necessitating informed and sustainable morphological management.

The study reach is characterized by a humid subtropical climate, with an average annual rainfall of approximately 2,300 mm (Shing et al., 2004). The mean annual temperature is around 24°C, with minimum temperatures reaching 17°C during the winter months (December to February) and maximum temperatures rising to 39°C in the summer (June to August).

3. Data used

3.1. Digital elevation model and bathymetric data

Copernicus digital elevation model (DEM) a 30 m resolution Digital Surface Model derived from the WorldDEM dataset via the TanDEM-X mission (DLR and Airbus), represents surface features including vegetation, infrastructure, and built-up areas. In this study, Copernicus DEM (2015), sourced from the Copernicus Data Space, was utilized to validate cross-sectional elevation profiles and support detailed topographic analysis of the study area.

Cross-sectional data utilized in this study were obtained from the Water Resources Department, Assam. These datasets were further refined and enhanced through the integration of available bathymetric

measurements to improve the representation of channel geometry and subaqueous features.

Gridded bathymetric data employed in this study were sourced from the General Bathymetric Chart of the Oceans (GEBCO), specifically the GEBCO_2024 Grid-a global terrain model that provides elevation information for both terrestrial and oceanic surfaces. This dataset, available at 15 arc-second (~400 m) spatial resolution, is accompanied by a Type Identifier (TID) Grid, which classifies the underlying sources used in the generation of elevation values. Bathymetric data spanning the period from 2019 to 2024 were downloaded from the GEBCO repositoryto support topographic and morphological analyses within the study area.

3.2. Hydrological and meteorological data

Gridded river discharge data utilized in this study were sourced from the Copernicus Emergency Management Service (CEMS) Early Warning Data Store, specifically from the Global Flood Awareness System (GloFAS). These data are generated using the LISFLOOD hydrological model, which is forced with ERA5 meteorological reanalysis inputs interpolated to a spatial resolution of 0.05° (approximately 5 km) and produced at a 24-hour temporal resolution. GloFAS provides two types of hydrological outputs: intermediate data, derived from the near real-time ERA5T inputs and updated daily, and consolidated data, based on the finalized ERA5 reanalysis and updated monthly. For the present study, daily river discharge data spanning the period 2015 to 2024 were acquired and used to analyze hydrological dynamics within the study reach. The dataset was used for both simulations. The 2-year and 100-year return period floods were computed using statistical frequency analysis of the observed flow data, applying the standard hydrological methods (e.g., Gumbel's extreme value distribution).

Water level observations for the period 2015-2024 were obtained from the Central Water Commission (CWC). These data provide critical insights into the temporal fluctuations of water levels in the study area and were utilized to support hydrodynamic modeling and river behavior analysis.

3.3. Bed sediment sample

In December 2024, a total of nine bed sediment samples were collected using a Van Veen Grab sampler from three cross-sections within the 2D model domain to analyze grain size distribution, gradation, and sorting (Figure 1). The samples were specifically collected to assess hydraulic roughness and sediment transport characteristics. At each cross-section, one sample was taken from the mid-channel, and two samples were collected from the bank-adjacent areas. These data are essential for understanding the sediment dynamics and refining the model's sediment transport predictions.

3.4. Satellite and ancillary data

Satellite imagery from Landsat-5 TM, Landsat-7 ETM+, Landsat-8 OLI, and Landsat-9 OLI-2, each with a spatial resolution of 30 meters, covering the period from 2013 to 2024, were obtained from Earth Explorer. These images were employed for the analysis of river planform, riverbank erosion, and delineation of banklines, providing critical data for understanding morphological changes in the study area.

3.5. Data limitations

Despite the use of reliable and widely accepted datasets, certain limitations were inherent in the input data utilized for this study. The Copernicus DEM, with a spatial resolution of 30 m, may include surface features such as vegetation and built-up infrastructure, potentially leading to overestimated elevations in densely vegetated or urbanized areas. To mitigate this, cross-sectional elevation data from the Water Resources Department, Assam, were

used to validate and refine terrain representation. Similarly, GEBCO bathymetric data, available at ~400 m resolution, lack the spatial detail necessary for fine-scale channel morphology representation and were therefore enhanced using in-situ bathymetric and cross-sectional measurements where available. The GloFAS discharge dataset, while offering consistent and long-term gridded hydrological data, represents modelled outputs and may not fully capture localized flow variability, particularly in complex alluvial systems like the Brahmaputra. To address this, observed water level data from the Central Water Commission (CWC) were used for calibration and validation of hydrodynamic simulations. Furthermore, satellite imagery analysis using multi-temporal Landsat data (2013-2024), with a spatial resolution of 30 m, is affected by seasonal cloud cover and varying river stages, which may obscure banklines and charland features. These limitations were addressed through careful image selection and cross-verification using ancillary datasets. While these measures enhance data reliability, the inherent limitations may still introduce uncertainties in model outputs, particularly in regions with sparse observations or highly dynamic morphological features.

4. Methodology

4.1. Overview of numerical modelling tools

Two-dimensional numerical models are effective tools for simulating long-term river morphology and assessing the influence of river engineering structures. A benchmarking study conducted by the National Sedimentation Laboratory (ARS-USDA) for the U.S. Army Corps of Engineers [81] evaluated the capabilities of such models. Among several candidates, only five met the established criteria: MIKE 21C (DHI, Denmark), Delft2D-Rivers (Deltares, Netherlands), CCHE2D (NCCHE, University of Mississippi, USA), TABS-MD (US Army Corps of Engineers, USA), and TELEMAC (EDF, France). Of these, MIKE 21C and Delft2D demonstrated the most comprehensive theoretical frameworks for modeling sediment transport, bank erosion, and morphological evolution in curved river channels. A comparison of their key features is summarized in Table 2.

Table 2. Salient features of MIKE 21C and Delft2D for two-dimensional hydrodynamic and sediment transport simulations

S. No.	Key features	MIKE 21C	Delft2D
1	Governing equations solved in curvilinear finite difference gird	✓	✓
2	Time integration method is second order, thus accurate and allows larger time step, computation is efficient	✓	✓
3	Capable of wetting and drying, very important in braided rivers	✓	✓
4	Temporal and spatial variation in use of flow roughness, very important in braided rivers	✓	x
5	Simulate non-cohesive bed material separately for bed and suspended load by different size class, and erosion/deposition of riverbed	✓	✓
6	Simulating transport, erosion, deposition and consolidation of cohesive materials	✓	✓
7	Simulate transport of sand and mud mixtures	✓	x
8	Include effects of helical flow in river bends on momentum and sediment load	✓	✓
9	Bank erosion in fixed and in moveable grid	✓	x

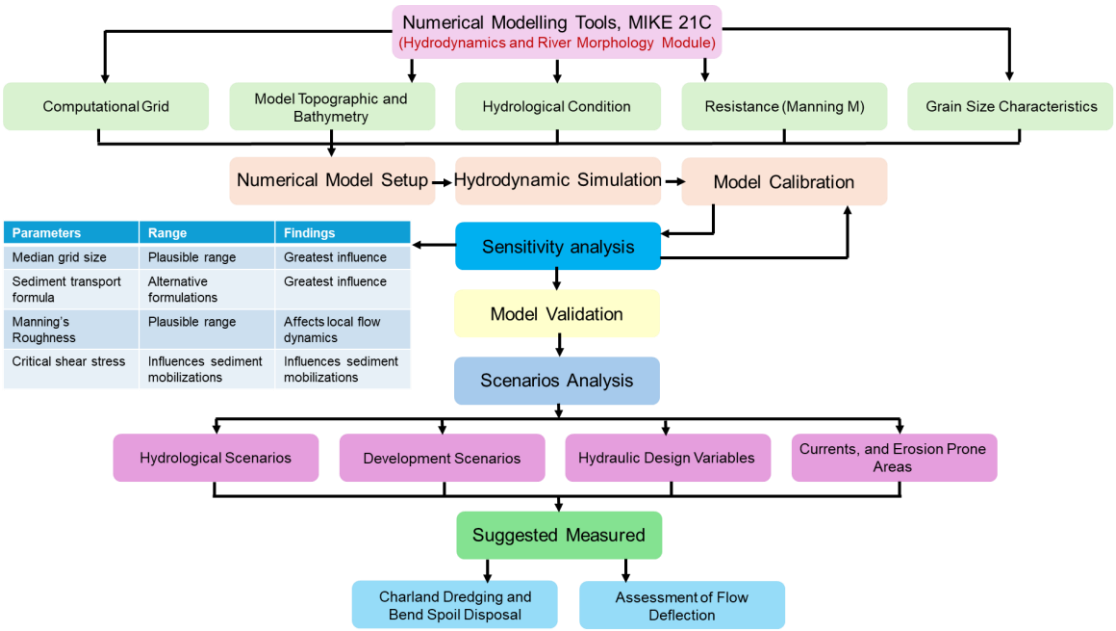


Figure 2. Schematic workflow of the methodology for 2D hydrodynamic and morphodynamic modeling.

MIKE 21C was selected for its advanced capabilities in simulating complex fluvial systems, particularly braided river reaches. Its use of a flexible curvilinear grid allows for precise representation of natural channel geometry with minimal grid distortion. In contrast to Delft2D, which employs structured or unstructured grids, MIKE 21C offers enhanced efficiency in modeling sediment transport dynamics, bank erosion processes, and long-term morphological evolution. This makes it particularly suitable for detailed, process-based analyses required in river engineering and sediment management applications. A schematic workflow of the methodology and modeling framework is shown in **Error! Reference s ource not found.**.

4.2. Model setup and input data

4.2.1. Computational grid

A two-dimensional hydrodynamic model of the study reach near the hill bend was developed using 7,860 computational cells within a curvilinear orthogonal grid framework in the MIKE 21C modeling system. The domain spans approximately 1 km in length and 0.5 km in width, comprising 120 cells along the flow direction and 65.5 cells across the channel. The curvilinear grid enables variable cell dimensions, with an average longitudinal cell size of about 7.5 meters, allowing efficient representation of complex channel geometry (Figure 3). A detailed mesh convergence test was conducted to ensure numerical accuracy and solution stability. Multiple grid resolutions were evaluated, and key hydraulic and morphological outputs-such as velocity distributions, bed level changes, and water surface profiles-were compared. Convergence was confirmed when changes in results between successive mesh refinements became negligible (within 5%). This high-resolution configuration was found to be optimal capturing localized morphological dynamics such as bend scour, obstruction-induced scour, and bank erosion with sufficient precisions. The model's capability was validated through bathymetric outputs, which successfully depict the observed scour zones near the hill toe with well-defined depth contours.

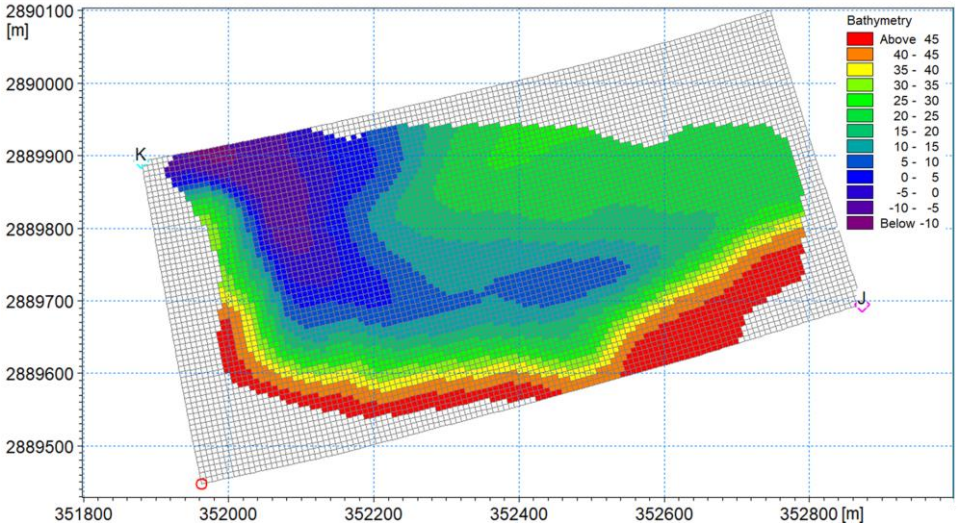


Figure 3. Curvilinear grid configuration and bathymetric profile of the hill bend study reach near Palasbari town.

4.2.2. Model topography and bathymetry

The bathymetry for the two-dimensional model was developed using a combination of gridded bathymetric datasets (2019-2024) and high-resolution cross-sectional data. Approximately 40 cross-sections were collected over a 1 km stretch along the thalweg, capturing the channel's deepest zones. The integrated dataset enabled the construction of a detailed bathymetric surface within the model domain, as illustrated in Figure 3. The resulting bathymetry effectively resolves morphological features such as scour zones, particularly in the vicinity of the hill bend, owing to the fine spatial resolution of the computational grid and the high accuracy of the survey inputs.

4.2.2. Hydrological condition

The boundary conditions for the present localized hydrodynamic model were derived from a large-scale model framework [82]. The upstream inflow boundary was specified using discharge data from the Pandu gauging station, while the downstream boundary was defined by applying observed water level data. Model calibration was performed using data from the 2023 hydrological year (Figure 4), and subsequent validation was carried out in June 2024. Discharge at the Pandu station for the calibration period was estimated through a stage–discharge relationship established via a rating curve based on observed water level measurements.

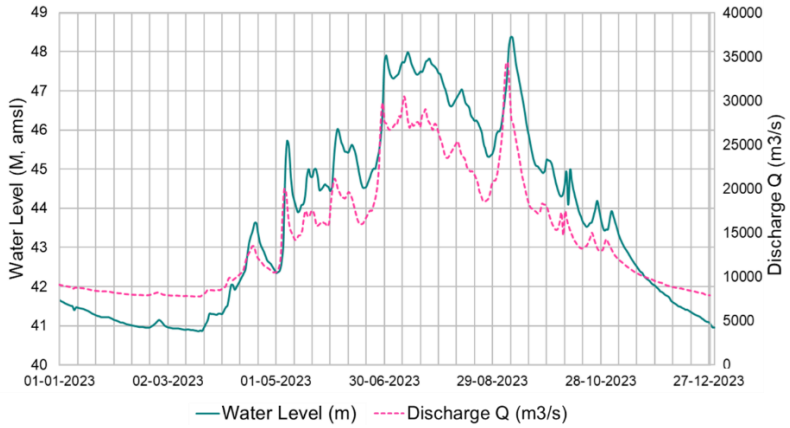


Figure 4. Two-dimensional model boundary conditions, inflow discharge and downstream water

level at Pandu gauging station.

At the Pandu gauging station, the bankfull discharge is approximately 42,500 m³/s, while the corresponding bankfull discharge incorporated from the large-scale model into the local model domain is about 10,073 m³/s. The 100-year flood discharge at Pandu is estimated at 66,000 m³/s, whereas the large-scale model provides a value of approximately 16,943 m³/s for the local reach. A continuous time series of discharge at Pandu was reconstructed from daily water level records using empirically derived stage–discharge rating relationships (Eq.1 and Eq.2). These relationships were developed based on observed water levels and corresponding discharge measurements from the 2014 hydrological year, which captured a comprehensive range of flow conditions, including near-bankfull stages. The Pandu gauging site is located within a geomorphologically stable reach of the Brahmaputra River, rendering the rating curves robust and valid across the recent decade (2015-2024). The established rating curves have also demonstrated reliable predictive capability for extreme hydrological events, including the 2-year (bankfull), 50-year, and 100-year return period discharges [53, 83, 84]. The 2-year (bankfull), 50-year, and 100-year return period discharges were estimated using established rating curves, developed from observed stage-discharge data at the Pandu gauging station for the period 2000-2023. Frequency analysis using the Gumbel distribution was then applied to the rating curve-derived discharge values to estimate the return period floods. These rating curves have demonstrated reliable extrapolation capability for extreme events.

Two rating curve equations were employed to estimate discharge at the Pandu gauging station, segmented by stage height.

Stage-I rating curve, valid for water levels up to 47.13 m amsl, is expressed as:

$$h = 14.163 \times Q^{0.1182} \quad (1)$$

Stage-II, applicable for water levels exceeding 47.13 m amsl, is defined as:

$$h = 23.923 \times Q^{0.0673} \quad (2)$$

Where h is the water level (m amsl) and Q is the discharge (m³/s).

Although refinement of the rating relationship for low-flow conditions (Q < 10,000 m³/s) during the dry season was feasible, such enhancements were deemed less critical given the focus on simulating flood-induced morphological changes. Nevertheless, the rating curve was optimized as part of the model calibration process. Ideally, the downstream boundary conditions of the 2D model would rely on observed stage data. However, in the absence of a gauging station in proximity to the downstream boundary-aside from the Pandu station-water level inputs were extrapolated to this location. This introduces a degree of uncertainty in the model outputs. To address this, a boundary sensitivity analysis was performed to evaluate the influence of downstream conditions on model performance and improve reliability.

4.2.4. Grain size characteristics

The collected samples were conducted using a Van Veen grab sampler, adhering to established procedures [85, 86]. Sieve analysis [87] was employed to quantify the sediment size classes, including the median grain diameter (D_{50}), which are presented in Table 3. The observed grain size data align well with published values for the Brahmaputra River, further validating the field measurements.

Grain sorting, evaluated through the sorting coefficient (σ), revealed well-sorted sediment across the sampled reach. Values of σ were consistently below 1.6, indicating a uniform sediment distribution as defined by established thresholds [46, 88]. Such uniformity justifies the use of sediment transport equations that assume a single representative grain size (D_{50}), thus improving the reliability of sediment transport and morphological modeling in the 2D simulation framework (Table 3).

Table 3. Grain size characteristics of bed material in the study reach (field data) and the Brahmaputra River (from literature).

S. No.	Grain class	Study reach*	Brahmaputra in Assam**	Brahmaputra in Jamuguri***
1	D_{16} (mm)	0.15		
2	D_{50} (mm) #	0.24	0.25 to 0.16	0.16
3	D_{65} (mm)	0.29		
4	D_{84} (mm)	0.44		
5	σ (grain sorting parameter, $(D_{84}/D_{50})^{0.5}$	1.65		

* Grain size distribution (median size class, see note below) of the sediment samples collected by Author.
* All the grain size distribution (GSD) values are averaged across the three cross-sections.
** Grain size range [89].
*** Grain size at Jamuguri [90].
# The D_{50} values in the table are arithmetic means of D_{50} values of all samples from respective river reach.

4.3. Sensitivity analysis

A sensitivity analysis was performed to assess the impact of key input parameters on sediment transport and morphological evolution in the MIKE 21C model. Parameters tested included median grain size (D_{50}), sediment transport formula, Manning's roughness coefficient, and critical shear stress for erosion and deposition. Each was varied within plausible limits derived from field data and literature, while keeping others constant [91, 92]. Model responses were evaluated in terms of changes in bed elevation, sediment flux, and scour depth.

The analysis revealed that sediment transport formula selection and D_{50} exert the greatest influence on predicted erosion and deposition patterns [30]. Manning's roughness primarily affected local flow dynamics, while critical shear stress influenced sediment mobilization thresholds under moderate flows [93]. These findings highlight the necessity of accurate field calibration to ensure reliable morphological forecasting in braided and dynamic riverine systems.

4.4. Scenarios and calibration

4.4.1. Hydrodynamic and erosion prediction

Hydrodynamic and erosion prediction involves simulating flow dynamics and sediment transport to identify erosion-prone zones and assess morphological changes. This helps evaluate the impact of hydraulic structures and flow variations on channel stability.

Hydrological scenarios: Hydrodynamic simulations were conducted under varying hydrological conditions to predict key design parameters along the study reach. The modeling focused on the monsoon season, characterized by heightened morphological activity. Two primary flood scenarios were evaluated: (i) the bankfull discharge condition, representing an event with an approximate 2-year return period, and (ii) the extreme 1 in 100-year flood condition. Discharge and water level hydrographs from the 2023 monsoon season (Figure 4) were used as a baseline and subsequently scaled to reflect the peak magnitudes associated with these design flood scenarios.

Development scenarios: For morphological forecasting, the above hydrological condition has been used, the condition / scenario for morphological prediction was as follows: (i) full length of the south bank of study reach was considered non-erodible, similar to assumption the banks are trained/fixed; aim is to assess scour development in the river, and will allow to

see extreme development useful for assessing dimension of protection work into the river, and volume of protection material; model will assess the magnitude of scour. However, the calculation of the volume of protection material or size of material / rock / boulder is intended to be calculated after adding local scour depth to the scour predicted by the 2D model; (ii) the river training work at upstream of study reach was set-up in the model, i.e., existing protection work immediate upstream of damaged study reach is considered as fixed, i.e., non-erodible bank, and thus, impact on bank erosion of the damaged bend reach on south bank has been assessed.

Hydraulic design variables: The hydraulic simulations for design variable estimation were conducted under fixed-bed conditions, based on the most recent riverbed topography of 2024. Two hydrological scenarios were considered: (i) bankfull discharge corresponding to a 1-in-2-year return period, and (ii) an extreme flood event with a 1-in-100-year return period. Depth, velocity, and water level distributions around the damaged study reach were computed relative to the 2024 bathymetry. While flow depth is sensitive to temporal variations in riverbed morphology, water levels remain relatively stable under consistent hydrologic inputs. Therefore, the water levels reported in Table 4 can be applied to estimate depth for other recent topographic conditions. The depth-averaged velocities values, as presented, exhibit minimal sensitivity to minor bed level changes. A comprehensive summary of the computed hydraulic variables is provided in Table 4. It is important to emphasize that the total design scour depth must include both general and local scour components. The current 2D MIKE 21C model framework is also recommended for evaluating the hydraulic performance of proposed riverbank protection measures such as revetments, geo-bags, or spurs.

Currents, and erosion prone areas: The study reach, characterized by an active meander bend, exhibits significant morphological dynamics, with both primary and secondary flow components playing critical roles in driving erosion processes. Under bankfull discharge conditions - which occur with relatively high frequency - the model predicts primary flow velocities exceeding 2 m/s, with peak velocities reaching approximately 3 m/s. This generates strong flow circulation and reverse flows in the downstream portion of the bend, with reverse velocities also exceeding 2 m/s (Figure 5 A). Given that the critical threshold for initiating sediment motion for 0.24 mm sand is approximately 0.1 m/s, such frequent high-flow conditions are sufficient to induce substantial bed scour and bank erosion. The presence of strong secondary currents further exacerbates these processes; the prevailing secondary flows are directed away from the bank (i.e., in the positive direction), which intensifies lateral sediment transport and enhances scouring along the outer bank (Figure 5 B). The current speed (Figure 5 C), and bed level map (Figure 5 D) confirms the persistence of a pronounced scour hole (bed elevation below -5 m) near the toe and head of the hill at the study reach. There is no indication of sediment deposition or natural infilling in this zone, suggesting that erosional processes will continue to dominate the morphological evolution of this bend.

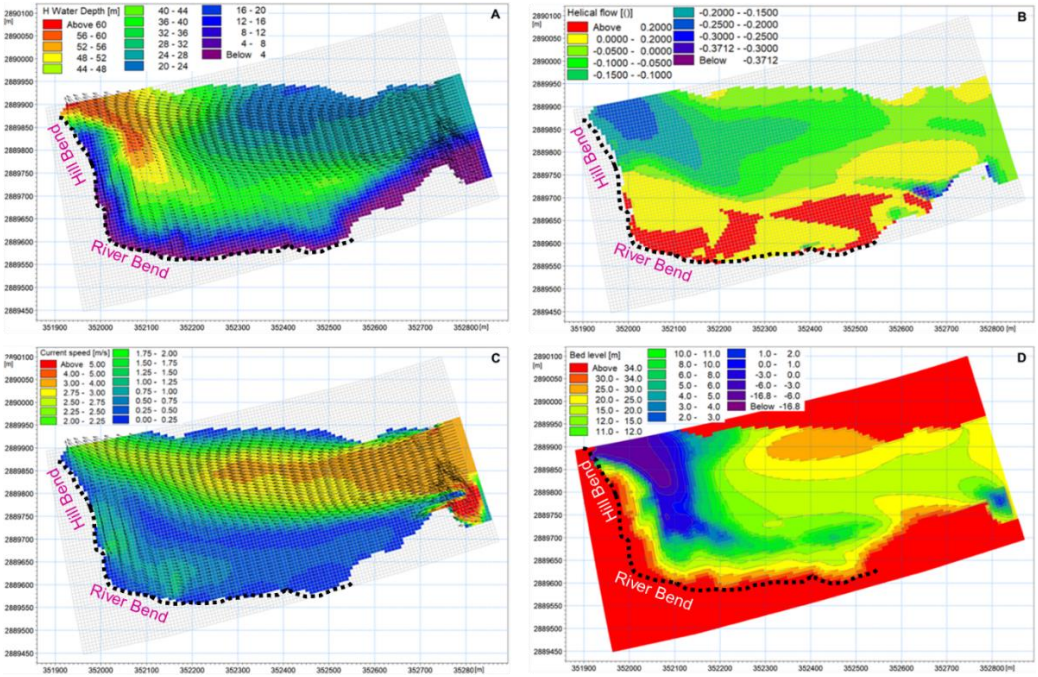


Figure 5. (A) spatial distribution of depth-averaged primary flow, (B) patterns of dimensionless helical flow intensity (secondary flow structure), (C) velocity magnitude (current speed), and (D) longitudinal variation in bed elevation along the hill-bend study reach near Palasbari town.

Table 4. Summary of measured data and simulated hydraulic parameters along the south bank of the study reach, and Pandu gauging station.

Hydraulic variables		Measured data	Simulated	
			1 in 2-year flood (bankfull discharge)	1 in 100-year flood
Pandu gauging station				
Depth (m)	Maximum		63.23	65.24
	Average		28.64	29.32
Water level (m, amsl)	Maximum		47.35	49.52
	Average	47.23	47.25	49.27
	Minimum		47.06	48.67
Speed (m/s)	Maximum		02.97	04.83
	Average		01.24	02.05
Study reach		Yr-2024		
Discharge (m^3/s)	Average		10,073	16,943
Depth (m)	Maximum	33.03	33.83	35.49
	Average	09.05	09.84	11.48
Water level (m, amsl)	Maximum	46.88	47.72	49.59
	Average	46.42	47.13	48.85
	Minimum	46.04	46.73	48.23
Speed (m/s)	Maximum	02.51	02.81	03.31
	Average	01.23	01.43	01.83

4.4.2. Model calibration

Hydraulic calibration: Hydraulic calibration involves adjusting flow resistance parameters to ensure the modelled water levels align with observed data. In this study, Manning's resistance formulation was adopted, with the calibration performed iteratively using the model in hydrodynamic-only mode (i.e., excluding river morphological processes). The Manning's roughness coefficient (expressed as Manning's M) was systematically varied to optimize the agreement with observed upstream water levels (Figure 6).

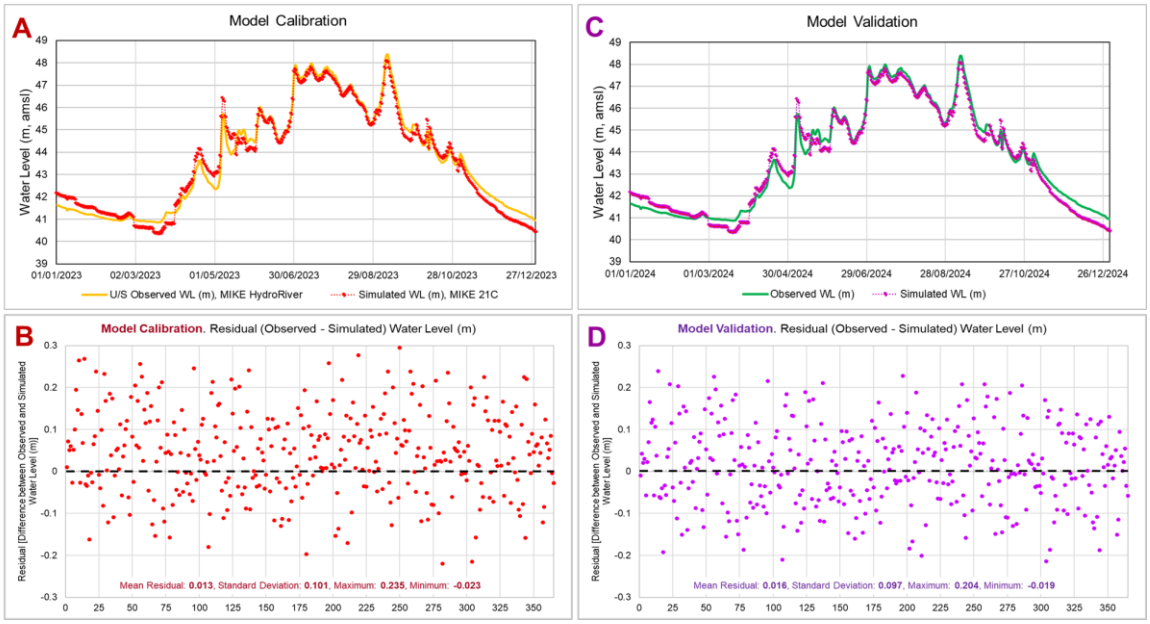


Figure 6. (A) Calibration of water levels for hydraulic resistance estimation; (B) residual analysis of the calibrated model; (C) validation of simulated water levels; (D) residual analysis of the validated model.

The calibration yielded Manning's M values ranging from 22 to 35, while calibration yielded a Manning's M value of 23 $m^{1/3}/s$, indicative of relatively high flow resistance-consistent with conditions typical of large, vegetated, and weed-infested rivers. Although this value may appear high, further assessment confirmed its plausibility within the context of the site-specific hydraulic characteristics. Water levels were carefully calibrated and subsequently validated, demonstrating excellent agreement with observed data. In addition, residual error analysis was performed for both calibration and validation phases, revealing minimal bias and confirming a strong model fit across the entire simulation period.

Figure 6 provides a comprehensive assessment of the hydrodynamic model's performance through calibration and validation analyses, presented in four panels. The panel (A) depicts the calibration phase for 2023, where observed upstream water levels (U/S observed WL) obtained from MIKE Hydro River are compared against simulated water levels generated by MIKE 21C. This comparison demonstrates the model's ability to reproduce temporal variations in water levels under observed flow conditions. The panel (C) presents the validation phase for 2024, contrasting observed water levels with MIKE 21C simulations to evaluate the model's predictive capability under independent datasets. The panel (B) shows the residuals (observed - simulated) during calibration, providing a quantitative measure of model accuracy. The residual distribution indicates a mean bias of 0.013 m, with variability characterized by a standard deviation of 0.101 m and extremes ranging between -0.023 m and 0.235 m. The panel (D) displays the residuals during validation, with a mean bias of 0.016 m, a standard deviation of 0.097 m, and values spanning -0.019 m to 0.204 m. Collectively, these panels demonstrate that the model achieves close agreement with observed water levels, with residuals remaining within acceptable limits for hydrodynamic simulations. The integrated presentation of calibration and validation results, alongside residual statistics, provides a coherent evaluation of

model robustness, accuracy, and reliability across different temporal datasets.

It is important to note that the model demonstrates superior performance under high discharges conditions, whereas it tends to overestimate water levels during low-flow (dry season) periods relative to MIKE Hydro River outputs. Such deviations between high and low discharge calibrations are frequently observed in hydrodynamic modeling.

In morphodynamic applications, minor discrepancies during low-flow periods are generally considered acceptable due to the nonlinear nature of sediment transport processes, which are predominantly driven by high-flow events.

Sediment transport calibration: Following the calibration of hydraulic resistance, the sediment transport component was subsequently adjusted. This was performed with the sediment transport module activated alongside bathymetric updating, enabling dynamic feedback between sediment movement and bed level changes.

The Engelund-Hansen total load transport formula [94] was adopted for simulating sediment dynamics in the study reach. To align model output with the observed sediment rating curve, a scaling factor of 0.4 was applied to the original formulation. This modification is considered justifiable, as it remains within a reasonable range near unity and ensures that the sediment transport estimates remain physically realistic (Figure 7). In contrast, applying a substantially lower factor, such as 0.01, would undermine the empirical integrity of the model and compromise its realism. The observed sediment rating curve used for calibration was derived from sediment flux data reported at the Pandu gauging station, using both available field measurements and values from established literature.

Since the Engelund-Hansen equation provides an estimate of the total sediment load, a load partitioning scheme was applied in order to distinguish between suspended and bed material transport. In this study, 75% of the total load was assigned to the suspended fraction. This choice is supported by sedimentological investigations of the Brahmaputra River and other large alluvial rivers, which consistently highlight the dominance of suspended material in the transport regime, particularly during monsoonal high flows. Previous field observations and sediment rating analyses (e.g. [23, 89]) indicate that suspended load typically constitutes 70-90% of the total sediment flux, with the remainder comprising bed load. Adopting 75% as the suspended fraction therefore lies well within the empirically observed range and aligns with established morphodynamic modeling practices for large sand-bed rivers. This approach not only reflects the natural transport dynamics of the Brahmaputra but also provides a stable and physically realistic input for the model simulations.

The application of the Engelund-Hansen sediment transport formula, though widely accepted, involves empirical adjustments that introduce uncertainty. The use of a 0.4 scaling factor, while within a reasonable range, reflects model calibration to observe data at the Pandu gauging station and may not fully capture temporal variability or extreme flow conditions. Additionally, the assumed 75% suspended load partitioning, although appropriate for large rivers like Brahmaputra, does not account for spatial heterogeneity in flow and sediment dynamics. Limited grain size and bathymetric data also contribute to uncertainty in hydraulic roughness and sediment flux estimation. These factors underscore the need for continuous field data and probabilistic approaches to improve model robustness and reduce uncertainty.

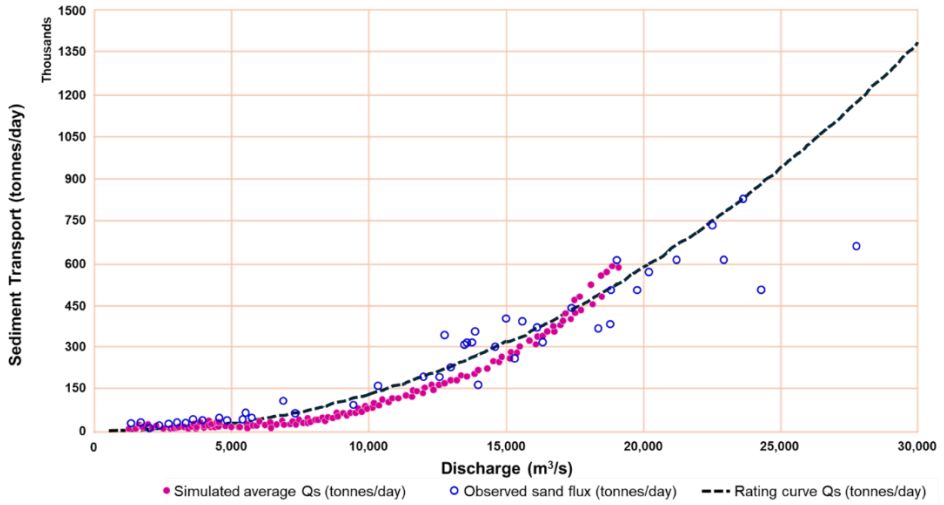


Figure 7. Sediment transport model calibration.

The sediment transport model was rigorously calibrated and validated using observed sediment data expressed in tonnes per day. The calibration process involved adjusting model parameters to match the temporal variations of observed sediment flux, while the validation confirmed the model's ability to reliably reproduce sediment transport dynamics within the study reach. This approach ensures that the simulated sediment flux captures both the magnitude and temporal patterns of sediment transport under varying flow conditions. Figure 8 subsequently illustrates the comparison between observed and simulated sediment flux values, demonstrating the model's performance.

The sediment transport model was successfully calibrated and validated using observed data expressed in tonnes per day (Figure 8). The simulated results closely matched the observed sediment transport values in both phases, demonstrating the robustness of the model. Residual analysis was also conducted for calibration and validation, which showed minimal errors and no significant bias, indicating a strong agreement between observed and simulated values and confirming the reliability of the model's performance.

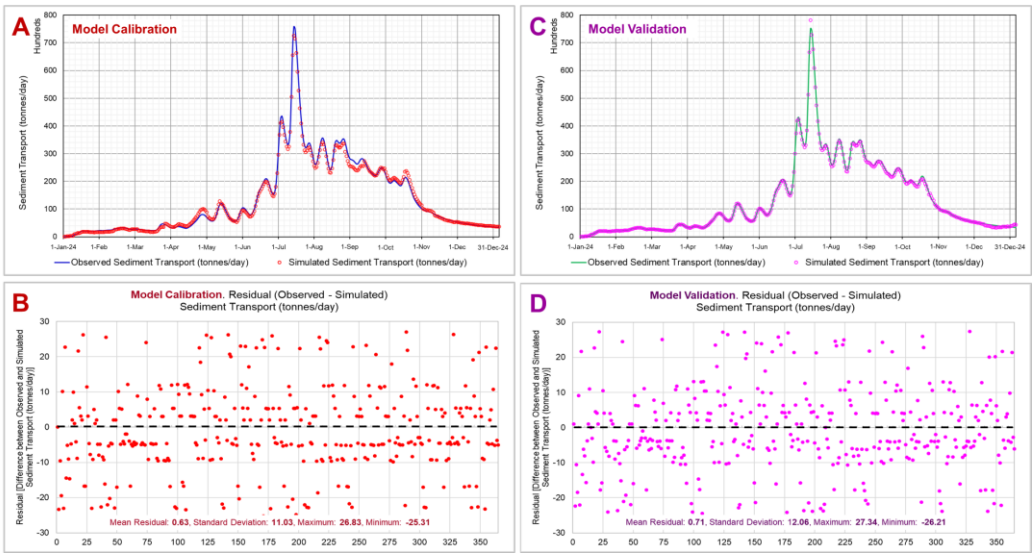


Figure 8. (A) Calibration of sediment transport; (B) residual analysis of the calibrated model; (C) validation of simulated sediment transport; (D) residual analysis of the validated model.

Figure 8 presents a comprehensive evaluation of the sediment transport model performance through calibration and validation analyses, organized into four panels. The top-left panel (A) shows the calibration phase, where observed sediment transport (tones/day) is compared against simulated values from January to December 2023. This time-series comparison highlights the model's ability to reproduce seasonal variability and peak transport events, particularly during the monsoon period. The bottom-left panel (B) displays the residuals (observed - simulated) for the calibration dataset, providing a quantitative measure of model accuracy. The residual distribution indicates a mean bias of 0.63 tonnes/day, with variability characterized by a standard deviation of 11.03 tonnes/day and extremes ranging between -25.31 and 26.83 tonnes/day.

The top-right panel (C) represents the validation phase, where observed sediment transport data from an independent dataset (January-December 2024) are compared with simulated values. This panel demonstrates the model's predictive capability under conditions not used for calibration. The bottom-right panel (D) shows the residuals for the validation dataset, with a mean bias of 0.71 tonnes/day, a standard deviation of 12.06 tonnes/day, and values spanning -26.21 to 27.34 tonnes/day. Collectively, these four panels provide an integrated assessment of model performance, demonstrating that the calibration and validation procedures were conducted using distinct temporal datasets, and that the residuals remain within acceptable limits for sediment transport simulations.

5. Results and discussion

5.1. Approaches to mitigate erosion risks

The study reach bend has exhibited significant morphological activity since 2024. Historical bankline analysis from 2013 to 2024 indicates that the reach remained relatively stable until recent years. However, post-2024 observations reveal substantial bank erosion and bend migration, resulting in the formation of deep scours and incised channels, with general scour depths ranging from 20 to 30 meters-local scour depths being considerably greater. This heightened morphological sensitivity, particularly in the context of ongoing and future developmental activities, necessitates a carefully engineered approach to erosion mitigation. Any proposed intervention must account for potential risks such as continued scour progression, compromised structural stability of the hill adjacent to the study reach, accelerated bank retreat, and long-term threats of bend evolution and out-flanking.

To evaluate these concerns, two mitigation scenarios were tested using hydrodynamic modeling under a 1-in-100-year flood condition [95]. The objective was not only to identify favourable effects but also to assess potential negative consequences, thereby informing risk-aware decision-making. It is strongly advised that all proposed mitigation strategies be subjected to rigorous scenario-based modeling and risk assessment prior to implementation. While current simulations were limited to hydrodynamic analyses, a more robust evaluation would require morphological modeling over extended temporal scales. This necessitates high-resolution bathymetric data and model domain expansion to reduce uncertainty associated with boundary condition influences. The constrained spatial extent of the current model introduces limitations for long-term morphological predictions, underscoring the need for more comprehensive data and modeling frameworks in future assessments.

5.2. Charland dredging and bend spoil disposal

Dredging is planned in the shallow charland located on the opposite side of the eroding

bank. In the model, approximately 8 meters of material is removed through dredging, and the excavated sediment is subsequently deposited along the eroded bank, forming a raised feature approximately 10 meters high (Figure 9). The primary objective of this intervention is to redirect the primary flow into the newly dredged channel, thereby reducing flow impingement on the outer bank. Concurrently, the strategic placement of dredged material at the eroded bend is intended to diminish local flow circulation and suppress the formation of secondary currents-mechanisms that are often responsible for enhancing bend scour and accelerating bank erosion. This approach, simulated under conditions equivalent to a 2-year return period flood, aims to stabilize the bend and mitigate further morphological degradation.

5.3. Assessment of flow deflection

The proposed flow deflection structures upstream are intended to achieve objectives similar to those of dredging the shallow charland located opposite the bank. These structures are designed to redirect the main flow toward the opposite side, thereby enhancing scouring and improving channel conveyance (Figure 10). The simulations for these structures were performed under conditions equivalent to a 2-year return period flood. However, their implementation is also being assessed for potential adverse impacts. Given that the study reach is a short and dynamically evolving meander bend, it is critical to evaluate whether the introduction of such deflection structures induces increased eddy formation or intensified secondary currents immediately downstream conditions that may be more detrimental than the existing hydraulic and morphological state.

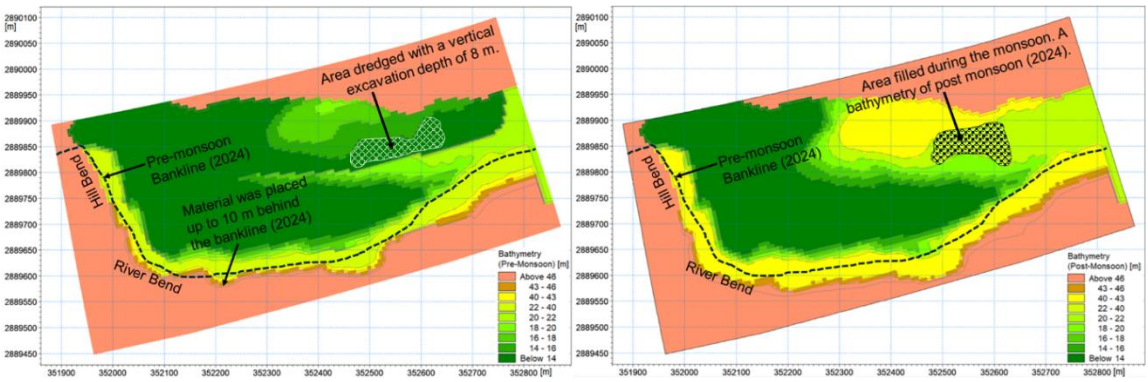


Figure 9. Dredging and material disposal scenarios are illustrated for the pre-monsoon (left) and post-monsoon (right) periods of 2024.

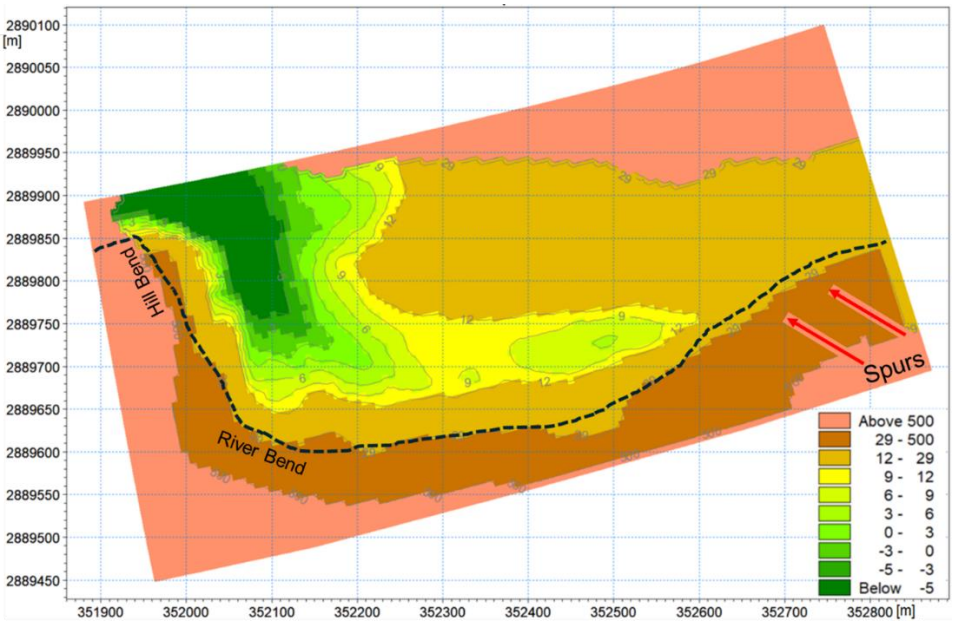


Figure 10. Spur structures designed to alter flow direction are situated roughly 1 km upstream from the hill segment of the study reach near Palasbari town.

5.4. Evaluation of dredging and sediment disposal scenario

The dredging and disposal scenario appears to be hydraulically favourable, as it reduces the intensity of flow circulation and facilitates increased discharge through the dredged channel section. In contrast, the flow deflection scenario-based solely on hydrodynamic simulations-demonstrates unfavourable outcomes. The deflected flow induces a bend-like circulation pattern toward the opposite charland, as clearly illustrated in Figure 11. This newly formed secondary flow pattern generates a pronounced reverse current along the bank situated behind the hill, thereby intensifying local bank erosion. Consequently, any implementation of flow deflection measures, even if positioned further upstream, must be approached with caution and underpinned by detailed morphological and hydraulic assessments.

It is also important to note that the hill bend within the study reach exhibited relative morphological stability during the period from 2021 to 2024. However, significant morphological activity has been observed post-2024. This raises the need for a thorough investigation into whether any upstream flow interventions may have contributed to this recent instability.

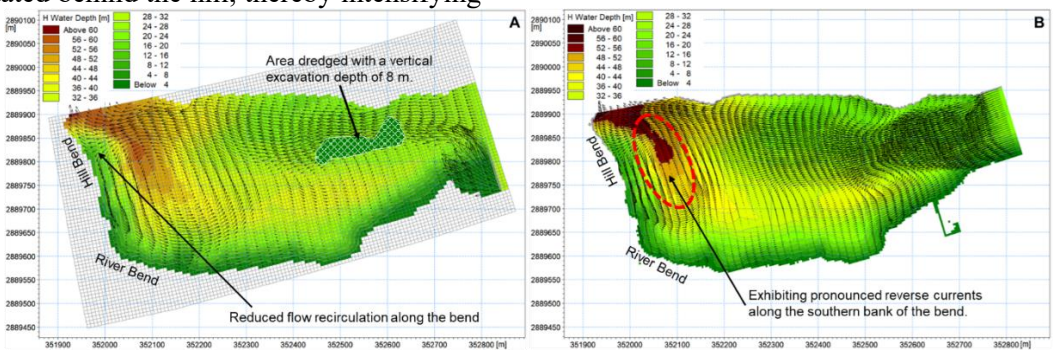


Figure 11. (A) Hydrodynamic simulation of dredging and dumping under a 100-year flood event, showing reduced flow recirculation along the bend; (B) Flow deflection scenario, illustrating increased circulation toward the opposite charland with stronger reverse currents along the southern bank bend.

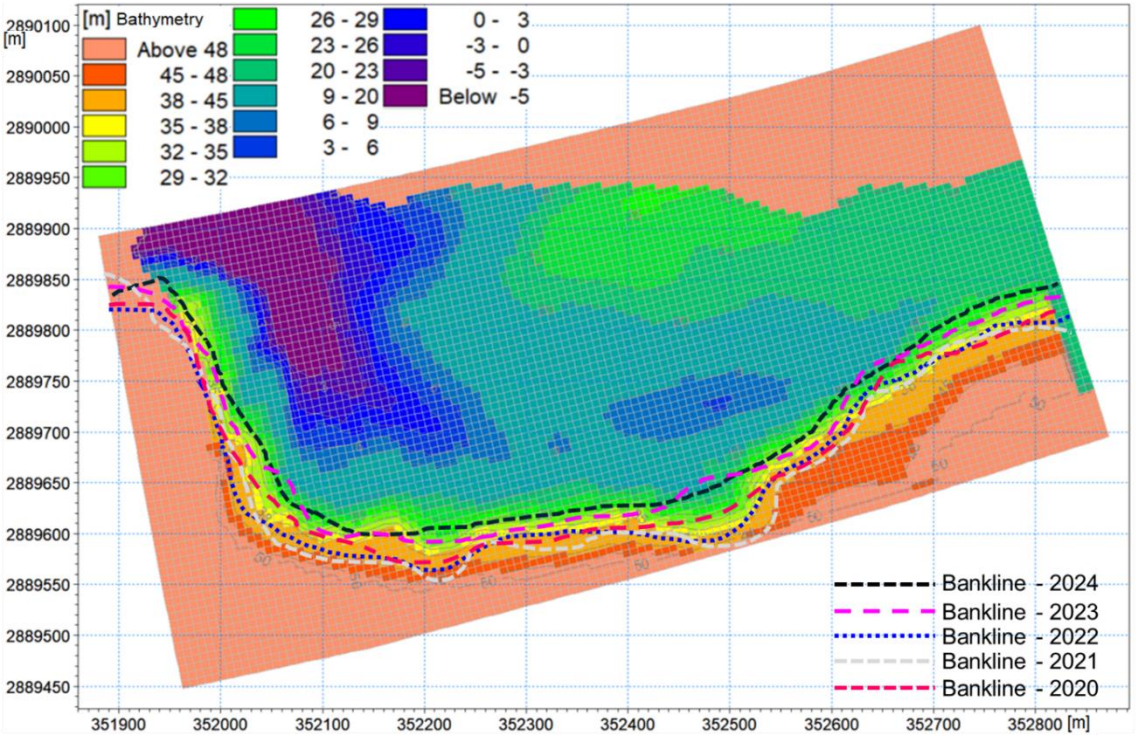


Figure 12. Bathymetric data from the post-monsoon 2024, along with bankline migration observed between 2020 and 2024.

Figure 11 compares two hydrodynamic scenarios under a 100-year flood event. In Panel A, the dredging and dumping scenario reduces flow recirculation along the bend. This outcome is evident from the velocity and depth patterns, which show smoother flow alignment and diminished reverse currents. Such reduction in recirculation can potentially stabilize the bend by lowering localized turbulence and minimizing sediment deposition.

In Panel B, the flow deflection scenario produces the opposite effect. The simulations indicate increased circulation, with the main current curving toward the opposite charland. This deflected flow generates stronger reverse currents along the southern bank bend. The intensified recirculation enhances shear stress on the bank, which may exacerbate erosion processes. The comparison between the two panels highlights how different intervention strategies can either mitigate or amplify bend instability, underscoring the importance of scenario-based hydrodynamic analysis in river management.

Once an erosion protection revetment-such as those constructed using geo-bags or cement concrete blocks installed along an erosion-prone reach of the Brahmaputra River, two outcomes are typically observed: (i) the structure remains functional with the main flow aligned along the protected bank, or (ii) the primary flow path migrates away from the structure, rendering it ineffective or abandoned. Both scenarios have been documented in various reaches of the Brahmaputra. In the first case, where the revetment remains functional and the main flow continues to run adjacent to the protected bank, one consistent hydraulic response is observed: increased bank erosion and bed scour immediately downstream of the revetment. This is attributed to the fact that the protected section resists erosion, thereby causing the flow-now sediment-deprived or 'hungry'-to aggressively erode the downstream unprotected bank and bed. Such a phenomenon has been observed at the hill bend within the current study reach. Satellite-derived bankline analyses (Figure

12) indicate that this bend remained relatively stable from 2020 to 2024. However, under present conditions, the reach is experiencing significant bank erosion and bed degradation. Predictive simulations using the local 2D hydrodynamic model suggest that this erosion trend will persist, with further bed scour anticipated, particularly near the toe of the hill within the study reach. These developments present several potential future risks and management implications that warrant detailed investigation.

5.5. Future morphological risk and flow realignment strategy

In the context of ongoing bank erosion, it is imperative to consider potential future risks-particularly the possibility of the river outflanking the study reach hill and rejoining the main flow channel immediately downstream. This scenario, while extreme, cannot be categorically ruled out. Regardless of whether such a course shift occurs, maintenance interventions are likely to be undertaken to mitigate the current bank erosion. However, once lateral bank migration is arrested through such protective measures, the ongoing bed scour at the toe of the hill has already reached considerable depths expected to intensify. Predictions from the local 2D hydrodynamic model indicate continued deepening of this scour zone. It is important to note that the hill at the study reach is currently functioning in a manner analogous to an engineered spur. Typically, spurs are designed with sloped aprons and the placement of scour-resistant material along the riverbed to counteract localized erosion. In contrast, the study reach hill lacks such protective features, making it particularly vulnerable to undermining by continued scour. This condition poses a significant threat to the structural and geotechnical stability of the hill under the 100-year return period.

As a potential solution to mitigate further scour, it is essential not only to protect the eroding bank but also to divert the main flow away from the bank and the study reach hill. This flow realignment should be initiated upstream of the current model domain, preferably through strategic dredging of a new channel across the opposite charland to guide the discharge away from the vulnerable bankline. While flow deflection using structural measures such as spurs or groynes may also be considered, their placement must be carefully evaluated. Specifically, such structures should not be positioned in the immediate upstream vicinity of the study reach hill. Results from the 2D hydrodynamic model demonstrate that introducing a deflector approximately 1 km upstream of the hill could produce adverse hydraulic effects, including intensified bank erosion. Therefore, the optimal location and design of any deflector must be assessed within an expanded modelling framework that captures a larger spatial domain and integrates both morphological and hydraulic considerations.

6. Conclusions

This study employs a high-resolution 2D hydrodynamic and morphodynamic modeling framework (MIKE 21C) to evaluate erosion risk and inform hydraulic design for a dynamically migrating meander bend along the Brahmaputra River—one of the world's most sediment-laden and hydrologically dynamic alluvial systems. By Simulating two critical hydrological scenarios-the 2-year bankfull discharge and the 1-in-100-year flood—the study provides new insights into extreme morphological responses and sediment dynamics under high-flow conditions. The findings include peak velocities of 4.83 m/s and flow depths exceeding 65 m, and water levels reaching 49.92 m amsl near the Pandu station. The southern bank behind the hill emerged as a persistent high-energy zone, where secondary currents and localized reverse flows (>2 m/s) contributed to progressive bank retreat and deep local scour (>30 m), clearly exceeding sediment motion threshold for 0.24 mm sand, confirming that

the reach is highly susceptible to erosion during frequent flood events.

This work advances current scientific understanding by integrating site-specific sediment calibration (Manning's M of 23 $m^{1/3}/s$; Engelund–Hansen total load formula with 0.4 scaling and 75% suspended load) with scenario-based intervention testing —an approach rarely applied with such spatial and hydraulic detail in the Brahmaputra context. Two mitigation strategies were evaluated under extreme flood conditions: (i) dredging the shallow charland opposite the eroding bank and depositing excavated sediment along the outer bend, and (ii) installing upstream flow deflectors. The dredging-disposal scenario approach reduced erosive flow patterns, while deflectors intensified reverse flow and erosion, underscoring the potential for misinformed structural interventions to exacerbate degradation.

The study also fills a critical research gap by documenting post-2024 bed and bank instability —following a decade of morphological stability—linking it to possible upstream changes and highlighting the urgency for adaptive, system-scale river management. The findings advocate for sediment-guided flow realignment over hard engineering, reinforcing the necessity of domain-wide, process-based morphological modeling to inform sustainable and technically sound riverbank protection in complex alluvial environments.

7. Recommendations

Based on the findings of this study, a set of technical and management-oriented recommendations is proposed to mitigate bank erosion and morphological instability in the dynamic reach of the Brahmaputra River near Palasbari. First, dredging the mid-channel bar (charland) opposite the eroding bank and strategically placing the excavated material along the outer bend proved to be an effective intervention. This approach minimized secondary circulation and high-energy zones along the vulnerable bankline, thereby reducing erosion risk. It is recommended that such sediment-guided realignment strategies be prioritized over hard-engineering structures in similar settings.

Second, structural interventions such as flow deflectors or groynes should not be implemented without extensive hydraulic and morphological simulation. Model results indicate that improper placement—especially near or upstream of the study reach hill—can exacerbate reverse flow and erosion. Any deflector must be positioned with caution and should be evaluated within an extended domain that captures upstream flow conditions, sediment dynamics, and potential feedback mechanisms.

Third, immediate action is needed to stabilize the hill toe, which is currently subject to deepening scour. This may involve the installation of a sloped scour apron using geobags or concrete mattresses to resist undermining forces. Long-term protection measures must integrate both bank stabilization and bed protection strategies.

Fourth, the recent morphological instability observed after 2024 underscores the influence of upstream changes. Therefore, a system-scale monitoring program should be implemented, incorporating satellite-based bankline tracking, bathymetric surveys, and sediment load monitoring to assess cumulative impacts.

Finally, future river training projects should adopt a process-based modeling approach like MIKE 21C to design adaptive and scientifically validated solutions. This ensures that interventions are not only locally effective but also system-compatible, preserving the morphological and hydraulic integrity of one of the world's most complex alluvial rivers. Future studies could also focus on evaluating the optimal frequency of sediment-guided interventions, considering the evolving morphology of the river reach. Moreover, comprehensive assessments of the economic feasibility, technical requirements, and long-term sustainability of such strategies would

provide valuable guidance for practical implementation in similar dynamic riverine environments.

Acknowledgment

Authors are grateful to Managing Director, DHI (India) Water & Environment Pvt Ltd, New Delhi, India for providing the necessary facilities to carry out this work.

Declarations

Ethical Approval: This study did not involve any human participants or animal subjects, and therefore ethical approval was not required.

Consent to Participate: Not applicable. This study did not involve human participants, and therefore no consent to participate was required.

Consent to Publish: Not applicable. This study does not include any individual data or images requiring consent for publication.

Data Availability Statement: The links to publicly available datasets used in this study are provided in the data used section. Other datasets that were collected and analyzed during the study are available from the corresponding author upon reasonable request.

Clinical Trial Number: Not applicable.

Funding Statement: This research was conducted without any external funding.

Conflict of Interest: The authors declare that there are no conflicts of interest regarding the publication of this manuscript.

AI Statement: The authors did not use any artificial intelligence (AI) tools or services in the preparation of this work.

Author Contributions: KP conceptualized and formulated the research study. KP was responsible for the acquisition and analysis of the dataset. UP provided valuable assistance in the hydrological modeling aspects of the study. KP and UP both contributed to the interpretation of the research findings. KP prepared the initial manuscript draft. The final version of the manuscript was critically reviewed, revised, and approved by KP and UP.

References

1. Church M. Channel stability: morphodynamics and the morphology of rivers. In: Rowiński P, Radecki-Pawlik A, editors. *Rivers – physical, fluvial and environmental processes*. GeoPlanet: Earth and Planetary Sciences. Cham: Springer; 2015. https://doi.org/10.1007/978-3-319-17719-9_12
2. Lightbody AF, Kui L, Stella JC, Skorko KW, Bywater-Reyes S, Wilcox AC. Riparian vegetation and sediment supply regulate the morphodynamic response of an experimental stream to floods. Front Environ Sci. 2019;7:40. https://doi.org/10.3389/fenvs.2019.00040
3. Nittrouer JA, Shaw J, Lamb MP, Mohrig D. Spatial and temporal trends for water-flow velocity and bed-material sediment transport in the lower Mississippi River. GSA Bull. 2012;124(3-4):400–414. https://doi.org/10.1130/B30497.1
4. Hooke J. Morphodynamics of active meandering rivers reviewed in a hierarchy of spatial and temporal scales. Geomorphology. 2023;439. https://doi.org/10.1016/j.geomorph.2023.108825
5. Thomas R, Nicholas A. Simulation of braided river flow using a new cellular routing scheme. Geomorphology. 2002;43:179–195. https://doi.org/10.1016/s0169-555x(01)00128-3
6. Kasprak A, Brasington J, Hafen K, Williams RD, Wheaton JM. Modelling braided river morphodynamics using a particle travel length framework. Earth Surf Dyn. 2019;7:247–274. https://doi.org/10.5194/esurf-7-247-2019
7. Kulnu AS, Hazarika N, Bharali P. Evolution and morphodynamics of the large-braided river Brahmaputra during the last four decades of the Quaternary epoch: a spatio-temporal assessment using geoinformatics. Int J River Basin Manag. 2024:1–19. https://doi.org/10.1080/15715124.2024.2421372
8. Church M, Ferguson RI. Morphodynamics: rivers beyond steady state. Water Resour Res. 2015;51(4):1883–1897. https://doi.org/10.1002/2014WR016862
9. Hohensinner S, Hauer C, Muhar S. River morphology, channelization, and habitat restoration. In: Schmutz S, Sendzimir J, editors. *Riverine ecosystem management*. Aquatic Ecology Series. Vol. 8. Cham: Springer; 2018. https://doi.org/10.1007/978-3-319-73250-3_3
10. Schuurman F, Marra WA, Kleinhans MG.

Physics-based modeling of large-braided sand-bed rivers: bar pattern formation, dynamics, and sensitivity. J Geophys Res Earth Surf. 2013;118(4):2509–2527. https://doi.org/10.1002/2013JF002896
11. Williams RD, Brasington J, Hicks DM. Numerical modelling of braided river morphodynamics: review and future challenges. Geogr Compass. 2016;10(3):102–127. https://doi.org/10.1111/gec3.12260
12. Hicks DM, Baynes ERC, Measures R, Stecca G, Tunnicliffe J, Friedrich H. Morphodynamic research challenges for braided river environments: lessons from the iconic case of New Zealand. Earth Surf Process Landf. 2021;46(1):188–204. https://doi.org/10.1002/esp.5014
13. Pareta K. Morphological study of Brahmaputra River in Assam based on historical Landsat satellite imagery from 1996 to 2020. Am J Environ Sustain Dev. 2021;6(2). http://www.aiscience.org/journal/paperInfo/ajesd?paperId=5293
14. Tubaldi E, White CJ, Patelli E, Mitoulis SA, de Almeida G, Brown J, Cranston M, Hardman M, Koursari E, Lamb R, McDonald H, Mathews R, Newell R, Pizarro A, Roca M, Zonta D. Invited perspectives: challenges and future directions in improving bridge flood resilience. Nat Hazards Earth Syst Sci. 2022;22:795–812. https://doi.org/10.5194/nhess-22-795-2022
15. Uddin MJ, Shakik A, Mim FB. Understanding the impact of bridge structure on river morphology through geospatial techniques: case on Teesta River, Bangladesh. Discover Environ. 2024;2:91. https://doi.org/10.1007/s44274-024-00136-z
16. Wright N, Crosato A. The hydrodynamics and morphodynamics of rivers. In: Wilderer P, editor. *Treatise on water science*. Vol. 2. Oxford: Academic Press; 2011. p.135–156. https://www.academia.edu/23806974/The_Hydrodynamics_and_Morphodynamics_of_Rivers
17. Ashmore P. Morphology and dynamics of braided rivers. In: Shroder J, Wohl E, editors. *Treatise on geomorphology*. Vol. 9: fluvial geomorphology. San Diego: Academic Press; 2013. p.289–312. https://doi.org/10.1016/B978-0-12-374739-6.00242-6
18. Eke E, Parker G, Shimizu Y. Numerical modeling of erosional and depositional bank processes in migrating river bends with self-formed width: morphodynamics of bar push and bank pull. J Geophys Res Earth Surf. 2014;119(7):1455–1483. https://doi.org/10.1002/2013JF003020
19. Chadwick AJ, Steel E, Passalacqua P, Paola C. Differential bank migration limits the lifespan and width of braided channel threads. Water Resour Res. 2022;58(8). https://doi.org/10.1029/2021WR031236
20. Wal MVD. Bank protection structures along the Brahmaputra-Jamuna River, a study of flow slides. Water. 2020;12(9). https://doi.org/10.3390/w12092588
21. Pareta K. River morphological modelling of Brahmaputra River, Assam. Int J Hydropower Civ Eng. 2021;2(2):8–17. https://www.civilengineeringjournals.com/ijhce/article/13/3-1-1-892.pdf
22. Debnath J, Sahariah D, Lahon D, Nath N, Chand K, Meraj G, Kumar P, Singh SK, Kanga S, Farooq M. Assessing the impacts of current and future changes of the planforms of river Brahmaputra on its land use-land cover. Geosci Front. 2023;14(4). https://doi.org/10.1016/j.gsf.2023.101557
23. Sarma JN. Fluvial process and morphology of the Brahmaputra River in Assam, India. Geomorphology. 2005;70(3-4):226–256. https://doi.org/10.1016/j.geomorph.2005.02.007
24. Gautam S, Singh A, Dhanya CT, Chandrika. Increased socio-economic vulnerability in the floodplains of Brahmaputra Basin, India. vEGU21, the 23rd EGU General Assembly. 2021. https://meetingorganizer.copernicus.org/EGU21/EGU21-3193.html
25. Pareta K. River morphology of braided Brahmaputra River, Assam, India. Chisinau: LAP Lambert Academic Publishing, Republic of Moldova; 2022. p.1–444. https://www.morebooks.shop/shop-ui/shop/book-launch-offer/1471e9b08e1f2677f4f2c18a12d1dbe6e60d2cdc
26. Sarker S, Sarker T, Leta OT, Raihan SU, Ahmed N. Understanding the planform complexity and morphodynamic properties of Brahmaputra River in Bangladesh: protection and exploitation of riparian areas. Water. 2023;15(7):1384. https://doi.org/10.3390/w15071384
27. Summer S, Walling DE. Modelling erosion, sediment transport and sediment yield. IHP-VI Technical Documents in Hydrology No.

60. Paris: UNESCO; 2002. https://www.hydrology.nl/images/docs/ihp/2002_Modelling_erosion_sediment_127848e.pdf
28. Pareta K, Jakobsen F, Joshi M. Morphological characteristics and vulnerability assessment of Alaknanda, Bhagirathi, Mandakini and Kali rivers, Uttarakhand (India). Am J Geophys Geochem Geosyst. 2019;5(2):49–68. http://www.aiscience.org/journal/paperInfo/aj3g?paperId=4645
29. Mir AA, Patel M. A comprehensive review on sediment transport, flow dynamics, and hazards in steep channels. J Water Manag Model. 2024. https://doi.org/10.14796/JWMM.C517
30. Andualem TG, Hewa GA, Myers BR, Peters S, Boland J. Erosion and sediment transport modeling: a systematic review. Land. 2023;12(7):1396. https://doi.org/10.3390/land12071396
31. Hu Y, Yang H, Zhou H, Lv Q. A review of numerical modelling of morphodynamics in braided rivers: mechanisms, insights and challenges. Water. 2023;15(3):595. https://doi.org/10.3390/w15030595
32. Pareta K. 1D-2D hydrodynamic and sediment transport modelling using MIKE models. Discover Water. 2024;4:94. https://doi.org/10.1007/s43832-024-00130-9
33. Brown RA. Hydrogeomorphic scaling and ecohydraulics for designing rescaled channel and floodplain geometry in regulated gravel–cobble bed rivers for Pacific salmon habitat. Water. 2022;14(4):670. https://doi.org/10.3390/w14040670
34. Odey G, Cho Y. Event-based vs. continuous hydrological modeling with HEC-HMS: a review of use cases, methodologies, and performance metrics. Hydrology. 2025;12(2):39. https://doi.org/10.3390/hydrology12020039
35. Darby S, Sear D. River restoration: managing the uncertainty in restoring physical habitat. Hoboken: John Wiley & Sons Inc.; 2008. https://www.academia.edu/Documents/in/River_Restoration?swp=tc-ri-1156513
36. Javernick L, Hicks DM, Measures R, Caruso B, Brasington J. Numerical modelling of braided rivers with structure-from-motion-derived terrain models. River Res Appl. 2015;32(5):1071–1081. https://doi.org/10.1002/rra.2918
37. Kasvi E, Alho P, Lotsari E, Wang Y, Kukko A, Hyyppä H, Hyyppä J. Two-dimensional and three-dimensional computational models in hydrodynamic and morphodynamic reconstructions of a river bend: sensitivity and functionality. Hydrol Process. 2014;29(6):1604–1629. https://doi.org/10.1002/hyp.10277
38. Horvat Z, Isic M, Spasojevic M. Two-dimensional river flow and sediment transport model. Environ Fluid Mech. 2015;15:595–625. https://doi.org/10.1007/s10652-014-9375-y
39. Zhang Y, Al-Hamdan M, Wren D. Development of a two-dimensional hybrid sediment-transport model. Appl Sci. 2023;13(8):4940. https://doi.org/10.3390/app13084940
40. Lai YG, Thomas RE, Ozeren Y, Simon A, Greimann BP, Wu K. Modeling of multilayer cohesive bank erosion with a coupled bank stability and mobile-bed model. Geomorphology. 2015;243:116–129. https://doi.org/10.1016/j.geomorph.2014.07.017
41. Lai YG. Modeling stream bank erosion: practical stream results and future needs. Water. 2017;9(12):950. https://doi.org/10.3390/w9120950
42. Dubuis R, Cesare GD. The clogging of riverbeds: a review of the physical processes. Earth-Science Reviews. 2023;239. https://doi.org/10.1016/j.earscirev.2023.104374
43. Morianou GG, Kourgialas NN, Karatzas GP, Nikolaidis NP. Hydraulic and sediment transport simulation of Koiliaris River using the MIKE 21C model. Procedia Engineering. 2016;162C:463–470. https://doi.org/10.1016/j.proeng.2016.11.089
44. Vozinaki AEK, Morianou GG, Alexakis DD, Tsanis IK. Comparing 1D and combined 1D/2D hydraulic simulations using high-resolution topographic data: a case study of the Koiliaris basin, Greece. Hydrol Sci J. 2016;62(4):642–656. https://doi.org/10.1080/02626667.2016.1255746
45. DHI. MIKE 21C curvilinear model – scientific documentation. Horsholm: Danish Hydraulic Institute; 2022. https://manuals.mikepoweredbydhi.help/latest/Water_Resources/MIKE21C_Scientific_documentation.pdf
46. Ackers P, White WR. Sediment transport – new approach and analysis. J Hydraul Div. 1973;99(11):2041–2060.

https://ascelibrary.org/doi/10.1061/JYCEAJ.0003791
47. Borden C, Gaur A, Singh CR. Water resource software: application overview and review. Washington (DC): World Bank; 2016. https://documents1.worldbank.org/curated/en/279391467995445292/pdf/106396-WP-PUBLIC-WRS-SAWI-reportjune8.pdf
48. Enggrob HG, Tjerry S. Simulation of morphological characteristics of a braided river. In: River, Coastal and Estuarine Morphodynamics (RCEM) Proceedings; 1998. https://www.dhigroup.com/upload/publications/mike21/Vested_2014.pdf
49. Vested HJ, Tjerry S, Christensen BB, Dubinski IM. Numerical simulation of estuarine and river morphology. In: International Conference on Small Scale Morphological Evolution of Coastal, Estuarine and River Systems; Nantes; 2014.
50. Zongo J, Zabsonre JDD, Roamba B. Formal derivation of a new sediment transport model using a multiscale procedure: numerical validation. Partial Differ Equ Appl Math. 2024;9. https://doi.org/10.1016/j.padiff.2023.100606
51. Aksoy H, Mahe G, Meddi M. Modeling and practice of erosion and sediment transport under change. Water. 2019.
52. Sarker S. Essence of MIKE 21C (FDM numerical scheme): application on the river morphology of Bangladesh. Open J Model Simul. 2022;10:88–117. https://www.scirp.org/journal/paperinformation?paperid=116189
53. Pareta K. Morphological model for erosion prediction of India's largest braided river using MIKE 21C model. Earth Sci Syst Soc. 2024;4. https://doi.org/10.3389/esss.2024.10075
54. Ramakrishnan R, Rajawat AS. Simulation of suspended sediment transport initialized with satellite derived suspended sediment concentrations. J Earth Syst Sci. 2012;121:1201–1213. https://doi.org/10.1007/s12040-012-0222-6
55. Dang TA, Tran TH. Application of the MIKE21C model to simulate flow in the lower Mekong River basin. SpringerPlus. 2016;5:1982. https://doi.org/10.1186/s40064-016-3637-8
56. Karmaker T, Dutta S. Prediction of short-term morphological change in large braided river using 2D numerical model. J Hydraul Eng. 2016;142(10). https://doi.org/10.1061/(ASCE)HY.1943-7900.0001167
57. Morianou GG, Kourgialas NN, Karatzas GP, Nikolaidis NP. Assessing hydro-morphological changes in Mediterranean stream using curvilinear grid modeling approach – climate change impacts. Earth Sci Inform. 2018;11:205–216. https://doi.org/10.1007/s12145-017-0326-2
58. Wang Q, Peng W, Dong F, Liu X, Ou N. Simulating flow of an urban river course with complex cross sections based on the MIKE 21 FM model. Water. 2020;12(3):761. https://doi.org/10.3390/w12030761
59. Pareta K. Morphological dynamics of braided river near Bogibeel bridge, Assam. Int J Environ Plan Manag. 2021;7(3):72–86. https://www.semanticscholar.org/paper/Morphological-Dynamics-of-Braided-River-Near-Assam-Pareta/1e5ab6aecec070f531aef7da770f1abf2ac1507e
60. Le Xuan T, Nguyen Cong P, Vo Quoc T, Tran QQ, Wright DP, Anh DT. Multi-scale modelling for hydrodynamic and morphological changes of breakwater in coastal Mekong Delta in Vietnam. J Coast Conserv. 2022;26:18. https://doi.org/10.1007/s11852-022-00866-3
61. Sarker S. Separation of floodplain flow and bankfull discharge: application of 1D momentum equation solver and MIKE 21C. CivilEng. 2023;4(3):933–948. https://doi.org/10.3390/civileng4030050
62. Samir F. The impact of flow reduction on the river morphology during bridge rehabilitation. Ain Shams Eng J. 2025;16(5). https://doi.org/10.1016/j.asej.2025.103359
63. Jiang C, Parteli JR, Shao Y. A model for regional-scale water erosion and sediment transport and its application to the Yellow River Basin. J Adv Model Earth Syst. 2025;7(5). https://doi.org/10.1029/2024MS004593
64. Coleman JM. Brahmaputra river: channel processes and sedimentation. Sediment Geol. 1969;3(2–3):129–239. https://doi.org/10.1016/0037-0738(69)90010-4
65. Fischer S, Pietroń J, Bring A, Thorslund J, Jarsjö J. Present to future sediment transport of the Brahmaputra River: reducing uncertainty in predictions and management. Reg Environ Change. 2017;17:515–526. https://doi.org/10.1007/s10113-016-1039-7

66. Yannan J, Haining H. A new era for Tibet's rivers. Dialogue Earth. 2011. https://dialogue.earth/en/energy/4055-a-new-era-for-tibet-s-rivers/
67. Mahanta C, et al. Physical assessment of the Brahmaputra River. Dhaka: IUCN, International Union for Conservation of Nature; 2014. p.xii + 74. https://portals.iucn.org/library/sites/library/files/documents/2014-083.pdf
68. Samaranayake N, Limaye S, Wuthnow J. Water resource competition in the Brahmaputra River Basin: China, India and Bangladesh. CAN analysis and solution; 2016. https://www.cna.org/archive/CNA_Files/pdf/cna-brahmaputra-study-2016.pdf
69. Yasuda Y, Aich D, Hill D, Huntjens P, Swain A. Transboundary water cooperation over the Brahmaputra River: legal political economy analysis of current and future potential cooperation. The Hague: The Hague Institute for Global Justice; 2017. https://siwi.org/wp-content/uploads/2018/01/brahmaputra-basin-report-final_design.pdf
70. Palash W, Bajracharya SR, Shrestha AB, Wahid S, Hossain MS, Mogumder TK, Mazumder LC. Climate change impacts on the hydrology of the Brahmaputra River Basin. Climate. 2023;11(1):18. https://doi.org/10.3390/cli11010018
71. Mahanta C, Zaman AM, Newaz SMS, Rahman SMM, Mazumdar TK, Choudhury R, Borah PJ, Saikia L. Physical assessment of the Brahmaputra River: ecosystems for life, a Bangladesh-India initiative. Dhaka: IUCN, International Union for Conservation of Nature; 2014. https://portals.iucn.org/library/sites/library/files/documents/2014-083.pdf
72. Chauhan P, Singh N, Chauniyal DD, et al. Differential behaviour of a Lesser Himalayan watershed in extreme rainfall regimes. J Earth Syst Sci. 2017;126:22. https://doi.org/10.1007/s12040-017-0796-0
73. Rao MP, Cook ER, Cook BI, et al. Seven centuries of reconstructed Brahmaputra River discharge demonstrate underestimated high discharge and flood hazard frequency. Nat Commun. 2020;11:6017. https://doi.org/10.1038/s41467-020-19795-6
74. Vaithiyanathan P, Ramanathan AL, Subramanian V. Erosion, transport and deposition of sediments by the tropical rivers of India. In: Sediment budgets, proceedings of the Porto Alegre Symposium. IAHS Publ No. 174; 1988. https://iahs.info/uploads/dms/iahs_174_0561.pdf
75. Raff JL, Goodbred SL, Pickering JL, et al. Sediment delivery to sustain the Ganges-Brahmaputra delta under climate change and anthropogenic impacts. Nat Commun. 2023;14:2429. https://doi.org/10.1038/s41467-023-38057-9
76. Jiang C, Zhang L, Li D, Li F. Water discharge and sediment load changes in China: change patterns, causes, and implications. Water. 2015;7(10):5849–5875. https://doi.org/10.3390/w7105849
77. Zhang L, Ssu F, Yang D, Hao Z, Tong K. Discharge regime and simulation for the upstreams of major rivers over Tibetan Plateau. J Geophys Res Atmos. 2013;118(15):8500–8515. https://doi.org/10.1002/jgrd.50665
78. Sarma JN. Water resources of the Brahmaputra: viabilities and apprehensions of its transfer to other rivers. In: Proceedings of the National Seminar on Linking the Major Rivers of India, Possibilities and Apprehensions. Assam Science Society; 2003. https://www.researchgate.net/publication/282866677_WATER_RESOURCES_OF_THE_BRAHMAPUTRA_VIABILITIES_AND_APPREHENSIONS_OF_ITS_TRANSFER_TO_OTHER_RIVER
79. Pangare G, Nishat B, Liao X, Qaddumi HM. The restless river. Washington (DC): World Bank; 2021. https://documents1.worldbank.org/curated/en/267471631520173475/pdf/The-Restless-River-Yarlung-Tsangpo-Siang-Brahmaputra-Jamuna.pdf
80. WAPCOS. Morphological studies of the river Brahmaputra. New Delhi: Northeastern Council, Govt. of India; 1993.
81. Langendoen EJ. CONCEPTS – conservational channel evolution and pollutant transport system, stream corridor version-1(i). Research report no. 16. Oxford (MS): USDA-ARS National Sedimentation Laboratory; 2000. https://www.ars.usda.gov/ARSUserFiles/60600505/TechnicalReports/NSLTechnicalReport16.pdf
82. Pareta K. Two-dimensional morphological model for prediction of erosion of a reach of Brahmaputra River using MIKE 21C software with hydrodynamics and river

morphology modules. River. 2023;2:445–456. https://onlinelibrary.wiley.com/doi/full/10.1002/rvr2.64
83. Bhattacharya NN, Bora AK. Floods of the Brahmaputra River in India. Water Int. 1997;22(4). https://lib.icimod.org/records/gwqhb-h2766
84. Roy NG, Sinha R. Linking hydrology and sediment dynamics of large alluvial rivers to landscape diversity in the Ganga dispersal system, India. Earth Surf Process Landf. 2016;42(7):1078–1091. https://doi.org/10.1002/esp.4074
85. Word JQ, Kauwling TJ, Mearns AJ. A comparative field study of benthic sampling devices. Task report to the US Environmental Protection Agency (EPA Grant No. R801152); 1976.
86. Stubbs HH, Diehl DW, Hershelman GP. A Van Veen grab sampling method. Technical report 276. Southern California Coastal Water Research Project Authority; 1987. https://ftp.sccwrp.org/pub/download/DOCUMENTS/TechnicalReports/0204_VanVeen.pdf
87. Amsterdam EV. Construction materials for civil engineering. Juta and Company Ltd; 2000. p.16.
88. ASCE. Sediment transportation mechanics – sediment discharge formulas. Task Committee for Preparation of Sediment Manual, Committee on Sedimentation of the Hydraulics Division. J Hydraul Div. 1971;97(4). https://ascelibrary.org/doi/abs/10.1061/JYCEAJ.0002933
89. Goswami DC. Brahmaputra River, Assam, India: physiography, basin denudation, and channel aggradation. Water Resour Res. 1985;21(7):959–978. https://doi.org/10.1029/WR021i007p00959
90. Karmakar P, Das PK, Sarkar S, Karmakar S, Mazumdar D. Association study between lead and zinc accumulation at different physiological systems of cattle by canonical correlation and canonical correspondence analyses. Environ Ecol. 2010;28(4):2321–2325.
91. Akbar Z, Pasha GA, Tanaka N, Ghani U, Hamidifar H. Reducing bed scour in meandering channel bends using spur dikes. Int J Sediment Res. 2024;39(2):243–256. https://doi.org/10.1016/j.ijsrc.2024.01.001
92. Koohizadeh Dehkordi A, Fatahi Nafchi R, Samadi-Boroujeni H, Khastar Boroujeni M, Ostad-Ali-Askari K. Assessment of morphological changes of riverbank erosion using Landsat satellite time-series images. Ain Shams Eng J. 2024;15(3):102455. https://doi.org/10.1016/j.asej.2023.102455
93. Zhang GH, Luo RT, Cao Y, Shen RC, Zhang XC. Impacts of sediment load on Manning coefficient in supercritical shallow flow on steep slopes. Hydrol Process. 2010;24(6):3909–3914. https://doi.org/10.1002/hyp.7892
94. Engelund F, Hansen E. A monograph on sediment transport in alluvial streams. Copenhagen: Teknisk Forlag, Danish Technical Press, Danish Technological University; 1967. http://resolver.tudelft.nl/uuid:81101b08-04b5-4082-9121-861949c336c9
95. Benavides-Munoz HM, Roman-Aguilar KM. Hydrodynamic modeling and flood mitigation strategies in an Andean valley city. PLOS Water. 2025;4(7):e0000397. https://doi.org/10.1371/journal.pwat.0000397

© 2025 by the authors. Licensee SCU, Ahvaz, Iran. This article is an open access article distributed under the terms and conditions of the Creative Commons Attribution 4.0 International (CC BY 4.0 license) (http://creativecommons.org/licenses/by/4.0/).

Optimization of Static Operating Rule Curves for Gated Spillways of Dams Under Flood Conditions

Mohammadreza Masoudimoghaddam[1], Saman Espahbodinia[1], Jafar Yazdi[1*], Maedeh Behifar[2], Jamal Aghayari[2]

1. Department of Water Resources Engineering, Faculty of Civil, Water and Environmental Engineering, Shahid Beheshti University, Tehran, Iran.
2. Iranian Space Research Institute, Tehran, Iran.

***Corresponding Author:**
Jafar Yazdi

Email: j_yazdi@sbu.ac.ir
Received: 2026.01.02
Accepted: 2026.06.15
J. Hydraul. Struct., 2026; 12(4):42-59
DOI: 10.22055/jhs.2026.51390.1372

ABSTRACT

Optimal operation of dam reservoirs plays a vital role in mitigating flood-induced damages. This study introduces a novel approach to develop static operating rules for gated spillways, aiming to derive a set of robust operational policies that perform consistently across a wide range of flood scenarios without requiring complex real-time optimization. To this end, an integrated framework was developed by coupling a Genetic Algorithm (GA) with the Storm Water Management Model (SWMM), a dynamic hydraulic simulation model developed by the U.S. Environmental Protection Agency (EPA). The objective function was defined as minimizing the sum of peak outflows, and a comprehensive set of operational and safety constraints was incorporated to ensure the realism of the solutions. The results demonstrated that the derived optimal rules could reduce the peak outflow by 8% to 57% compared to the baseline scenario (fully open gates during floods), with an average reduction of 21.6% across the analyzed flood events. Performance analysis revealed that this success stems from an intelligent strategy based on the optimal utilization of the reservoir's storage capacity and controlled flow releases. By providing a set of fixed, operational, and efficient rules, this research offers a reliable tool to directly enhance the safety of downstream communities at no extra cost. Furthermore, its methodological framework is generalizable for developing similar operating policies in large, multi-reservoir systems.

KEYWORDS
Flood Control, Reservoir Operation, Genetic Algorithm, Static Operating Rules, Gated Spillways, SWMM, Hydraulic Modeling.

1. Introduction

The effective management of water resources and the control of floods are of escalating global importance, especially given the increased occurrence of extreme climatic events. Dams, as one of the most significant components of water infrastructure, fulfill a crucial function in water storage, power generation, and particularly in diminishing the damage caused by floods. However, optimizing the operation of dam reservoirs under flood conditions is a complex and multifaceted challenge. It requires accounting for diverse, and at times contradictory, objectives, hydraulic and operational limitations, and the intrinsic uncertainties associated with forecasting inflows. The body of research in this domain has undergone a notable transformation from classical models to integrated, intelligent frameworks. Initial studies, such as the work by Unver and Mays [1], were centered on nonlinear programming.

With subsequent growth in computational power, Genetic Algorithms (GA) and their derivatives emerged as principal instruments in this field. For example, Lei et al. [2] established the superiority of the multi-objective NSGA-II algorithm over single-objective GA in deriving operational rules. This trajectory continued with the development of other evolutionary algorithms like DREAM for tackling complex problems [3] and models based on game theory (MOGM) to manage conflicts among stakeholders [4]. Recent research efforts have increasingly focused on hybrid optimization algorithms. These approaches aim to combine the strengths of different metaheuristic methods while mitigating their individual limitations. For example, a novel hybrid algorithm known as F-HGAPSO integrates Genetic Algorithms (GA) and Particle Swarm Optimization (PSO) to address the issue of premature convergence and enhance peak flood reduction performance [5]. Another pivotal theme in this area is addressing uncertainty, especially concerning inflow prediction. Scholars have utilized a variety of methods for risk and uncertainty analysis, such as Copula-based Monte Carlo simulations [6], dynamic Bayesian networks [7], and vulnerability index analysis [8]. More recently, advancements in artificial intelligence have steered the focus toward employing deep learning models for uncertainty management. As an illustration, Xu et al. [9] put forward an optimization model for dam gate operations that handles prediction uncertainty via deep learning ensemble models; their results indicated a substantial reduction in peak flow and reservoir water level. Robust multi-objective optimization (RMOO) models have also been formulated for decision-making in uncertain scenarios, which mitigate system risk through optimized pre-discharges [10]. Beyond the algorithms themselves, there is a heightening focus on creating comprehensive and operational management frameworks. Research by scholars like Cheng and Chau [11] underscored the necessity of integrated management systems, while other studies have focused on optimizing complex systems that include cascaded reservoirs and flood detention areas [12-14]. Modern approaches, such as optimizing water pre-release with the aid of large-scale data, seek to generate greater vacant capacity in reservoirs ahead of severe flood events [15]. Moreover, extensive review studies conducted by Tariq et al. [16], Jain et al. [17], and Mehta et al. [18] have emphasized the significance of a risk-based approach, finding a balance between conflicting goals, and the imperative for real-time operations. In addition, research is trending towards dynamic decision-making for establishing the optimal reservoir water level in response to variable seasonal conditions, in order to simultaneously optimize resource utilization and flood preparedness [19]. Beyond operational optimization frameworks, accurate hydraulic characterization of gated structures remains a critical component of reliable flood routing and rule derivation. Several recent experimental and data-driven studies have focused on improving the prediction of discharge coefficients for various gate configurations. Laboratory investigations have demonstrated the influence of geometric features such as sills on radial gate discharge coefficients [20], while advanced machine learning approaches—including Gaussian Process Regression [21], genetic programming–based expert systems [22], multiple non-linear regression models [23], and hybrid artificial intelligence techniques such as SVM, ANN, RF, and related methods [24]—have shown strong predictive capability for sluice and oblique gate hydraulics. Furthermore, experimental validation combined with data-driven modeling has enhanced the reliability of discharge estimation for inclined slide gates under different hydraulic conditions [25]. These developments highlight the growing integration of experimental hydraulics and intelligent modeling approaches, which provide a stronger foundation for defining

operational rules in gated dam systems. Despite these wide-ranging advancements, a significant research gap remains: many advanced models necessitate real-time optimization and sophisticated forecasting systems, the implementation of which is arduous or unfeasible for many operational dams. In contrast, there is a compelling need to develop fixed, pre-defined, yet intelligent operating rules capable of delivering stable and dependable performance across a broad spectrum of flood scenarios, without requiring computationally intensive processes during a crisis. Gated dams present unique operational challenges compared to ungated (overflow) dams. Unlike ungated systems, where discharge is primarily governed by the reservoir water level and spillway geometry, gated dams require active and timely gate manipulation to regulate outflow. This introduces additional complexity, including the need for coordinated gate operations, rapid decision-making under uncertain inflow conditions, and the risk of operational or mechanical failure. In flood situations, improper gate management may lead either to excessive downstream discharge or to dangerous water level rise within the reservoir. Therefore, developing robust and predefined operating rules for gated systems is particularly important to enhance safety and reduce reliance on real-time subjective decisions. This research aims to bridge this gap by concentrating on gated dams. The principal objective of this study is the development and assessment of a suite of optimal and practical operating rules for the gated structures of a dam, utilizing a genetic algorithm and precise SWMM hydraulic modeling. The innovation of this research is centered on presenting a method to attain operating rules that exhibit robust performance under varied flood scenarios. This objective is realized through the formulation of an optimization problem with a "minimize the sum of peak outflows" objective function, as well as through the precise application and calibration of a comprehensive set of operational and physical constraints. This methodology results in the generation of logical and defensible rules, which can serve as a practical tool for dam managers and operators to enhance decision-making and augment safety under flood conditions.

2. Materials and Methods

2.1. Study Area

For this research, the Dez Dam and its reservoir were selected as the case study. Dez Dam is a double-arch concrete dam constructed on the Dez River, one of the most voluminous and sediment-laden rivers in western Iran. It is located 23 km northeast of Andimeshk in the Zagros Mountains (Figure 1). The construction of the dam was completed in 1962 (1341 in the Iranian calendar). The geographical location of the dam and its catchment basin is shown in Figure 1. With a height of 203 meters, it was considered one of the tallest dams in the world at the time of its construction. The primary objectives for its construction were to supply irrigation water for 125,000 hectares of downstream land, generate hydroelectric power, and control the region's seasonal floods.

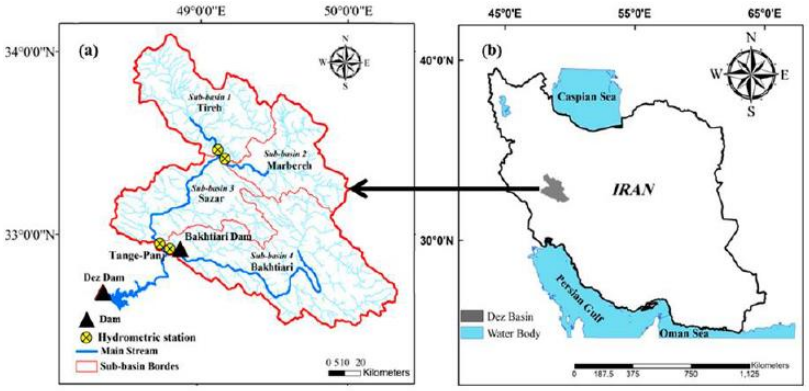


Figure 1: Location map of the Dez Dam and reservoir.

The dam has multiple outlet structures. To meet downstream irrigation demands, three conical valves were installed at an elevation of 222.7 meters, each capable of releasing 60 m³/s. However, these valves have been buried under heavy sedimentation since approximately 2001 (the year 1380) and have effectively lost their functionality. Two spillway tunnels, with diameters of 14 and 12.6 meters, are located at an elevation of 290 meters to discharge large floods, each capable of releasing a flow of 3000 m³/s. The dam's powerhouse, with eight 65 MW units, has a maximum energy production capacity of 520 MW, with its water supplied through two intakes at an elevation of 270 meters. Figure 2 shows a purely schematic (symbolic) arrangement of Dez Dam outlets and operational status (this figure does not reflect actual scale or exact component locations). Figure 3 shows the monthly inflow and outflow volumes for the Dez Dam reservoir between 1997 and 2015 (Persian years 1376 to 1394).

To evaluate and optimize the dam's performance under critical conditions, a set of significant historical flood events entering the reservoir was selected as the model's input scenarios. Figure 4 displays the hydrographs of these notable flood events. As can be seen, these events cover a wide spectrum of hydrological characteristics, from floods with a peak discharge of less than 1,000 m³/s to very large floods with peaks approaching 7,000 m³/s. This diversity in volume, shape, and timing of the flood peak clearly demonstrates the necessity of developing robust operating rules that can perform effectively against a wide range of threats.

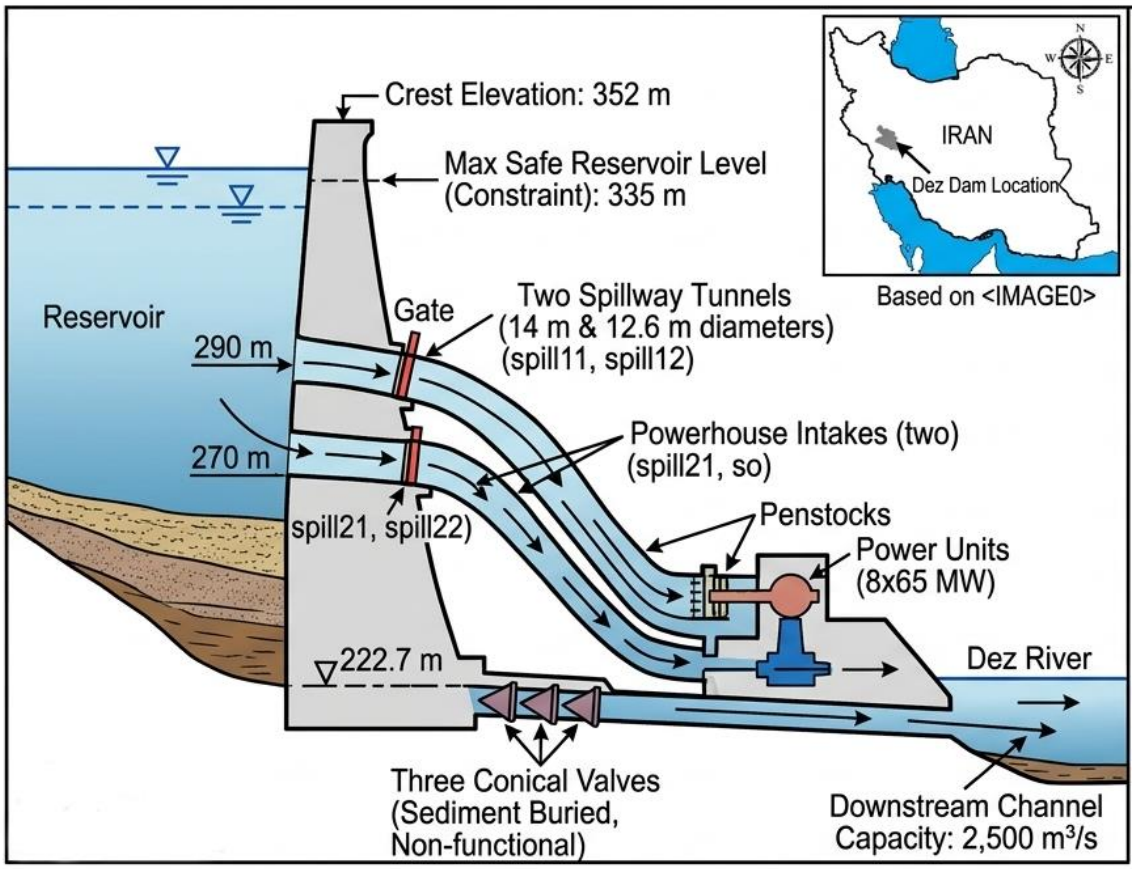


Figure 2: Schematic (symbolic) representation of Dez Dam outlet arrangement and operational status (Not to scale; does not represent actual dam geometry or exact component locations)

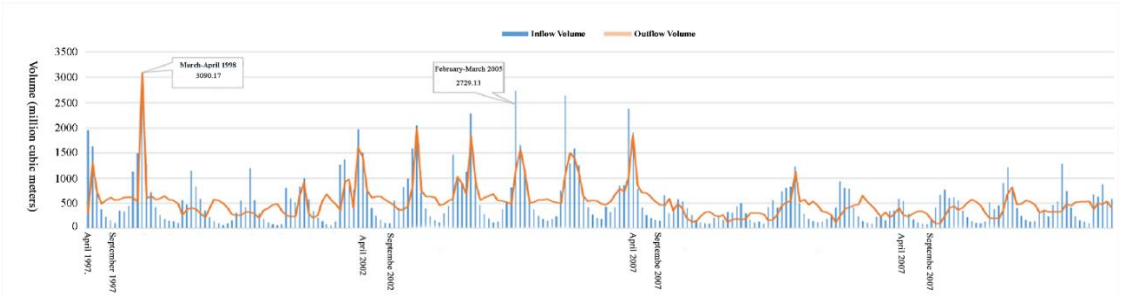


Figure 3: Monthly inflow and outflow volume (million cubic meters, MCM) for the Dez Dam reservoir between 1997 and 2015

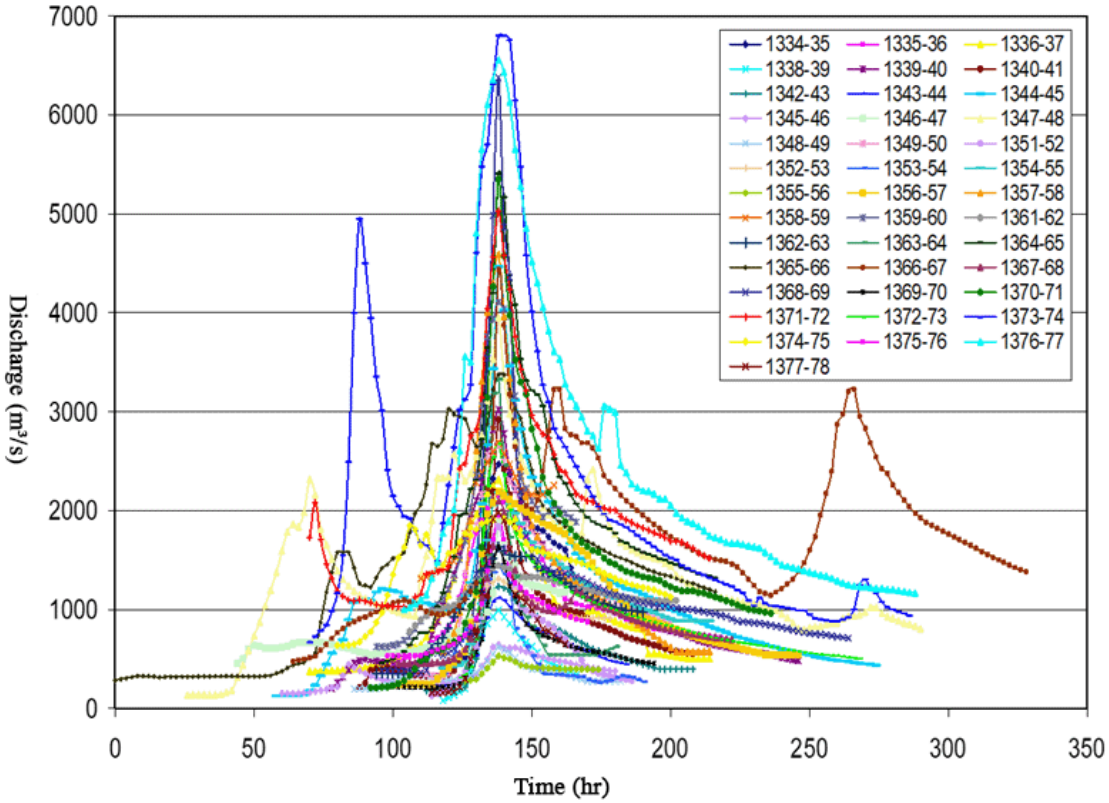


Figure 4: Hydrographs of some of the most significant inflow events to the Dez Dam (Persian years).

2.2. Reservoir Routing Model

To accurately simulate the hydraulic behavior of the dam reservoir and perform flood routing within the system, the Storm Water Management Model (SWMM), developed by the United States Environmental Protection Agency (EPA), was used. SWMM is a dynamic rainfall–runoff and hydraulic simulation model capable of performing continuous or event-based simulations of unsteady flow in complex water systems. It solves the full one-dimensional Saint-Venant equations, allowing detailed representation of storage units, hydraulic structures, conduits, and control elements. Due to its robust numerical engine and flexibility in modeling hydraulic structures such as gates, spillways, and outlets, SWMM provides a reliable platform for simulating reservoir routing and operational scenarios under flood conditions. Due to its advanced capabilities in dynamic and unsteady flow simulation in complex systems, this model is considered a powerful and reliable tool for analyzing hydro-hydraulic systems such as dams, canals, and rivers. The base model of the Dez reservoir, which includes the

geometric and hydraulic characteristics of the reservoir, spillways, and other related structures, was implemented in an input file. To evaluate the performance of the operating rules under various conditions, a set of real and historical flood hydrographs was used. These hydrographs, representing diverse flood scenarios with different return periods and volumes, were extracted from the historical series of inflow data and applied as input to the model. A key aspect of this study's methodology is the dynamic coupling between the optimization model (written in Python) and the SWMM simulation engine. This connection was established using the pyswmm library. Unlike traditional methods where control rules are statically defined in the [CONTROLS] section of the SWMM input file, this section was bypassed in our research. Instead, to evaluate each set of operating rules (each "individual" in the genetic algorithm), the SWMM simulation loop was controlled step-by-step by a Python script. At each time step, the script reads the instantaneous water level in the reservoir from the SWMM model, calculates the optimal gate opening percentage for each of the four outlets based on the operating rules being tested, and then applies these new settings back to the SWMM model. This dynamic process enabled a precise and realistic real-time evaluation of each set of operating rules, providing key variables such as outflow discharge and reservoir water level to the optimization algorithm for calculating the objective function and penalties. The complete dynamic coupling process between the Python optimization model and the SWMM engine is presented as a flowchart in Figure 5.

2.3. Optimization Framework

To find the optimal operating rules for the outlet gates of Dez Dam, an optimization framework based on a Genetic Algorithm (GA) was developed. As a powerful metaheuristic search method, the Genetic Algorithm is capable of solving complex, nonlinear problems with large search spaces, which is why it was selected for this research. The entire optimization process was implemented in the Python programming language, utilizing the robust and efficient DEAP (Distributed Evolutionary Algorithms in Python) library.

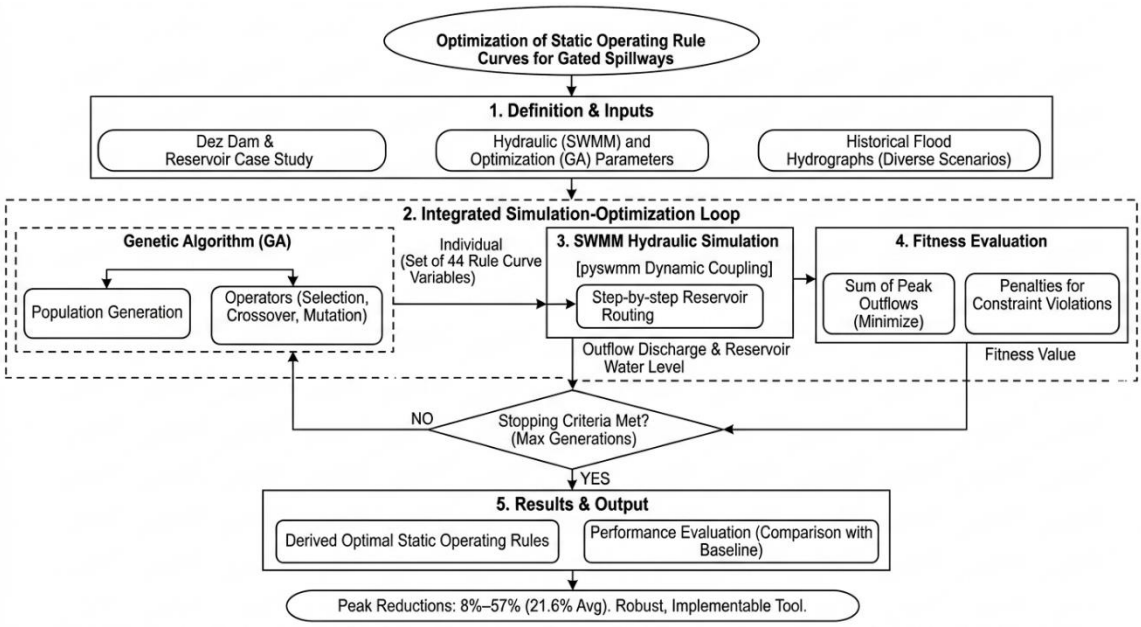


Figure 5: Flowchart of the dynamic coupling between the Python-based optimization model (GA) and the SWMM simulation engine via pyswmm

2.3.1. Decision Variables

The decision variables in this optimization problem consist of a set of 44 variables that define the piecewise constant rule curves for the dam's two spillways and two power tunnels (spill11, spill12, spill21, spill22). Each of these 44 variables represents the gate opening percentage (a continuous value from 0 to 100) for a specific gate within a defined range of reservoir water depth. To enhance the model's precision and flexibility, the depth intervals were defined in 5-meter increments; the rules for the upper-level gates (spill11, spill12) start at a depth of 70 meters, while the rules for the upper lower-level gates (spill21, spill22) begin at 90 meters. The 5-meter depth increment was selected as a compromise between operational resolution and computational tractability. Preliminary sensitivity analyses were conducted using smaller depth intervals (e.g., 2–3 meters); however, these significantly increased the number of decision variables and computational burden without yielding meaningful improvements in peak reduction performance. Therefore, the 5-meter discretization was considered sufficiently detailed to capture operational behavior while maintaining algorithm efficiency. Each chromosome in the genetic algorithm is a 44-element vector representing a complete set of these operating rules.

2.3.2. Objective Function

The main goal of this research is to develop rules that can effectively and sustainably control the peak outflow across a wide range of flood scenarios. Accordingly, the objective function that the GA aims to minimize was defined as the "sum of peak outflows across all simulated flood events". This choice, as opposed to minimizing only a single maximum peak, steers the algorithm toward finding more robust solutions that exhibit acceptable performance against both small and large floods. The final fitness value of each individual in the population is calculated from the sum of this primary objective function and the sum of weighted penalties incurred from violating operational constraints. To provide a clearer mathematical representation, the overall fitness function is defined as:

$$F = \sum_{i=1}^{N} Q_{peak.i} + \sum_{j=1}^{M} W_j, P_j \quad (1)$$

where:

- $Q_{peak,i}$ represents the peak outflow corresponding to flood event i,
- N is the total number of simulated flood events,
- P_j denotes the penalty term associated with constraint j,
- w_j is the weighting coefficient assigned to constraint j,
- M is the total number of defined operational and safety constraints.

Each penalty term is activated only when a constraint violation occurs and is proportional to the magnitude of violation. Larger violations result in proportionally larger penalty values, thereby steering the optimization process toward feasible and operationally defensible solutions.

2.3.3. Constraints and Penalty Functions

One of the key innovations of this study is the definition and precise calibration of a comprehensive set of operational and safety constraints to ensure that the optimized rules are not only mathematically optimal but also logical and defensible from an engineering and operational standpoint. The violation of any of these constraints adds a penalty to the individual's fitness value, proportional to the severity of the violation. These constraints, defined based on standard principles of dam engineering and water resources management, include the following:

a) **Dam Safety Constraint:** To prevent any risk to the dam's stability, the water level

must not exceed the maximum safe reservoir level (typically the dam crest or the top of the flood control pool). This constraint is the most critical in dam operation, and its observance takes precedence over all other objectives [26]. In this study's dam, the maximum safe level was set at 335 meters, and any solution causing the water level to surpass this limit was effectively eliminated from the optimization process by receiving a very large penalty (1e12).

b) **Operational Guide Curve:** To balance water storage for uses like agriculture and energy production with creating empty storage for flood control, an operational guide curve or target level is used. Optimal operation aims to keep the reservoir water level as close as possible to this curve [27]. In this research, the target level was defined as 308 meters, and deviations from this level were controlled with two separate penalty factors (for higher and lower levels).

c) **Ramping Rate Constraint:** To prevent sudden and drastic changes in the released flow, which can cause erosion of the riverbed and banks, endanger human life, and harm the downstream ecosystem, the rate of change of the outflow is limited [28]. In this study, the maximum allowable rate of change for the total outflow was set to 3,000 m^3/s per hour.

d) **Downstream Channel Capacity:** The outflow from the dam must always be less than the maximum safe capacity of the downstream channel to prevent flooding and damage to residential and agricultural areas. This constraint is a primary objective in reservoir operation for flood control [29]. Accordingly, the maximum safe discharge capacity of the downstream channel was assumed to be 2,500 m^3/s.

e) **Operational Stability Constraints:** To extend the service life of the equipment and prevent rapid, high-wear maneuvers, two additional constraints were defined:

i) **Limiting the rate of change of the reservoir water level:** Rapid changes in the reservoir level can jeopardize the stability of the reservoir's bank slopes. Therefore, limiting the drawdown rate is a critical consideration for safe operation [30]. In this research, this rate was limited to 1 meter per hour.

ii) **Limiting gate adjustment changes:** Frequent and rapid gate maneuvers lead to increased wear and tear on mechanical and hydraulic equipment. Limiting the amount of gate setting changes in short time steps is a standard operational practice to increase the lifespan and reliability of the structures. In this study, the maximum allowable change in any gate's setting in a single simulation time step was set to 50%.

2.3.4. Genetic Algorithm Parameters

The main parameters of the Genetic Algorithm, which control its performance, were configured as follows after preliminary investigations and based on experience from similar studies, considering the 44 decision variables in the problem:

- Population Size: 140
- Max Generations: 1000
- Crossover Probability: 0.8
- Mutation Probability: 0.2
- Genetic Operators: Tournament selection, Simulated Binary Crossover (SBX), and Polynomial Bounded mutation were used. The eta (η) parameter, which controls the distribution of offspring from these operators, was set to 20.0.

3. Results

This section presents the results from the optimization process and the performance evaluation of the optimal operating rules. First, the performance and convergence of the optimization algorithm are described. Then, the derived optimal rules are presented. Finally, the hydraulic performance of these rules in controlling various floods is evaluated and compared with the baseline scenario.

3.1. Performance and Convergence of the Optimization Algorithm

The optimization process was executed using the genetic algorithm for 1000 generations with a population of 140 individuals. Throughout the algorithm's execution, the fitness value of the best individual in each generation was continuously monitored. Observations showed that in the initial generations, the fitness value decreased sharply due to the high diversity of the population, indicating the algorithm's rapid movement toward desirable regions of the search space. As the generations progressed, this rate of improvement gradually slowed, and in the final generations, the best fitness value converged to a nearly stable and constant level. This convergence behavior indicates that the algorithm successfully reached an optimal or near-optimal solution and that further generations would not yield significant improvements, thereby confirming the validity and efficiency of the optimization process. The complete optimization process (1000 generations with a population size of 140) required approximately several days of computational time on a standard desktop computer (Intel i7 processor, 16 GB RAM). This computational demand is associated with the repeated dynamic coupling between the Genetic Algorithm and the SWMM hydraulic simulation for multiple flood scenarios. It should be emphasized that this optimization is performed offline for rule derivation purposes only. Once the optimal static operating rules are obtained, their implementation does not require any further computational effort, making the approach practically feasible for real-world dam operation.

3.2. Optimal Operating Rules

The final output of the optimization process is a set of 44 decision variables that constitute the optimal operating rules for the Dez Dam spillways. These rules specify the optimal opening percentage for each of the four dam gates at different reservoir water levels. The complete details of these derived rules are presented in Table 1. This table effectively represents the optimal guide curve that forms the basis for the dam's operation under flood conditions. This curve reveals an intelligent, nonlinear strategy discovered by the algorithm. A key feature is the reduction in gate opening at intermediate water levels (approximately 280 to 295 meters). This action allows the reservoir to absorb and attenuate the flood wave by utilizing its storage capacity. Subsequently, at higher levels, the gate is opened rapidly to release the flow in a controlled manner, thereby ensuring the dam's safety. This dynamic behavior is significantly more efficient than a simple, linear rule.

3.3. Hydraulic Performance Evaluation of the Optimal Rules

To evaluate the operational efficiency of the derived optimal rules, they were applied to several different flood scenarios within the SWMM hydraulic model. The performance of these rules was compared with two other hydrographs: the reservoir inflow hydrograph and the outflow hydrograph from the baseline scenario (all gates fully open). The results of this comparison for nine extreme flood events are displayed in Figure 6. Also, for easier interpretation, these optimal rules are also presented graphically in Figure 7, which shows the opening percentage of each gate as a function of reservoir water level.

Table 1. Derived optimal operating rules for the Dez Dam gates.

Row	Gate Name	Water Level (m)	Opening Percentage (%)
1	spill11	275	40.37
2	spill11	280	69.3
3	spill11	285	47.28
4	spill11	290	6.8
5	spill11	295	2.65
6	spill11	300	0.1
7	spill11	305	36.74
8	spill11	310	94.94
9	spill11	315	94.58
10	spill11	320	21.53
11	spill11	325	86.07
12	spill11	330	92.23
13	spill11	335	58.39
14	spill12	275	23.75
15	spill12	280	87.45
16	spill12	285	16.24
17	spill12	290	24.56
18	spill12	295	0.03
19	spill12	300	0.03
20	spill12	305	57.16
21	spill12	310	16.02
22	spill12	315	92.73
23	spill12	320	4.26
24	spill12	325	21.07
25	spill12	330	46.16
26	spill12	335	14.33
27	spill21	295	17.2
28	spill21	300	3.05
29	spill21	305	16.41
30	spill21	310	33.26
31	spill21	315	75.65
32	spill21	320	60.05
33	spill21	325	5.67
34	spill21	330	98.41
35	spill21	335	42.07
36	spill22	295	2.6
37	spill22	300	28.6
38	spill22	305	49.73
39	spill22	310	68.08
40	spill22	315	46.66
41	spill22	320	82.13
42	spill22	325	3.41
43	spill22	330	2.04
44	spill22	335	48.34

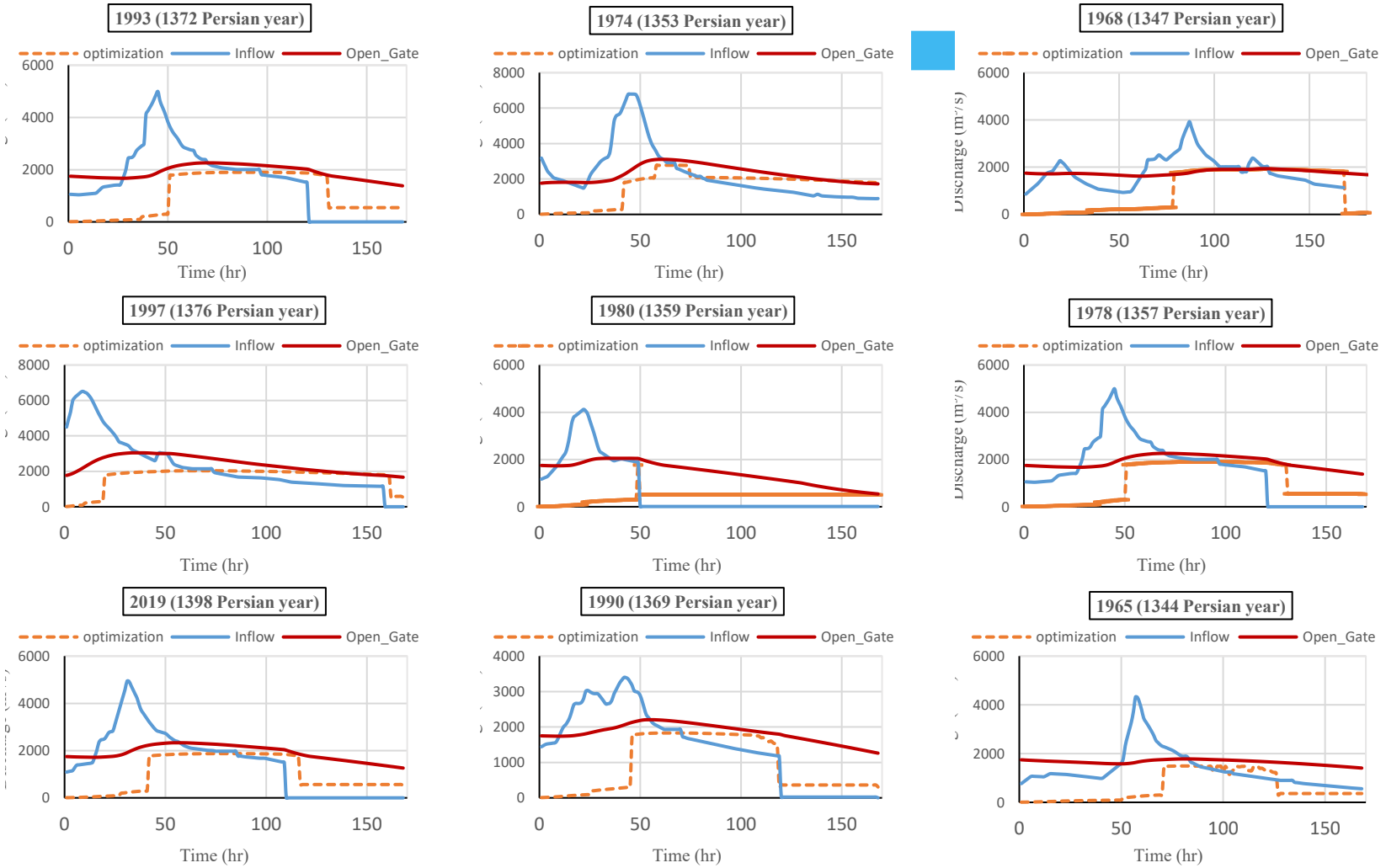


Figure 6: Comparison of inflow, optimal outflow, and baseline outflow (fully open gates) hydrographs for 9 different flood events.

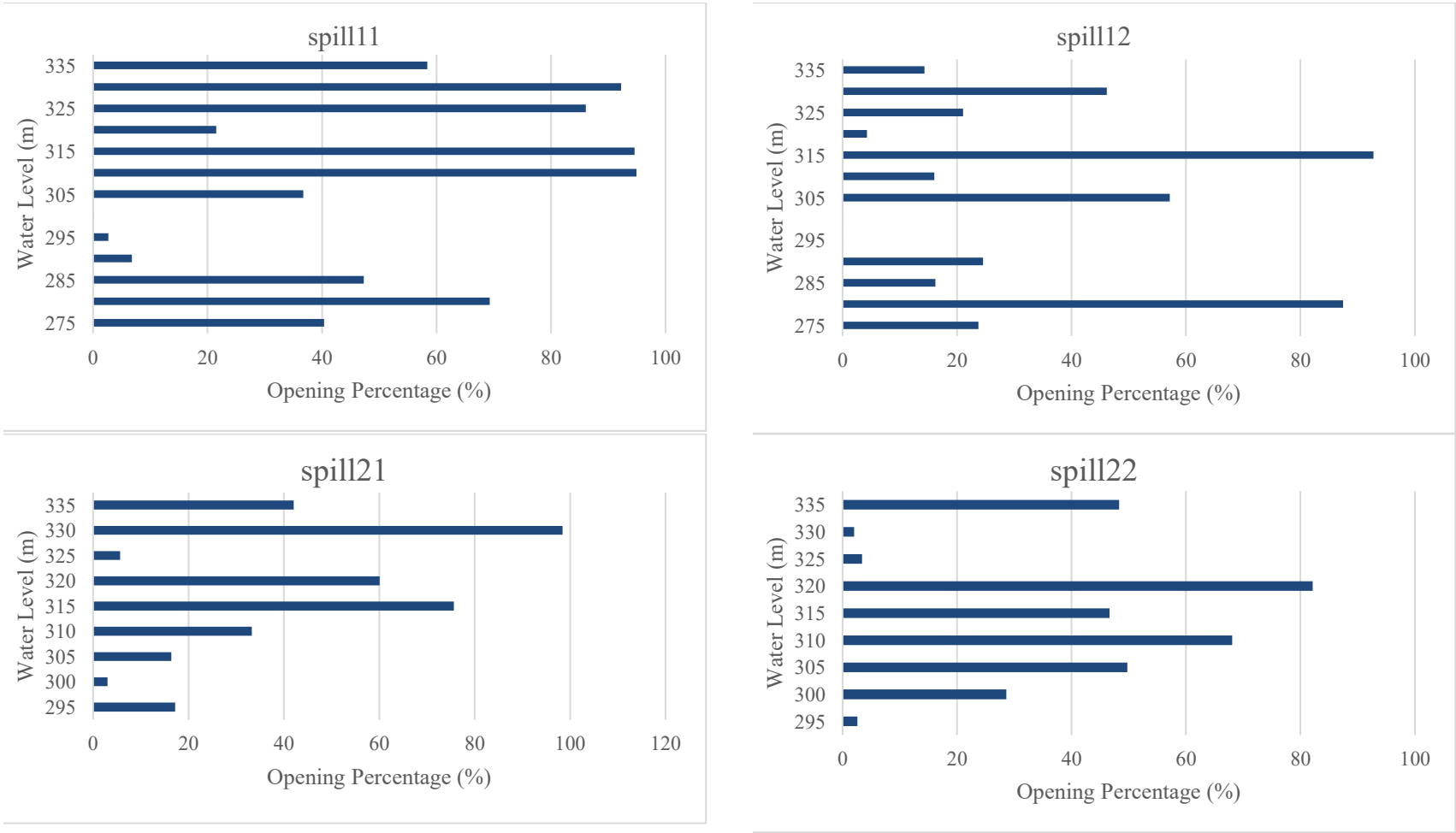


Figure 7: Optimal gate opening percentage curves for spill11, spill12, spill21, and spill22 as a function of reservoir water level.

The diagrams in Figure 6 clearly illustrate that the optimal operating rules have effectively attenuated the incoming flood peaks. Across all investigated scenarios, the peak outflow under the optimal rules (the 'Optimization' plot) is substantially lower than the peak outflow from the baseline scenario (the 'Open_gate' plot). This finding indicates that the optimization approach yields a far more efficient strategy compared to a simplistic, static alternative.

In analyzing the results, it's important to note the differentiated behavior of the optimal strategy when faced with floods of varying magnitudes. The primary objective of this study is the control of large, destructive floods that have the potential to cause downstream damage. According to the operational constraints defined in the model, the safe discharge capacity of the downstream channel is assumed to be 2500 m^3/s. Floods with a peak inflow below this threshold are not considered a significant threat and can pass through the system without causing damage or requiring complex optimization maneuvers. Consequently, the optimization process and performance analysis are appropriately focused on major flood scenarios where reducing the peak outflow is of high operational importance and directly contributes to enhancing the safety of the downstream community. For this reason, a detailed analysis of minor flood events, for which optimization yields no significant risk reduction, is omitted from this section. Among the analyzed events, Event 47 exhibited the highest peak reduction (57.1%). A closer examination of its hydrograph reveals that this flood was characterized by a relatively sharp and concentrated peak combined with moderate total volume. This configuration allowed the reservoir to effectively absorb a substantial portion of the inflow before reaching critical water levels. Consequently, the optimized rules were able to delay and attenuate the peak discharge significantly. In contrast, floods with longer duration and larger volumes reduce the available storage flexibility, thereby limiting the achievable peak attenuation.

3.4. Summary of Results and Overall Comparison

For a detailed quantitative analysis and a comprehensive comparison of the optimal rules' performance across all scenarios, the key results related to peak flood reduction are summarized in Table 2. This table presents the peak inflow and outflow values for the two operating scenarios (baseline and optimal), along with the percentage of performance improvement achieved through optimization for each of the nine events studied.

Table 2: Summary of results and performance comparison of the optimal rules in reducing peak flood.

Event ID (Year)	Peak Inflow (m^3/s)	Peak Outflow - Baseline (m^3/s)	Peak Outflow - Optimal (m^3/s)	Peak Reduction (%) (relative to baseline)
72	4,991.50	2,227	1,893	15
53	6,749	3,105	2,769	10.8
47	4,500	2,800	1,200	57.1
76	6,464	3,190	2,019.50	36.7
59	4,054	2,051	1,887	8
57	4,992	2,243	1,875.60	16.4
98	4,926	2,326	1,873	19.5
69	3,332	2,126	1,817	14.5
91	4,302	1,781	1,493	16.2
Average	-	-	-	21.6

A review of the quantitative results presented in Table 2 numerically confirms the significant success of the optimization approach. As can be observed, the optimized operating rules performed better than the baseline scenario in all tested scenarios, without exception. The degree of improvement in peak flood reduction varied between 8.0% and 57.1%, depending on the characteristics of the input hydrograph. It should be noted that these nine events were selected as representative samples from a wide range of floods studied. The analysis of other flood events also showed similar results within the same performance range; to avoid verbosity and repetition, their detailed presentation has been omitted here. Considering all scenarios, the optimal rules were able to reduce the peak outflow by an average of approximately 21.6% compared to the baseline scenario. This consistent success in peak reduction across all test scenarios demonstrates the robustness and high efficiency of the solution presented in this research, indicating that these rules can be a reliable tool for significantly increasing the safety of downstream areas.

4. Discussion

The results presented in this research clearly demonstrate that using an optimization framework based on a genetic algorithm, coupled with a hydraulic routing model, can significantly improve the operational performance of the Dez Dam under flood conditions. The consistent success of the optimized rules in reducing peak outflow across all nine diverse flood scenarios highlights the high efficiency and robustness of the adopted approach. This remarkable success is the result of an intelligent operating strategy discovered by the algorithm. Instead of a passive and simplistic reaction, such as fully opening the gates or operating them based on experience, the optimal rules more effectively mitigate the flood peak by utilizing the reservoir's storage volume at the beginning of the flood and then releasing the flow in a controlled and steady manner. This dynamic strategy, a key achievement of this study, shows that with proper temporal and volumetric management, the existing capacity of a dam can be utilized far more efficiently.

When positioning the present results within the broader literature, it is important to consider both performance magnitude and methodological objectives. Previous studies using multi-objective NSGA-II frameworks (e.g., Ref. [2]) or hybrid algorithms such as F-HGAPSO (Ref. [5]) have reported notable improvements in flood control performance under various system configurations. Although direct quantitative comparison is constrained by differences in case studies and modeling assumptions, the peak reduction range achieved in this study (8%–57%, average 21.6%) is consistent with the order of magnitude reported in advanced evolutionary optimization studies. A key distinction, however, lies in the objective of the proposed framework: rather than relying on computationally intensive real-time optimization, this study derives static yet robust operating rules that can be implemented without online computation during flood events.

Of course, achieving this level of optimality was not without its challenges and trade-offs. The process of fine-tuning the six soft operational constraints was itself a significant challenge, requiring a deep understanding of the system's behavior and numerous trial-and-error tests. To reach its primary goal of "minimizing the sum of peaks," the genetic algorithm sometimes had to accept small penalties for violating other constraints. These trade-offs show that in real-world operations, there is no "absolute ideal" solution; rather, the best solution is the point that strikes an optimal balance between conflicting objectives and limitations. The significance of the present work lies in the fact that by defining and applying a comprehensive set of constraints, it guided this balance toward solutions that are not only mathematically optimal but also defensible and logical from an engineering and operational perspective.

Despite these significant achievements, acknowledging the study's limitations is essential for outlining future research directions. One challenge was the single-objective focus of this research on flood control. The Dez Dam is a multipurpose structure with other objectives, such as power generation and water supply, which may conflict with the goal of flood control. The solutions presented here are not necessarily optimal for these other objectives, although an effort was made to meet them by applying operational constraints. These limitations themselves create valuable opportunities for future research. The next step could be to move toward a multi-objective optimization model that simultaneously considers flood control, power generation, and environmental needs, not just for a single dam but for a series of cascaded, parallel, or combined dams. This could provide more comprehensive solutions that are closer to the real needs of operators. Finally, integrating this optimization model with real-time forecasting systems could lead to the creation of a dynamic decision support system, which would be a major step toward modernizing and increasing the management efficiency of the country's large dams.

Overall, by providing a transparent methodology and efficient, stable rules, this research has established a solid and practical foundation for future studies and for the tangible improvement of dam flood management. Despite the demonstrated robustness of the derived rules across multiple historical flood scenarios, sensitivity to inflow uncertainty remains an important consideration. The current framework relies on deterministic historical hydrographs, and therefore its performance depends on the representativeness of these selected events. In real-world applications, forecast errors, nonstationary climate patterns, and extreme outlier events may affect operational outcomes. Future research could extend the proposed methodology by incorporating stochastic Genetic Algorithm variants, ensemble-based inflow generation, or robust optimization techniques that explicitly consider uncertainty bounds. Such extensions would allow the derivation of operating rules that remain effective under probabilistic inflow scenarios and evolving hydrological conditions.

A practical concern that may arise from the optimal rule curves shown in Figure 7 is the presence of rapid variations in opening percentages at certain water level intervals. While these theoretical jumps may appear impractical at first glance, it is important to emphasize that modern dam gate systems are fully automated. Hydraulic or electric actuators, controlled by PLCs, can precisely achieve any required opening percentage without manual intervention. The control system can also interpolate between the discrete 5-meter intervals to ensure smooth transitions. Therefore, the derived rules are entirely feasible with currently available automation technologies, and no operational impracticality exists.

5. Conclusion

This study presented an integrated simulation–optimization framework for deriving static operating rules for gated spillways with a primary focus on flood mitigation. By coupling a Genetic Algorithm (GA) with a detailed hydraulic routing model and incorporating a comprehensive set of operational and safety constraints, the framework produced operational rules capable of consistently reducing peak outflows across diverse flood scenarios.

The results demonstrated that the derived rules achieved peak reductions ranging from 8% to 57%, with an average reduction of 21.6% relative to the baseline scenario. These findings confirm that structured offline optimization can significantly enhance flood control performance while maintaining operational feasibility. Importantly, the developed rules are directly implementable without requiring real-time computational resources, making them suitable for practical dam management contexts.

While the present study focused on a single case study, the methodological framework is transferable to other gated dams with similar hydraulic characteristics. As a practical next step, pilot implementation of the proposed operating rules at other major Iranian dams is recommended to evaluate real-world performance, institutional adaptability, and long-term safety improvements. Such applications would provide valuable empirical evidence for broader adoption and could contribute meaningfully to strengthening national flood risk management strategies.

Declarations

Funding: This research received no external funding.

Conflict of Interest: The authors declare that they have no conflict of interest.

AI Statement: During the preparation of this work, the authors used Gemini (AI model) in order to improve language, enhance readability, and ensure the manuscript conforms to the journal's formatting and referencing guidelines. After using this tool, the authors reviewed and edited the content as needed and take full responsibility for the content of the publication. This tool was used solely for linguistic assistance and not for data analysis, hydraulic simulation, or drawing research insights

Author Contributions: All authors contributed to the study conception and design. Material preparation, data collection, and analysis were performed by M.M. and S.E. The first draft of the manuscript was written by M.M., and all authors (including J.Y., M.B., and J.A.) commented on previous versions of the manuscript. All authors read and approved the final manuscript.

Resources:

1. Unver OI, Mays LW. Model for real-time optimal flood control operation of a reservoir system. Water Resour Manage. 1990;4(1):21–46. https://doi.org/10.1007/BF00429923
2. Lei, X., Zhang, J., Wang, H., Wang, M., Khu, S. T., Li, Z., & Tan, Q. Deriving mixed reservoir operating rules for flood control based on weighted non-dominated sorting genetic algorithm II. J Hydrol. 2018; 564:967–983. https://doi.org/10.1016/j.jhydrol.2018.07.075
3. Diao, W., Peng, P., Zhang, C., Yang, S., & Zhang, X. (2021). Multi-objective optimal operation of reservoir group in Jialing River based on DREAM algorithm. Water Supply, 21(5), 2518-2531. https://doi.org/10.2166/ws.2021.064
4. Yu Y, Zhao R, Zhang J, Yang D, Zhou T. Multi-objective game theory optimization for balancing economic, social and ecological benefits in the Three Gorges Reservoir operation. Environ Res Lett. 2021;16(8):085007. https://doi.org/10.1088/1748-9326/ac1480
5. Cui, G., Qi, Z., Zhao, H., Zhao, R., Wang, H., & Zhao, J. (2025). Application of F-HGAPSO algorithm in reservoir flood control optimal operation. Water Resources Management, 39(4), 1763-1782. https://doi.org/10.1007/s11269-024-04045-x
6. Huang, K., Ye, L., Chen, L., Wang, Q., Dai, L., Zhou, J., ... & Zhang, J. Risk analysis of flood control reservoir operation considering multiple uncertainties. J Hydrol. 2018; 565:672–684. https://doi.org/10.1016/j.jhydrol.2018.08.040
7. Chen, J., Zhong, P. A., An, R., Zhu, F., & Xu, B. Risk analysis for real-time flood control operation of a multi-reservoir system using a dynamic Bayesian network. Environ Model Softw. 2019; 111:409–420. https://doi.org/10.1016/j.envsoft.2018.10.007
8. Yang, Y., Guo, H., Chen, L., Liu, X., Gu, M., & Pan, W. (2020). Multiattribute decision making for the assessment of disaster resilience in the Three Gorges Reservoir Area. Ecology & Society, 25(2). https://doi.org/10.5751/ES-11464-250205
9. XU, Y., LU, H., YU, X., & GUO, Y. Optimization of gate operation for reservoir

flood control based on deep learning ensemble forecasting. Adv Water Sci. 2024. 10.14042/j.cnki.32.1309.2024.06.004

10. Huang, X., Xu, B., Zhong, P. A., Yao, H., Yue, H., Zhu, F., ... & Liu, W. (2022). Robust multiobjective reservoir operation and risk decision-making model for real-time flood control coping with forecast uncertainty. Journal of Hydrology, 605, 127334. https://doi.org/10.1016/j.jhydrol.2021.127334
11. Cheng, C. T., & Chau, K. W. (2004). Flood control management system for reservoirs. Environmental Modelling & Software, 19(12), 1141-1150. https://doi.org/10.1016/j.envsoft.2003.12.004
12. Zhu, D., Mei, Y., Xu, X., Chen, J., & Ben, Y. Optimal operation of complex flood control system composed of cascade reservoirs, navigation-power junctions, and flood storage areas. Water. 2020;12(7):1883. https://doi.org/10.3390/w12071883
13. Wang, K., Wang, Z., Liu, K., Cheng, L., Bai, Y., & Jin, G. Optimizing flood diversion siting and its control strategy of detention basins: A case study of the Yangtze River, China. J Hydrol. 2021; 597:126201. https://doi.org/10.1016/j.jhydrol.2021.126201
14. Yu P, Ma H, Qiu L, Zhang T, Li S. Optimization of a flood diversion gate scheme in flood storage and detention areas based on flood numerical simulation. Front Environ Sci. 2022; 10:978385. https://doi.org/10.3389/fenvs.2022.978385
15. Zhang, L., Feng, Z. K., Yao, X. R., Niu, W. J., Wang, Y. Q., & Mo, L. A multi-objective operation optimization method for dynamic control of reservoir water level in evolving flood season environments. J Hydrol. 2024; 643:131940. https://doi.org/10.1016/j.jhydrol.2024.131940
16. Tariq MAUR, Farooq R, Van de Giesen N. A critical review of flood risk management and the selection of suitable measures. Appl Sci. 2020;10(23):8752. https://doi.org/10.3390/app10238752
17. Jain SK, Shilpa LS, Rani D, Sudheer KP. State-of-the-art review: Operation of multi-purpose reservoirs during flood season. J Hydrol. 2023; 618:129165. https://doi.org/10.1016/j.jhydrol.2023.129165
18. Mehta D, Achour B, Pastagia J, Azamathulla H, Verma S. Review of reservoir operation. LARHYSS J. 2023;(56):193-214.
19. Lu, M., & Merwade, V. Enhancing Reservoir Operations by Leveraging Large-Scale Data Sets for Multi-Objective Simulation and Optimization. J Water Resour Plan Manag. 2024. https://doi.org/10.1061/JWRMD5.WRENG-6778
20. Salmasi, F., Nouri, M., & Abraham, J. (2019). Laboratory study of the effect of sills on radial gate discharge coefficient. KSCE Journal of Civil Engineering, 23(5), 2117-2125. https://doi.org/10.1007/s12205-019-1114-y
21. Akbari, M., Salmasi, F., Arvanaghi, H., Karbasi, M., & Farsadizadeh, D. (2019). Application of Gaussian process regression model to predict discharge coefficient of Gated Piano Key Weir. Water Resources Management, 33(11), 3929-3947. https://doi.org/10.1007/s11269-019-02343-3
22. Salmasi, F., & Abraham, J. (2020). Expert system for determining discharge coefficients for inclined slide gates using genetic programming. Journal of Irrigation and Drainage Engineering, 146(12), 06020013. https://doi.org/10.1061/(ASCE)IR.1943-4774.0001520
23. Salmasi, F., & Abraham, J. (2021). Prediction of discharge coefficients for sluice gates equipped with different geometric sills under the gate using multiple non-linear regression (MNLR). Journal of Hydrology, 597, 125728. https://doi.org/10.1016/j.jhydrol.2020.125728

24. Salmasi, F., Nouri, M., Sihag, P., & Abraham, J. (2021). Application of SVM, ANN, GRNN, RF, GP and RT models for predicting discharge coefficients of oblique sluice gates using experimental data. Water Supply, 21(1), 232-248. https://doi.org/10.2166/ws.2020.226
25. Salmasi, F., Shadkani, S., Abraham, J., & Malekzadeh, F. (2022). Experimental investigation for determination of discharge coefficients for inclined slide gates and comparison with data-driven models. Iranian Journal of Science and Technology, Transactions of Civil Engineering, 46(3), 2495-2509. https://doi.org/10.1007/s40996-022-00850-9
26. Wurbs, R. A. (2005). Modeling river/reservoir system management, water allocation, and supply reliability. Journal of Hydrology, 300(1-4), 100-113. https://doi.org/10.1016/j.jhydrol.2004.06.003
27. Lund, J. R., & Guzman, J. (1999). Derived operating rules for reservoirs in series or in parallel. Journal of water resources planning and management, 125(3), 143-153. https://doi.org/10.1061/(ASCE)0733-9496(1999)125:3(143)
28. SMOKOROWSKI, K. E., et al. Ecosystem level assessment of environmentally based flow restrictions for maintaining ecosystem integrity: a comparison of a modified peaking versus unaltered river. Ecohydrology, 2011, 4.6: 791-806. https://doi.org/10.1002/eco.167
29. Yeh WWG. Reservoir management and operations models: A state-of-the-art review. Water Resour Res. 1985;21(12):1797-1818. https://doi.org/10.1029/WR021i012p01797
30. ASCE Task Committee. Guidelines for retirement of dams and hydroelectric facilities. American Society of Civil Engineers; 1999.



© 2026 by the authors. Licensee SCU, Ahvaz, Iran. This article is an open access article distributed under the terms and conditions of the Creative Commons Attribution 4.0 International (CC BY 4.0 license) (http://creativecommons.org/licenses/by/4.0/).

Risk Analysis of Internal Erosion in Earth Dams Considering Uncertainties in the Permeability Coefficient of Materials

Samane Manafi [1], Jafar Yazdi [*,1]

1. Department of Water Resources Engineering, Shahid Beheshti University, Tehran, Iran.

***Corresponding Author:**
Jafar Yazdi

Email: j_yazdi@sbu.ac.ir
Received: 2026.01.30
Accepted: 2026.06.27
J. Hydraul. Struct., 2026; 12(4):60-74
DOI: 10.22055/jhs.2026.51383.1371

ABSTRACT

Earth dams play a crucial role in water supply and power generation; therefore, ensuring their stability, safety and identifying various potential failure mechanisms are of great importance.
Among different failure modes, internal erosion (piping) is one of the primary factors contributing to the instability and eventual failure of earth dams. In this study, a probabilistic framework is proposed to assess the risk of internal erosion in earth dams considering uncertainty in the permeability coefficient of materials. The Lar Dam was selected as a case study. Seepage analysis was performed using the finite element method in SEEP/W software under transient conditions based on a 22-year time series of reservoir water levels. The uncertainty in permeability coefficients of dam materials was modeled using normal probability distributions. To quantify the risk of internal erosion, two point-estimate methods, namely Rosenblueth and Harr methods, were applied. The results showed that the probability of internal erosion is 0.22 and 0.21 using Rosenblueth and Harr methods, respectively, with a standard deviation of approximately 0.10. These results indicate a relatively high risk of internal erosion in Lar Dam. Furthermore, the close agreement between the two methods demonstrates that the Harr method can be used as a computationally efficient alternative for probabilistic risk assessment in cases with symmetric distributions. The proposed approach provides a practical framework for incorporating uncertainty into internal erosion risk analysis of earth dam.

KEYWORDS
internal erosion risk, earth dam, uncertainty, permeability coefficient, Harr method, Rosenblueth method.

1. Introduction

Dams, as one of the main engineering structures in water resource management and flood control, play a vital role and hold particular importance in providing drinking water, supporting agriculture, and generating hydroelectric power [1]. Any dam failure can lead to significant human and financial losses. The seriousness of dam failure stems from the severe risks it poses to human communities. Given the importance of dams—especially earth dams, which are more prevalent and widely used—examining and analyzing the factors that lead to their failure is critically important [2]. Because of the key role of earth dams in achieving multiple objectives, the stability of these structures is also of great significance. Earth dams are susceptible to various failure modes, such as overtopping, earthquakes, internal erosion, slope instability, and more. Among these, the risk stemming from internal erosion has been studied occasionally as a critical factor threatening the stability of earth dams. Some of these studies are as follows:

Delavar et al. (2016) investigated internal erosion and seepage in earth dams using the Natural Element Method (NEM) [3]. They first validated the accuracy of NEM by simulating the behavior of porous flow and calculating leakage discharge in a semi-permeable weir, and then applied the method to the Doroodzan Dam. Their results showed that the proposed method, with an average error below 5%, has suitable accuracy for analyzing this phenomenon. They also reported that the absence of internal erosion and piping in the dam body—due to the constancy of the permeability coefficient over time—confirms the proper performance of the body drain. Fattahi et al. (2020) conducted a case study to analyze seepage in the foundation and body of the Roudbar Lorestan earth dam using a numerical finite element method [4]. The results showed that the water seepage through the cross-section of the dam's foundation and body was equivalent to 0.27% of the dam's total water volume. Moreover, the dam demonstrated a very high safety factor against piping. Kalate and Kheiri (2022), taking into account uncertainty in hydraulic conductivity, examined seepage in earth dams using the finite element method and Monte Carlo simulation (MCS) [5]. To predict the Effective Seepage Discharge (ESD), they employed Support Vector Regression (SVR) and Gene Expression Programming (GEP). With a correlation coefficient of 0.96 and a root mean square error of approximately 0.01, the SVR model exhibited higher accuracy than GEP and showed closer agreement with the finite element analysis. Koohdaraq et al. (2024) used SEEP/W software to study seepage flow and hydraulic gradient in the body and foundation of the Alavian earth dam [6]. The purpose of their research was to analyze the effects of seepage flow and hydraulic gradient, as well as to evaluate various seepage control methods such as drains, cutoff walls, and clay blankets. Foster et al. (2000) presented a method for estimating the relative probability of earth dam failures due to piping, based on an analysis of historical dam failures and incidents [7]. They approximated a dam's probability of failure from piping by using weighted factors. Data on the time interval of piping and its warning signs indicate that piping usually develops rapidly, providing little time for remedial measures. However, in certain cases, the piping process progresses slowly enough to allow sufficient time for reservoir drawdown or other corrective actions to prevent further infiltration.

Zhang et al. (2006) investigated the failure of the Guohui Dam in China, examining the geometric and hydraulic criteria for internal erosion in gravelly materials [8]. They employed unsaturated-saturated seepage theory to analyze Guohui Dam, as the gravelly materials were unsaturated prior to reservoir water penetration. Water infiltration was simulated through several scenarios, and the results indicated that once reservoir water entered the gravelly materials, a perched water table formed and moved horizontally within the gravel layers, exiting through the downstream slope. The hydraulic gradient of this perched water was greatest near the saturated zone, creating conditions conducive to internal erosion and piping failure. This study demonstrated that the dam's geometric and hydraulic conditions can significantly influence the occurrence of internal erosion and dam failure. Athani et al. (2015) analyzed seepage and stability results for an earth dam using the finite element method [9]. They concluded that increasing the Young's modulus of the core and shell reduces the maximum settlement of the dam crest, while changes in the internal friction angle are crucial in meeting stability criteria. Sazzad et al. (2015) examined seepage through earth dam bodies from a structural safety perspective [10]. They used numerical and analytical analyses to evaluate the effects of factors such as the shape and size of the mesh, the shape of the internal clay core, and the upstream and downstream slopes, as well as

foundation permeability, on seepage rates. Various geometric models of dams were developed, and the discharge rate was analyzed for each model. The findings showed that mesh shape and size have a negligible effect on seepage. When a clay core is present, neither the upstream nor the downstream slope affects seepage. Moreover, without a clay core, seepage is independent of foundation permeability; however, in the presence of a clay core, foundation type (permeable or impermeable) impacts seepage when hydraulic conductivity is high. Tan et al. (2017) used Monte Carlo simulation and random field theory to examine the impact of spatial variations in hydraulic parameters on seepage in earth dams [11]. They applied the van Genuchten model for the soil-water characteristic curve (SWCC) and treated the soil characteristic curve parameters α, n, and the saturated hydraulic conductivity (k_s) as random variables with a lognormal distribution. Results revealed that the coefficient of variation (COV) for n and k_s exerts a stronger influence on seepage rates, whereas the COV for α is less significant. Furthermore, increasing the horizontal correlation length leads to higher mean seepage rates and greater variability. This study showed that disregarding the spatial variation of hydraulic parameters can lead to conservative estimates in earth dam design. Wang et al. (2023) investigated piping failure in tailings dams [12]. They examined the effect of fine particles on the piping process by combining permeability tests and a discrete particle flow model. The results showed that increasing the number of fine particles reduces the permeability coefficient and raises the critical water height. Additionally, changes in pore ratio and particle size distribution were significantly affected by fine particles. From a meso-structural standpoint, this study also offered new approaches to preventing piping and water infiltration failures in tailings dams. Liu et al. (2024) explored internal erosion failures in sliding dams with highly permeable regions [13]. They employed physical models to analyze how the position and particle size distribution of these zones affect water seepage. The results indicated that piping and downstream slope erosion are among the most critical failure modes for this type of dam. Moreover, increasing the permeability coefficient intensifies the speed and severity of piping, slope erosion, and dam collapse.

A review of previous research reveals that there have been relatively few studies on estimating the risk of internal erosion. The limited existing research primarily adopts a deterministic approach and focuses on estimating seepage flow. The main novelty of this study lies in the integration of transient seepage analysis with probabilistic internal erosion assessment, enabling a more realistic evaluation of erosion risk in earth dams under uncertain hydraulic conditions. In addition, this work applies and compares the Rosenblueth and Harr point-estimate methods to examine their capability in estimating the probability of internal erosion. A further contribution is the development of an efficient computational framework for internal erosion risk analysis in earth dams, explicitly accounting for the uncertainty associated with permeability.

2. Materials and Methods

2.1. Seepage Analysis in the Dam Body and Foundation

Generally, the total seepage discharge through a dam is divided into two components: seepage through the foundation and seepage through the dam body. In other words:

Total Seepage = Seepage Through Foundation + Seepage Through Body

In this study, the finite element method (FEM) using SEEP/W software was applied to calculate the seepage flow from the dam body and foundation. Seepage in earth dams can be analyzed under two conditions: steady-state and transient. Steady-state

conditions occur when neither the seepage discharge nor the water head at any point changes over time, which typically happens a few years after the dam reservoir is filled. In a water-saturated soil medium, the governing equation for steady-state (i.e., time-invariant) seepage flow is the Laplace equation, expressed as:

$$k_x \frac{\partial^2 h}{\partial x^2} + k_y \frac{\partial^2 h}{\partial y^2} = 0 \quad (1)$$

Where h is the water head, dependent on the spatial coordinates x and y. The terms k_x and k_y represent the permeability coefficients of the soil in the horizontal and vertical directions, respectively. By contrast, transient (unsteady) flow occurs when the water head at each point changes over time. For instance, once an earth dam is completely filled, the water head in its core rises until it reaches the free water surface [14].

It should be noted that as the reservoir level changes due to filling or drawdown, the water level in the dam's core also fluctuates. In high dams, such transient flow conditions may warrant further analysis. Under transient conditions, the governing equation (the Boussinesq equation) is:

$$k_x \frac{\partial^2 h}{\partial x^2} + k_y \frac{\partial^2 h}{\partial y^2} = c \frac{\partial h}{\partial t} \quad (2)$$

Here, $\frac{\partial h}{\partial t}$ indicates that the water head changes over time, thereby signifying unsteady flow. Various approaches exist for solving the Boussinesq equation; however, with advances in computing technology over the past three decades, numerical analyses using specialized software have largely replaced analytical methods.

2.2. Uncertainty Analysis Using the Rosenblueth Point Estimate Method

The Rosenblueth Point Estimate Method is a commonly used approach in uncertainty analysis and risk assessment for estimating statistical parameters of complex functions. In this method, the probability distribution of random variables is approximated by a limited number of representative points (often two points for each variable). By combining these points, an estimate of the target expected values (such as mean and variance) is obtained. The primary advantage of this method lies in its significant reduction in computational cost compared to Monte Carlo simulations or Latin Hypercube Sampling (LHS), while still maintaining adequate accuracy in assessing the impact of uncertainties [15]. The permeability coefficients of the materials used in the dam inherently carry uncertainty. To consider this uncertainty in the piping risk analysis, it is necessary to run a transient (non-steady-state) model of water seepage through the dam and foundation. Since this model is very time-consuming to run, using a Monte Carlo simulation for analyzing uncertainty in soil permeability coefficients was not feasible. Consequently, the Rosenblueth Point Estimate Method and the Harr Point Estimate Method—both of which entail far fewer computations—were employed for this purpose. This section provides a detailed explanation of the Rosenblueth method.

Considering a model $W = g(X)$, which has a random variable X and its three initial moments or probability density function (PDF) are known, the Rosenbluth probability point method estimates the original probability density function of the random variable X by assuming that the entire probability mass of X is concentrated in two points x_- and x_+ .

Using the two-point estimation, the positions x_- and x_+ and their corresponding probability masses p_- and p_+ are determined in such a way that the first three moments of the random variable X are preserved. In the general case where a model has N dependent random variables, the m^{th} moment of the model $W = g(X_1, X_2, \dots, X_N)$ around the origin can be estimated as follows:

$$E(W^m) \approx \sum p_{(\delta_1,\delta_2,\ldots,\delta_N)}\left[w_{(\delta_1,\delta_2,\ldots,\delta_N)}\right]^m \quad (3)$$

where the index δ_i indicates the sign and can only be + or – and indicates that the random variable X_i has the value $x_{i+} = \mu_i + x'_{i+}\sigma_i$ or $x_{i-} = \mu_i + x'_{i-}\sigma_i$. The probability mass at each 2^N point, $p_{(\delta_1,\delta_2,\ldots,\delta_N)}$, can be estimated as follows:

$$p_{(\delta_1,\delta_2,\ldots,\delta_N)} = \prod_{i=1}^{N} p_i\sigma_i + \sum_{i=1}^{N-1}\left(\sum_{j=i+1}^{N}\delta_i\delta_j a_{ij}\right) \quad (4)$$

$$a_{ij} = \frac{\rho_{ij}/2^N}{\sqrt{\prod_{i=1}^{N}\left[1+\left(\gamma_i/2\right)^2\right]}} \quad (5)$$

3.2. Uncertainty Analysis Using the Harr Point Estimate Method

The Harr Point Estimate Method is an approximate technique for uncertainty assessment in which a limited number of specific points in the space of random variables are used to estimate the statistical behavior of a system. Rather than performing extensive sampling (such as Monte Carlo simulations), this method selects particular points in the probabilistic space that represent the mean and variance of the random variables. The response function is then evaluated at these points, and the resulting values are combined to estimate statistical parameters of complex functions. Because only a small number of points are required and the computational demands are relatively low, the Harr method is especially effective and efficient in applications involving computationally intensive numerical models (such as finite element models) [16].

For a multivariate model $W = g(X_1, X_2, \ldots, X_N)$ with N random variables, the Haar method selects the calculation points at the intersection of the axes of the N eigenvectors with the plane of a multidimensional sphere of radius $\sqrt{N}$ in the eigenspace as follows:

$$x_i = \mu \pm \sqrt{ND^{1/2}}\vartheta_i \ , \quad i = 1.2.\ldots,,.N \quad (6)$$

Where $x_{i\pm}$ represents the coordinate vector of N random variables in the parameter space corresponding to the i[th] eigenvector, ϑ_i and $\mu = (\mu_1, \mu_2, \ldots, \mu_N)^t$ is the vector of means of N random variables X. Based on the 2N points determined by equation (6), the function values at each 2N point can be calculated. Therefore, the m[th] output moment of the model W about the origin can be calculated based on the following equations:

$$\overline{w_i^m} = \frac{w_{i+}^m + w_{i-}^m}{2} = \frac{g^m(x_{i+}) + g^m(x_{i-})}{2}, \quad i = 1,2,\ldots..,N\ ;\ m = 1,2,\ldots \quad (7)$$

$$E[W^m] = \mu_m(W) = \frac{\sum_{i=1}^{N}\lambda_i\overline{w_i^m}}{\sum_{i=1}^{N}\lambda_i} \ , \quad m = 1.2.\ldots \quad (8)$$

2.4. Risk Analysis of Internal Erosion

Exceeding the critical hydraulic gradient triggers internal erosion. Piping is one of the most significant mechanisms of hydraulic failure in earth dams and happens when the hydraulic gradient (i) surpasses its critical value (i_{cr}). This phenomenon leads to internal erosion and ultimately creates preferential flow paths within the dam body or foundation. In this study, numerical and probabilistic methods were used to analyze this phenomenon. To evaluate the dam's stability against internal erosion (piping), the hydraulic gradient must first be calculated, which is defined as follows:

$$i = \frac{\Delta h}{L} \quad (9)$$

where Δh denotes the head difference and L is the length of the flow path through the soil. The seepage path length is estimated using Equation (10), which is presented as follows:

$$L = \sqrt{\Delta h^2 + \Delta x^2} \quad (10)$$

where Δh is the change in piezometric head between two points (in meters) and Δx is the horizontal distance between those two points (in meters). Therefore, the probability of internal erosion is given by:

$$R = P(i > i_{cr}) \quad (11)$$

Since the hydraulic gradient i depends on the soil permeability K, and K itself carries uncertainty, this uncertainty propagates to the risk of internal erosion. Given the uncertainty in K, the hydraulic gradient i is assumed to follow a normal distribution. Similarly, based on the minimum and maximum critical gradient values from reputable geotechnical references, the critical gradient i_{cr} is also assumed to follow a normal distribution. Thus, for the probability that $i \geq i_{cr}$ one can write:

$$P(i > i_{cr}) = P(i - i_{cr} > 0) \quad (12)$$

Since i and i_{cr} are both normally distributed, their difference $(i - i_{cr})$ is also normally distributed. Therefore, the variable Z is standard normally distributed:

$$Z = \frac{(i - i_{cr}) - \mu_{i-i_{cr}}}{\sigma_{i-i_{cr}}} \quad (13)$$

where $\mu_{i-i_{cr}}$ is the mean of $(\mu_{i-i_{cr}})$ and $\sigma_{i-i_{cr}}$ is the standard deviation of the normally distributed variable $(i - i_{cr})$. According to the standard normal distribution:

$$\mu_{i-i_{cr}} = \mu_i - \mu_{i_{cr}} \quad (14)$$

$$\sigma_{i-i_{cr}} = \sqrt{\sigma_i^2 + \sigma_{i_{cr}}^2} \quad (15)$$

Therefore:

$$P(i > i_{cr}) = \Phi\left(\frac{\mu_{i-i_{cr}}}{\sigma_{i-i_{cr}}}\right) \quad (16)$$

Where $\Phi\left(\frac{\mu_{i-i_{cr}}}{\sigma_{i-i_{cr}}}\right)$ is the cumulative distribution function (CDF) of the standard normal distribution, whose values can be obtained from standard normal distribution tables.

2.4. Case Study

Lar Dam is one of the major dams in Iran, located on the southern slopes of Mount Damavand (Figure 1), approximately 84 kilometers northeast of Tehran. This earth dam, with a clay core, has been under construction since the 1971s to supply drinking water to Tehran and control seasonal floods, and it was commissioned in the 1981s. Lar Dam has a considerable reservoir capacity, meeting part of Tehran's drinking water needs and providing the potential for hydropower generation. However, reports indicate seepage issues in the dam body and foundation, which could be related to internal erosion [17], [18]. Thus, assessing the risk of internal erosion in Lar Dam is particularly critical given its strategic importance for water resource management in metropolitan Tehran. Lar Dam is an earth-fill dam with a height of 105 meters from the riverbed and a crest length of 1,300 meters. Table 1 presents the permeability characteristics of Lar Dam, and Figure 2 illustrates the zones of materials used in the dam body and foundation.

Table 1. Permeability Coefficients of Materials Used in Lar Dam (Moshanir Company, 2022)

Zone	Material Type	Average Permeability (m/day)	Average Permeability (cm/s)	Minimum Permeability (m/day)	Minimum Permeability (cm/s)	Maximum Permeability (m/day)	Maximum Permeability (cm/s)
1A, 1B	Silty Clay	0.0006912	7.966×10^{-7}	0.0005184	5.998×10^{-7}	0.000864	1×10^{-6}
2	Sandy Silt	0.001728	1.999×10^{-6}	0.000864	1×10^{-6}	0.002592	3×10^{-6}
3A, 3B, 3C, 4, 5	Sandy Gravel	475.2	0.5498	86.4	0.1	864	1
Foundation	Silty Clay	0.0004752	5.498×10^{-7}	0.0000864	1×10^{-7}	0.000864	1×10^{-6}

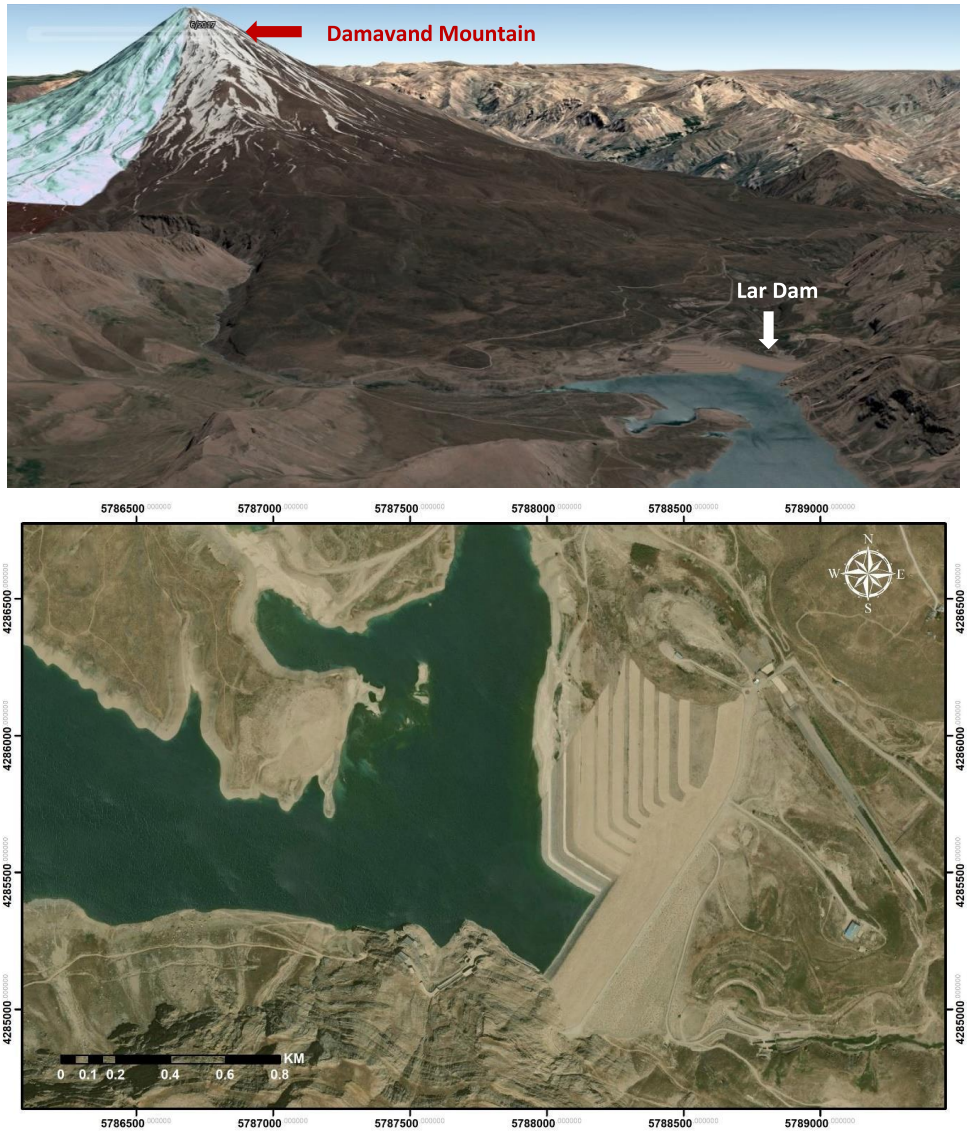


Figure 1. (a) The location of Lar Dam relative to Mount Damavand; (b) Layout of Lar Dam

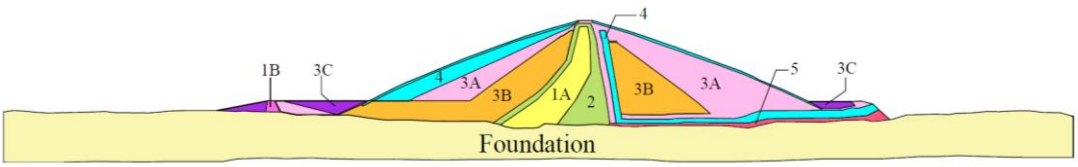


Figure 2. Zones of Materials Used in Lar Dam (Moshaniro Company, 2023).

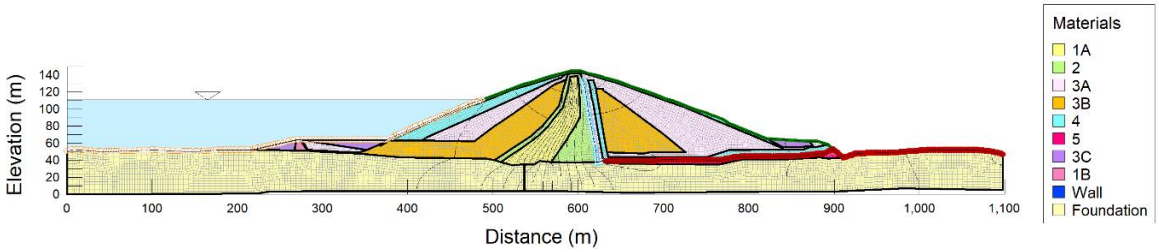


Figure 3. Finite Element Mesh and Materials Used in Lar Dam.

3. Model Implementation and Results Analysis

In this study, the SEEP/W software was used to numerically solve the seepage equations using the finite element method. In the finite element approach, both triangular and quadrilateral elements were employed to construct the computational mesh. A sensitivity analysis was conducted on the mesh dimensions, and ultimately a mesh element size of 3 meters was adopted. Figure 3 shows the computational mesh of the dam body and foundation, along with its zoning. It is worth noting that the longitudinal profile shown corresponds to Chainage 320 on the right bank of Lar Dam.

For the seepage analysis in this software, after constructing the geometry of Lar Dam and assigning its permeability coefficients equal to their average values—based on the type of materials used and the data received from the Tehran Regional Water Company (Table 1)—the model was executed under both steady-state and unsteady-state conditions.

Under steady-state conditions, when the reservoir water level was at its historical maximum, the seepage discharge in the critical zone of the core was estimated to be 0.12 m^3/day, and when the reservoir water level was at its historical minimum, it was estimated to be 0.036 m^3/day.

The boundary conditions applied in the steady-state analysis were as follows:

- Upstream boundary: Head (m)
- Filter boundary: Total Flux (m^3/day)
- Downstream boundary: Pressure Head (m)

For the upstream boundary, the water head was set equal to the maximum inflow head into the dam. The Total Flux and Pressure Head at the filter and downstream boundaries were set to zero. The numerical results of the steady-state seepage analysis are presented in Figure 4(a).

The boundary conditions for the unsteady-state analysis were similar to those of the steady-state, with the exception that in the unsteady-state case, the upstream boundary condition is defined as a time-dependent Head (m) function due to variations in the reservoir water level over time. In the Lar Dam model, this function was defined based on daily water level data collected over the period from 2001 to 2023 (corresponding to 8159 days). The results of the seepage analysis over these 8159 days are shown in Figure 4(b).

As Figure 4(b) illustrates, the highest hydraulic gradient occurs in the core zone of the dam. Therefore, in the calculation of the internal erosion risk, the hydraulic gradient in the dam core was used, since the other zones or transition areas exhibit more favorable hydraulic gradient conditions compared to the core.

Validation of the Seepage Model for the Dam Body and Foundation

After running the model, the piezometric head outputs were obtained. To validate the model, the observed data for the only available piezometric head measurement at location H38 (shown in Figure 5) was received from the Tehran Regional Water Company, and the model results were compared with these measured values. It is noteworthy that the model results were obtained using the average permeability coefficients. Figure 6 presents a comparison between the modeled and measured results. As observed visually, the model has successfully predicted both the temporal variations and the magnitude of the piezometric head. It should also be mentioned that although additional piezometers have been installed in the dam body, data from these devices were unfortunately not available, which limited further evaluation of the model's performance.

Analysis of the Probability of Failure Due to Internal Erosion

The execution time for the transient analysis on a system with a Core™ i5-12450H processor and 16 GB of memory was around 2.5 hours. This duration is considerable and limits the use of random sampling methods such as the Monte Carlo method and Latin Hypercube Sampling. Therefore, in this study, two-point estimate methods—the Rosenblueth Point Estimate Method and the Harr Point Estimate Method—were utilized.

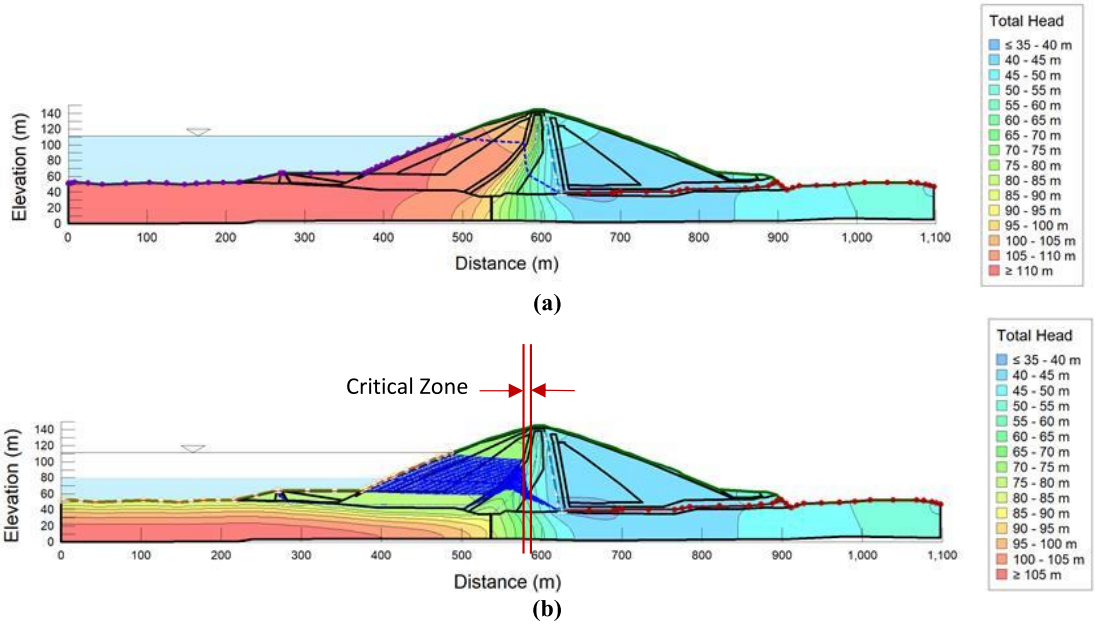


Figure 4. Leakage from the Lar Dam Body in Case (a) Steady Analysis and (b) Unsteady Analysis.

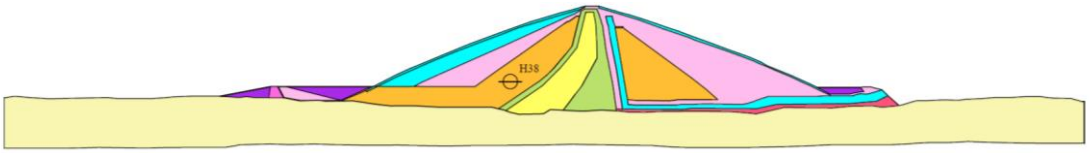


Figure 5. Location of Piezometer H38 on the Dam Body.

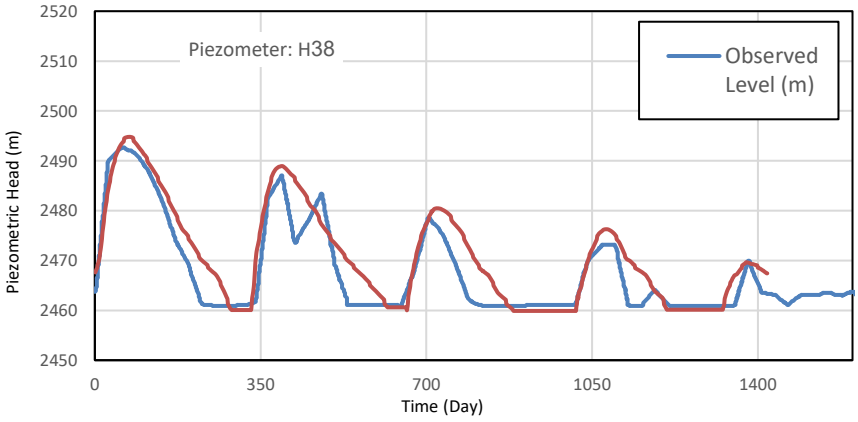


Figure 6. Changes in Piezometric Head from 2019 to 2023.

Rosenblueth Point Estimate Method

Considering that the dam body and foundation of Lar Dam consist of four different types of materials, and that the permeability coefficients of these materials inherently possess uncertainty, the uncertainty of the permeability coefficient for each material was modeled using a normal distribution. The mean of each distribution was taken as the average value reported in Table 1, and the standard deviation of the probability distribution was estimated as $\sigma \approx \frac{K_{max} - K_{min}}{6}$ based on the theoretical principles of probability and statistics. This choice is justified by the fact that, for a normal distribution, approximately 97.5% of the data lie within ±3σ. According to the theory of the Rosenblueth Point Estimate Method, if the probability of internal erosion is represented by a function $g(k)$ and the permeability coefficient k is treated as the uncertain input parameter, then for Lar Dam there are N=4 random input variables corresponding to the permeability coefficients. Consequently, according to the Rosenblueth method, $2^4 = 16$ possible points must be evaluated. Assuming a normal probability mass function (PMF) for the permeability variable, the PMF for the random variable K is approximated at two points, K_- and K_+. Since the probability distribution of the random variable K is symmetric (i.e., normally distributed), the skewness factor is γ=0. In this case, according to the relations in the Rosenblueth method, we have: $k'_- = k'_+ = 1$ and $p_- = p_+ = 0.5$. If the permeability coefficients for the core, transitional zone, shell, and foundation are denoted by K_1, K_2, K_3 and K_4 respectively, the objective is to calculate the probability of internal erosion in the critical zone of the core. Now, it is necessary to evaluate the function $g(k)$, which represents the probability of internal erosion (Pp), at the 16 computational points (i.e., $2^4 = 16$) as determined by the Rosenblueth method, as listed in Table 2. Subsequently, based on these probability values, the expected value of the internal erosion probability (μ = E(P_p)) and its standard deviation (σ_{P_p}) were calculated. The values for the probability of internal erosion occurrence at these points are provided in Table 3.

According to the formulas, assuming that the permeability coefficients are independent, the probability mass (P) is obtained as 0.625. Then, by calculating $P_p \times P$ and $(P_p^2) \times P$ and summing the resulting values, we obtain μ_{P_p}= E(P_p) = 0.225 and E(P_p^2) = 0.066. Therefore, the expected value of the "internal erosion probability" and its standard deviation, as determined by the Rosenbluth method, are 0.225 and 0.1, respectively.

Table 2. Permeability Coefficients Calculated Using the Rosenbluth Method Formulas.

Point	K_1 (m/day)	K_2 (m/day)	K_3 (m/day)	K_4 (m/day)
1	0.00072	0.00216	540	0.00054
2	0.00072	0.00216	410.4	0.0004104
3	0.00072	0.00216	540	0.0004104
4	0.00072	0.00216	410.4	0.00054
5	0.00072	0.001296	540	0.0004104
6	0.00072	0.001296	410.4	0.00054
7	0.00072	0.001296	540	0.00054
8	0.00072	0.001296	410.4	0.0004104
9	0.0006624	0.00216	540	0.00054
10	0.0006624	0.00216	410.4	0.0004104
11	0.0006624	0.00216	540	0.0004104
12	0.0006624	0.00216	410.4	0.00054
13	0.0006624	0.001296	540	0.0004104
14	0.0006624	0.001296	410.4	0.00054
15	0.0006624	0.001296	540	0.00054
16	0.0006624	0.001296	410.4	0.0004104

Table 3. Probability of Internal Erosion Occurrence at Estimation Points Using the Rosenbluth Method.

Point	K_1 (m/day)	K_2 (m/day)	K_3 (m/day)	K_4 (m/day)	Probability of Internal Erosion Occurrence (P_p)
1	+	+	+	+	0.114
2	+	+	-	-	0.115
3	+	+	+	-	0.115
4	+	+	-	+	0.108
5	+	-	+	-	0.396
6	+	-	-	+	0.357
7	+	-	+	+	0.357
8	+	-	-	-	0.369
9	-	+	+	+	0.084
10	-	+	-	-	0.086
11	-	+	+	-	0.09
12	-	+	-	+	0.09
13	-	-	+	-	0.342
14	-	-	-	+	0.323
15	-	-	+	+	0.335
16	-	-	-	-	0.342

Harr's Point Estimation Method

Considering four different types of materials for the Lar dam, and based on Harr's probability point estimation theory, if the permeability coefficient of the materials is assumed to be a non-deterministic parameter, there are N = 4 random variables. According to Harr's method, a total of 2×N = 8 possible points must be examined. The points evaluated using Harr's method, calculated according to the existing formulas, are presented in Table 4. Additionally, the values for the probability of internal erosion occurrence at these points are provided in Table 5.

Table 4. Permeability Coefficients Calculated at the Evaluation Points Using Harr's Method.

Point	K_1 (m/day)	K_2 (m/day)	K_3 (m/day)	K_4 (m/day)
+1	0.0007488	0.0017	475.2	0.0004752
-1	0.000633	0.0017	475.2	0.0004752
+2	0.0006912	0.0026	475.2	0.0004752
-2	0.0006912	0.000864	475.2	0.0004752
+3	0.0006912	0.0017	604.8	0.0004752
-3	0.0006912	0.0017	345.6	0.0004752
+4	0.0006912	0.0017	475.2	0.0006048
-4	0.0006912	0.0017	475.2	0.0003456

Table 5. Calculation of the Internal Erosion Occurrence Probability at the Evaluation Points Using Harr's Method.

Point	Probability of Internal Erosion (P_p)	$(P_p)^2$	$\overline{P_p}$	$\overline{P_p^2}$
+1	0.258	0.066	0.156	0.034
-1	0.055	0.003		
+2	0.204	0.041	0.202	0.041
-2	0.2	0.04		
+3	0.173	0.03	0.275	0.086
-3	0.377	0.142		
+4	0.204	0.041	0.206	0.042
-4	0.207	0.043		

According to the formulas in Harr's method, the mean value is μ_{P_p} = 0.21 and $E(P_p^2)$ = 0.05. Therefore, the expected value of "internal erosion occurrence" and its standard deviation using Harr's method are 0.21 and 0.08, respectively, which are values close to those obtained from the Rosenbluth probability point method.

The probabilistic analyses performed using the Rosenblueth and Harr point-estimation methods yielded closely comparable results, indicating a mean internal erosion probability of approximately 0.225 and 0.21, respectively, with standard deviations of about 0.10 and 0.08. This close agreement is important because it suggests that the estimated erosion risk is not strongly dependent on the specific point-estimation scheme adopted, despite the different sampling strategies of the two methods. The Rosenblueth method evaluates 2^N=16 combinations for the four uncertain permeability variables, whereas Harr's method requires only 2N=8 evaluations. Therefore, the similarity of the results implies that Harr's method can provide a computationally efficient approximation of internal erosion risk for practical engineering applications, while the Rosenblueth method offers a somewhat richer exploration of the uncertainty space. From an engineering perspective, the fact that both methods produce a moderate probability of internal erosion, on the order of 0.21 to 0.23, indicates that the risk cannot be considered negligible and should be explicitly accounted for in seepage safety assessments of the dam.

A closer examination of the Rosenblueth evaluation points shows that the predicted probability of internal erosion varies noticeably across different combinations of permeability values. In particular, the lowest probabilities are associated with cases in which the permeability of the transition zone is relatively high, whereas markedly larger probabilities are observed when the transition-zone permeability takes its lower value. This pattern suggests that the transition zone plays a critical role in controlling the hydraulic response of the dam and, consequently, the susceptibility of the core to internal erosion. Physically, a reduction in the permeability of the transition zone may hinder the proper dissipation or redistribution of seepage flow, thereby increasing unfavorable hydraulic gradients in the critical part of the core. By contrast, variations in other material zones also affect the results, but their influence appears to be less dominant than that of the transition zone. This observation is valuable because it identifies a parameter to which the predicted erosion response is particularly sensitive, and it can help prioritize site investigation, material characterization, and quality control during design or rehabilitation.

The dispersion of the estimated probabilities, reflected by standard deviations in the range of 0.08 to 0.1, also deserves attention. These values show that uncertainty in permeability does not merely shift the mean estimate, but also creates a relatively broad spread in possible erosion outcomes. In other words, even if the mean

probability is moderate, there are combinations of material properties for which the likelihood of internal erosion becomes substantially higher. This finding highlights the importance of incorporating parameter uncertainty into seepage and erosion assessments, rather than relying solely on deterministic permeability values. It also supports the use of probabilistic frameworks in dam safety evaluation, because such approaches are able to capture both the expected level of risk and its variability. Overall, the results demonstrate that uncertainty in hydraulic properties, especially permeability, has a meaningful impact on the predicted internal erosion potential and should therefore be considered an integral part of risk-informed assessment for earth dams.

4. Conclusion

In this study, the risk of internal erosion for the Lar dam was calculated using the Rosenbluth and Har uncertainty analysis methods, considering the uncertainty in the permeability coefficients of the materials. The main findings are summarized as follows:

1. The results obtained from both Rosenblueth and Harr point estimate methods indicated that the probability of internal erosion is 0.22 and 0.21, respectively, suggesting a relatively high-risk level for the dam. This result is consistent with recent studies by consulting engineers regarding the safety of this dam.
2. The calculated probabilities of internal erosion occurrence from both the Rosenbluth and Harr methods are very similar, and their standard deviations are nearly equal, confirming the accuracy of the computations.
3. The findings also highlight that uncertainty in permeability coefficients plays a significant role in the variability of hydraulic gradients and, consequently, in the initiation of internal erosion. Higher permeability values, especially in coarse-grained materials, can lead to increased hydraulic gradients, thereby increasing the possibility of internal erosion. This emphasizes the importance of accurately characterizing material properties in dam safety assessments.
4. The standard deviation values obtained by both methods are approximately 0.10, which reflects the range of variability in the internal erosion probability.
5. In the present study, the computational burden of the Rosenbluth method is twice that of the Harr method, even though both methods produced identical results. Generally, the computational effort for the Rosenbluth method is 2N and for the Harr probability point method is also 2N. However, despite the lower computational load of the Harr method, it is only applicable to symmetric probability distributions. If the probability distribution of the variables is asymmetric, the asymmetry is not considered in the Harr method, whereas the Rosenbluth method accounts for the skewness of the random variables in the risk analysis. In this study, the use of a normal probability distribution, which has central symmetry, resulted in identical outcomes for both methods.
6. The close agreement between the results of the two methods demonstrates the reliability of point-estimate techniques in probabilistic risk assessment. In particular, the Harr method, due to its lower computational cost, can be considered an efficient alternative to the Rosenblueth method

in cases where input variables follow symmetric distributions.

For future research on this topic, the following recommendations are proposed:

1- Investigate the risk of internal erosion using the Monte Carlo method by incorporating the uncertainty in the critical hydraulic gradient.
2- Consider the uncertainty of other parameters, such as the specific weight of the materials, in the stability analysis.
3- Conduct a stability analysis of the Lar dam that accounts for seismic dynamic loads and incorporates the uncertainty of the dam's behavioral model parameters.
4- Evaluate the risk of liquefaction for earth dams.

Funding: The authors declare that no funds, grants, or other support were received during the preparation of this manuscript.

Data Availability: Not applicable.

Declarations

Competing Interests: The authors declare that they have no known competing financial interests or personal relationships that could have appeared to influence the work reported in this paper.
Ethical Approval: Not applicable.
Consent to Participate: Not applicable.
Consent to Publication: The authors give their full consent for the publication of this manuscript

References

1. Smith BR, Edds DR, Goeckler JM. Low head dams and the downstream dispersal of zebra mussels. Hydrobiologia. 2015;755:1-12.
2. Aghamajidi R. Examination of the dam failure process and its associated hazards in the event of occurrence (A case study of Dorudzan Dam). Technical Strategies in Water Systems. 2024; 2 (2): 174-185. Available from: https://civilica.com/doc/2146756
3. Delavar E, Zounemat Kermani M, Baradaran G. Seepage simulation through the body of earth dam using natural element meshless numerical method: Case study: Droodzan Dam. Journal of Dam and Hydroelectric PowerPlants. 2016; 3(8): 45-55 (In Persian).
4. Fattahi H, Shahmansouri M, Ghaedi H. Analysis of leakage in the foundation and body of an earth dam using numerical modeling: A case study. J Iranian Eng Geology Assoc. 2020;14(1):43-56. (In Persian).
5. Kalateh F, Khairi M. Uncertainty analysis in the simulation of effective leakage flow rate in earth dams using the Monte Carlo algorithm and machine learning. Model Manag Water Soil. 2022;4(1):151-170. (In Persian).
6. Kohdaragh M, Majidi Asl M, Omidpour Alavian T, Noubahari N, Ayami L. Analysis of leakage flow and hydraulic gradient in the body and foundation of the Alavian Earth Dam. Water Soil Sci (Isfahan Univ Technol). 2024;28(4):177-192. (In Persian).
7. Foster M, Fell R, Spannagle M. A method for assessing the relative likelihood of failure of embankment dams by piping. Can Geotech J. 2000;37(5):1025-1061.
8. Zhang LM, Chen Q. Seepage failure mechanism of the Gouhou rockfill dam during reservoir water infiltration. Soils Found. 2006;46(5):557-568.
9. Athani SS, Solanki CH, Dodagoudar GR. Seepage and stability analyses of earth dam using finite element method. Aquatic Procedia. 2015;4:876-883.
10. Sazzad MM, Roy MRINM, Rahman MM. FEM based seepage analysis through earth dam. Int J Adv Struct Geotech Eng. 2015;4(3):158-164.
11. Tan X, Wang X, Khoshnevisan S, Hou X, Zha F. Seepage analysis of earth dams

considering spatial variability of hydraulic parameters. Eng Geol. 2017;228:260-269.
12. Wang G, Zhao B, Zhao K, Wu B, Zhong W, Liu W. Piping-seepage mechanism of tailings with different fine particle contents. Int J Geomech. 2023;23(11):04023201.
13. Liu Z, Chen Q, Chen C, Li X, Zhao C. Experimental investigation on the characteristics of seepage failure of landslide dams with strongly permeable zones. IOP Conf Ser Earth Environ Sci. 2024;1334(1):012022.
14. Ghanbari A. *Principles of earth dam engineering*. Tehran: Khwarazmi University Press; 2014. (In Persian).
15. Rosenblueth E. Point estimates for probability moments. Proc Natl Acad Sci U S A. 1975;72(10):3812-3814. doi:10.1073/pnas.72.10.3812
16. Harr ME. Probabilistic estimates for multivariate analyses. Appl Math Model. 1989;13(5):313-318. doi:10.1016/0307-904X(89)90143-7
17. Moshanir Company. Preliminary report on the stabilization studies of the Lar Dam body. Tehran; 2022. (In Persian).
18. Ghadimi M. Conducting displacement studies of the Lar Dam body using the radar interferometry (InSAR) method and comparing them with the results of micro-geodetic operations [dissertation]. Tehran: University of Tehran; 2020. (In Persian).

© 2026 by the authors. Licensee SCU, Ahvaz, Iran. This article is an open access article distributed under the terms and conditions of the Creative Commons Attribution 4.0 International (CC BY 4.0 license) (http://creativecommons.org/licenses/by/4.0/).

Experimental Investigation of Local Scour Around Twin Cylindrical Bridge Piers: Effects of Pier Spacing and Skew Angle

AmirHossein Topal [1], Morteza Shokri [*,1], Majid Fazli [1]

1. Department of Civil Engineering, Faculty of Engineering, Bu-Ali Sina University, Hamedan, Iran.

***Corresponding Author:**
Morteza Shokri

Email: M.Shokri@basu.ac.ir
Received: 2026.04.26
Accepted: 2026.07.06
J. Hydraul. Struct., 2026; 12(4):75-90
DOI: 10.22055/jhs.2026.51968.1382

ABSTRACT

Local scour around bridge piers is a major cause of bridge instability in alluvial rivers, particularly when the approaching flow is skewed relative to the bridge alignment. This experimental study investigates the effects of pier spacing and skew angle on local scour development around twin cylindrical bridge piers. A total of 42 experiments were performed in a laboratory flume (15 m long, 0.6 m wide, and 0.6 m deep) under clear-water conditions. The sediment bed consisted of uniform sand with a median grain size of d_{50} = 1.6 mm. The flow discharge was maintained at 28 L/s with a water depth of 13.5 cm, corresponding to a Froude number of approximately 0.29. Two cylindrical piers with a diameter of D = 4 cm were tested at spacing ratios of S/D = 1–6 and skew angles ranging from 0° to 90°. The results show that the scour response strongly depends on both pier spacing and flow skewness. At close spacings (S/D = 1 and 2), increasing the skew angle intensifies the maximum scour depth and enlarges the scour-hole dimensions around both piers. At intermediate spacings (S/D = 3 and 4), the upstream pier experiences an increase in scour depth and scour length, while scour width decreases; in contrast, the downstream pier shows a non-monotonic variation, with scour parameters initially increasing and then decreasing. At wider spacings (S/D = 5 and 6), the upstream scour parameters continue to increase with skew angle, whereas the downstream maximum scour depth exhibits a rising–falling trend. In addition, the height of the deposition mound increases and then decreases as the skew angle rises for all tested spacings. These findings demonstrate that skew angle and pier interaction are key parameters governing local scour around twin bridge piers. The results provide useful quantitative guidance for bridge foundation design, scour prediction, and the assessment of river engineering measures under oblique-flow conditions.

KEYWORDS
Flow interference; Local scour; Pier spacing; Sediment mound; Skew angle; Twin bridge piers.

1. Introduction

Bridge piers significantly disturb the approaching flow and often become the focal point of local bed erosion in alluvial channels. Among the various hydraulic factors affecting bridge safety, local scour around piers has long been recognized as one of the primary causes of bridge damage and collapse worldwide. Numerous post-failure investigations have shown that a large proportion of bridge failures are associated with excessive scour at foundations, leading to severe economic losses and disruption of transportation networks.

Consequently, improving the understanding and prediction of pier scour has become a major focus in hydraulic and bridge engineering research [1–4].

Local scour develops when the approaching flow encounters a pier and generates complex three-dimensional flow structures near the bed. The downward flow in front of the pier and the formation of the horseshoe vortex system increase the local bed shear stress and promote sediment entrainment, gradually forming a scour hole around the foundation. Under clear-water conditions, the equilibrium scour depth is governed by several interacting parameters, including flow depth, flow intensity, sediment characteristics, and pier geometry. Because of this complexity, numerous experimental studies and predictive relationships have been proposed to estimate scour depth and evaluate the stability of bridge foundations, many of which continue to be widely used in engineering practice [5–8].

In practice, however, bridges are commonly supported by multiple piers. Flow interference between adjacent piers significantly alters vortex dynamics, scour-hole geometry, and sediment deposition patterns. Earlier studies primarily examined longitudinal (tandem) or transverse (side-by-side) spacing effects separately [9,10]. More recent experimental investigations have expanded this knowledge: side-by-side configurations under varying spacing [11], tandem and staggered arrangements of compound piles [12], non-uniform twin piers [13], staggered groups in gravel beds [14], and scour evolution around staggered double-cylinder piers [15]. Additional works have addressed side-by-side piers in curved channels under ice-covered conditions [16] and angled square pier groups [17]. These studies collectively demonstrate that pier interference can either amplify or reduce scour depending on spacing, alignment, and flow conditions, and have led to new predictive equations for specific configurations [11,18].

Despite these valuable contributions, a critical literature gap persists: few, if any, systematic experimental studies have simultaneously varied center-to-center spacing from $1D$ to $6D$ and skew angle from 0° (aligned) to 90° (transverse) for identical cylindrical twin piers under identical clear-water conditions. Most recent works focus on either fixed-spacing tandem/side-by-side setups or limited angle ranges, and rarely provide high-resolution three-dimensional scour topography or volumetric analysis across the full parameter space. This limitation restricts the understanding of horseshoe- and wake-vortex interaction mechanisms and reduces the applicability of findings to real multi-pier bridge design, where piers are often placed at oblique angles due to river morphology or structural constraints.

The present experimental study directly addresses this gap. Forty-two clear-water scour tests were conducted in a recirculating flume using identical cylindrical piers (diameter D). Twin cylindrical piers with diameter D were tested at six longitudinal spacings, characterized by a normalized spacing ratio S/D ranging from 1 to 6, and skew angles θ relative to the approach flow ranging from 0° to 90°. Equilibrium scour topography was measured at high spatial resolution with a point gauge and processed into three-dimensional surfaces using Surfer software to quantify maximum scour depth (upstream and downstream holes), hole dimensions (length and width), sediment mound characteristics, affected area, and scour volume.

Beyond the study of isolated piers, recent experimental efforts have increasingly focused on the complexities introduced by pier configurations, bed morphology, and environmental obstructions. For instance, the scour behavior around roughened pile groups have been investigated, particularly in the presence of material harvesting pits, highlighting how flow intensity and surface conditions influence the resulting bed topography [19]. Further research has explored the morphological evolution downstream of scour holes, specifically noting how upstream debris accumulation

significantly accelerates dune formation [20]. In addition, detailed mapping of scour evolution around grouped bridge piers under controlled hydraulic conditions has provided insights into the spatial distribution of bed erosion [21]. Recent studies have also evaluated the efficacy of mitigation measures, such as bed sills, in controlling the intensified scour caused by debris obstructions, demonstrating the sensitive balance between structural interventions and local flow dynamics [22]. These advancements underscore the importance of accounting for multi-pier interactions and external obstructions in scour prediction.

Local scour around bridge piers located in channel bends has attracted considerable attention in recent years because of the complex flow structures generated by channel curvature and secondary currents. In curved channels, the interaction between centrifugal forces, secondary flow, and the horseshoe vortex system around the pier can considerably intensify the scour process, particularly near the outer bank of the bend. Several recent experimental studies have investigated the influence of flow intensity, pier position, and pier arrangement on scour characteristics in sharp bends. Vaghefi et al. (2025) experimentally examined the effect of variations in the velocity ratio (U/Uc) on scour holes around vertical-inclined piers positioned within a sharp 180° bend [23]. Safaripour et al. (2025) analyzed streamlines around single and double piers with submerged vanes in a sharp U-shaped flume and demonstrated the significant influence of flow structures on scour development [24]. Furthermore, Eghbalnik et al. (2023) investigated the effects of triplex inclined-vertical group pier arrangements on scour hole characteristics in a sharp bend, while Moghaddassi et al. (2024) studied the combined effects of pier position and critical velocity ratio on scour patterns in two consecutive bends under clear-water conditions [25,26]. These studies emphasize the importance of bend-induced flow complexity in determining local scour behavior around bridge foundations.

Based on the limitations identified in previous studies, the present research provides several important contributions to the existing literature.

The main novelties of this study are as follows:

- Simultaneous investigation of skew angles (0°–90°) and spacing ratios (S/D = 1–6), whereas previous studies mostly examined these parameters separately.
- Three-dimensional analysis of scour morphology, including scour hole length, bed deformation, and deposition mound characteristics in addition to maximum scour depth.
- Providing new experimental evidence on the influence of skewed flow on scour intensity and erosion–deposition patterns around bridge piers.

Recent studies have provided further insight into hydraulic behavior, sediment transport, and local scour processes under different flow conditions and hydraulic configurations [27-30]. Despite these advances, the combined effects of skew angle and pier spacing on the three-dimensional morphology of scour around bridge piers have not yet been comprehensively investigated. Therefore, the present study experimentally examines the evolution of scour geometry under varying skew angles and spacing ratios.

The specific objectives are: (1) to quantify the combined influence of pier spacing and skew angle on the magnitude and three-dimensional geometry of local scour holes around twin cylindrical piers; (2) to elucidate the underlying vortex interaction mechanisms responsible for observed trends; (3) to generate a high-resolution dataset suitable for numerical model validation and development of improved design equations; and (4) to provide practical recommendations for optimal pier placement in new and existing bridges.

Results reveal strong non-linear interactions: at close spacings (1D-2D), increasing skew angle dramatically

amplifies scour through merged vortices, while at larger spacings, the effect of angle differs markedly between upstream and downstream piers. These findings extend and complement recent literature [11,15] and have direct implications for resilient bridge design under complex hydraulic conditions.

2. Materials and Methods

2.1. Experimental Facility

The experimental investigation was carried out in a recirculating rectangular laboratory flume. The flume is a concrete structure with a length of 15 m, a width of 0.6 m, and a depth of 0.6 m. The side walls of the flume are constructed of transparent materials to facilitate continuous side-view observation of the scour process and flow dynamics. A test section, specifically designed for sediment placement, was located approximately in the middle of the channel, allowing for a 4 m upstream approach length to ensure a fully developed turbulent flow. The test section itself was 2 m long and spanned the entire width of the flume. In order to minimize the influence of side-wall effects on the flow field and scour development, the piers were installed along the centerline of the flume. The channel width was selected to be sufficiently larger than the pier diameter, providing a large width-to-diameter ratio and reducing the possibility of wall-induced flow distortion. This configuration allowed the main flow structures responsible for local scour, including the horseshoe vortex and wake vortices, to develop properly around the piers.

A 4 m upstream distance was provided between the flow entrance and the test section to allow the approach flow to develop before reaching the model piers. Given the flume width of 0.6 m, this length corresponds to approximately 6.7 times the channel width, which is generally considered sufficient to achieve a reasonably developed turbulent flow in laboratory flumes [31,32]. Preliminary runs also indicated that the approaching flow was stable and uniform before entering the test section.

Flow discharge was supplied by a pump and was determined using a volumetric method. A tailgate situated at the downstream end of the flume was utilized to precisely control the flow depth.

The experiments were conducted in a rectangular flume. The schematic view of the experimental setup, including the arrangement of the twin piers, flow direction, and measurement grid, is illustrated in Figure 1.

The experiments were conducted under constant hydraulic and geometric conditions throughout all test runs. The flume dimensions, sediment characteristics, discharge, flow depth, and clear-water scour condition were maintained unchanged during the experiments. Therefore, Table 1 in section 2.3 summarizes only the principal experimental variables and measured scour parameters.

In the present study, a single flow condition and a uniform sediment size were selected to isolate the effects of skew angle and pier spacing on local scour characteristics. Keeping the hydraulic and sediment conditions constant allowed a clearer interpretation of the influence of the

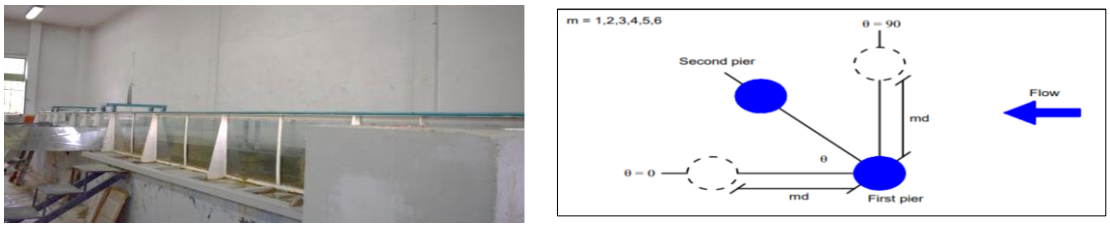


Figure 1.Schematic of the experimental setup showing the flume and twin cylindrical piers at variable spacing S and skew angle θ, flow direction.

investigated parameters on scour morphology. Although different flow intensities and sediment properties may affect the absolute scour dimensions, the observed trends are expected to remain qualitatively similar under comparable clear-water scour conditions. Future studies may extend the experiments to multiple flow and sediment conditions to further evaluate the general applicability of the results.

2.2. Sediment Characteristics

The working section of the flume was filled with a uniform, non-cohesive natural sand bed with a thickness of 13.5 cm. The physical properties of the sediment were determined through standard sieve analysis. The median grain size (d_{50}) was 1.6 mm. The geometric standard deviation of the particle size distribution, defined as $\sigma_g = \sqrt{d_{84}/d_{16}}$, ranged between 1.29 and 1.5. Since the sediment size distribution ($\sigma_g < 1.5$) the sediment was classified as uniform, effectively eliminating the influence of dynamic bed armoring during the scour process [7]. The specific gravity of sediment particles (G_s) was 2.65.

2.3. Pier Geometry and Test Configuration

Two identical cylindrical pipes with an external diameter of $D = 40$mm (0.04 m) were used as the bridge pier models. A pier diameter of 4 cm was adopted based on the flume dimensions and hydraulic conditions to ensure reliable development of local scour while minimizing wall interference effects. The selected diameter also allowed accurate measurement of scour geometry and was consistent with commonly used laboratory-scale pier dimensions reported in previous scour studies. The pier diameter was selected such that the flume width-to-pier diameter ratio ($B/D = 15$) was greater than 10, ensuring that flow contraction and side-wall boundary effects on the local scour development were practically eliminated.

To systematically investigate the interference effects, the twin piers were tested under various spatial configurations. The center-to-center spacing between the piers, S, was varied in increments of one pier diameter, corresponding to $S/D =$ 1,2,3,4,5,and 6. For each spacing, the skew angle (θ) of the twin-pier arrangement relative to the longitudinal direction of the approach flow was adjusted to $\theta \in \{0°, 15°, 30°, 45°, 60°, 90°\}$. The spacing ratios investigated in this study ranged from 1D to 6D in order to capture the transition from strong hydraulic interaction between adjacent piers to conditions approaching isolated-pier behavior. Spacing smaller than 1D was avoided because the two piers effectively act as a single obstruction, whereas at spacing ratios larger than 6D the interaction effects become considerably weaker and the scour characteristics tend toward those of isolated piers. A single isolated pier test was also conducted under the same hydraulic conditions to serve as a baseline for comparison. In total, 42 experimental runs were executed for the twin-pier configurations, plus additional tests for calibration and isolated pier conditions.

Under clear-water scour conditions, with the flow intensity set at the threshold of sediment motion, $V/V_c = 1$ to investigate the effect of spacing and skew angle on

Table 1.Main experimental variables and measured scour parameters

Parameter type	Symbol / Parameter	Values / Description
Independent variable	Longitudinal pier spacing, L/D	1, 2, 3, 4, 5, 6
Independent variable	Pier skew angle, θ (deg)	0, 15, 30, 45, 60, 75, 90
Response parameter	Maximum scour depth, ds	Measured after each experiment
Response parameter	Scour-hole length, Ls	Measured after each experiment
Response parameter	Scour-hole width, Ws	Measured after each experiment
Response parameter	Deposition mound height, Hd	Measured after each experiment

local scour around twin cylindrical piers. The experiments were conducted in a rectangular concrete flume with a uniform sediment bed having a median particle diameter of d_{50} = 1.6mm. The approach flow conditions corresponded to a Froude number of $Fr \approx 0.29$. The experiments were conducted in a rectangular laboratory flume with fixed geometric and hydraulic conditions. The flume dimensions, channel slope, sediment properties, and scour regime were kept constant throughout the experiments and are described in this section. Table 1 summarizes only the main experimental variables and parameters considered in the present study.

Table 1 summarizes only the main experimental variables and response parameters. Constant hydraulic and geometric conditions, including the flume dimensions, channel slope, sediment size, discharge, flow depth, and scour regime, are described in the Experimental Facility section.

2.4. Hydraulic Conditions

The experiments were conducted under clear-water scour conditions, which occur when the approach flow velocity is close to the critical velocity for sediment motion. The critical velocity (V_c) corresponding to the initiation of sediment movement was estimated based on sediment characteristics and flow conditions.

The flow velocity in the flume was gradually increased until the bed material showed the onset of particle movement, indicating the threshold condition for sediment entrainment. The approach velocity was then adjusted so that the velocity intensity ratio remained approximately equal to unity ($V/V_c \approx 1$), representing clear-water scour conditions near the threshold of sediment motion.

Maintaining this condition ensured that the observed scour was primarily generated by the flow–structure interaction around the bridge piers rather than by general sediment transport within the channel.

All experiments were conducted under clear-water scour conditions at the threshold of sediment motion. Clear-water scour conditions were ensured by maintaining the approach flow intensity below the threshold for initiation of sediment motion, consistent with the criterion $V/V_c < 1$, where V is the mean approach velocity and V_c is the critical velocity for the bed material [33,1]. The selected hydraulic conditions were defined with respect to the sediment size used in the experiments ($d_{50} = 1.6$ mm), so that no general bed transport occurred upstream of the test section. In addition, preliminary observations confirmed that sediment motion was absent in the approach reach and remained limited to the vicinity of the pier during the tests. Therefore, all experiments were conducted under clear-water scour conditions. To maximize the local scour depth without inducing general bed movement, the approach flow velocity (V) was systematically adjusted until it equaled the critical velocity for sediment entrainment (V_c). Thus, the velocity intensity was set precisely to $V/V_c \approx 1$. The flow depth (y_0) was maintained constant at 13.5 cm for all tests.

The experiments were carried out under clear-water scour conditions, i.e., the approach flow velocity was kept below the threshold of sediment motion. In each run, the sediment bed was initially at rest, so scour developed solely due to the local hydraulic action around the piers. The hydraulic conditions were selected to ensure that general bed movement did not occur during the tests.

In the present experiments, the Froude number was used as the primary hydraulic similarity parameter because it represents the balance between inertial and gravitational forces in open-channel flows. The experiments were conducted under a constant flow condition in order to isolate the effects of pier spacing and skew angle on local scour characteristics. Other parameters such as flow depth, sediment properties, and pier geometry were kept constant to maintain comparable clear-water scour conditions throughout the tests.

2.5. Experimental Procedure

Prior to each experiment, the sediment bed in the test section was carefully leveled to ensure a uniform initial condition. The twin cylindrical piers were then installed at the desired center-to-center spacing (S/D = 1–6) and skew angle relative to the approach flow (θ = 0°, 15°, 30°, 45°, 60°, and 90°).

Water discharge was gradually increased until the target hydraulic conditions were achieved. The flow depth was maintained constant at y = 0.135 m using an adjustable tailgate located at the downstream end of the flume.

All experiments were conducted under clear-water scour conditions at the threshold of sediment motion. Once the desired flow condition was established, the experiment was allowed to run continuously until the equilibrium scour state was reached.

Equilibrium scour conditions were assumed to be reached when the temporal variation in scour depth became negligible. In this study, equilibrium was defined as the condition in which the change in the maximum scour depth during a 24-hour observation period was less than or equal to 5% of the pier diameter (0.05D).

To determine the approximate equilibrium time, a preliminary long-duration experiment was conducted for a single isolated pier under the same hydraulic conditions. The results indicated that the rate of scour development significantly decreased after approximately 9 hours. Therefore, all experiments in the present study were conducted for a minimum duration of 9 hours to ensure that the scour process approached equilibrium conditions. Each experiment was continued until the scour process approached equilibrium conditions. Equilibrium scour was assumed when no noticeable change in scour depth was observed during an extended observation interval and the scour rate became very small. The temporal variation of scour depth generally exhibited a rapid initial increase followed by gradual stabilization, indicating the approach toward equilibrium conditions.

The selected test duration was based on a preliminary long-term experiment conducted under the same hydraulic conditions as the main tests, namely clear-water flow in a recirculating flume with a discharge of 28 L/s, a flow depth of 13.5 cm, and a Froude number of approximately 0.29. The bed material was uniform sand with $d_{50} = 1.6$mm. In this preliminary test, the rate of scour development decreased markedly after about 9 h, indicating that the scour process was approaching equilibrium. Accordingly, the main tests were conducted for at least 9 h. The equilibrium condition was defined as a 24 h change in the maximum scour depth not exceeding 5% of the pier diameter.

After completion of each test, the flow was slowly stopped and the bed topography around the piers was measured using a point gauge. The bed elevations were recorded over a measurement grid covering the scour hole and the surrounding deposition area.

After completion of each test, the flow was slowly stopped and the bed topography around the piers was measured using a point gauge. The bed elevations were recorded over a measurement grid covering the scour hole and the surrounding deposition area. To better illustrate the spatial characteristics of the scour hole and the deposition dune formed around the twin bridge piers, the measured bed elevations were interpolated using Surfer software to generate two-dimensional contour maps and three-dimensional surface plots of the bed morphology.

The collected data were then processed to generate three-dimensional representations of the scour morphology using Surfer software.

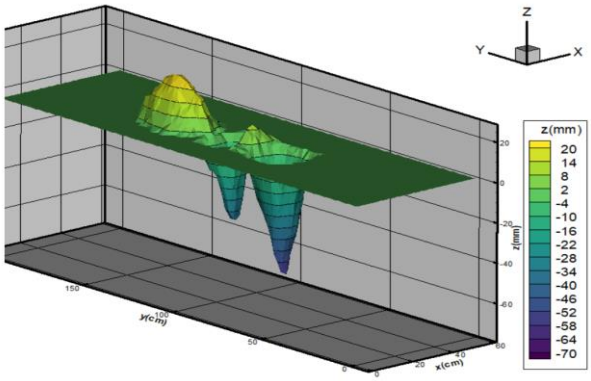


Figure 2.Three-dimensional bed morphology showing the scour hole and downstream deposition dune around the twin bridge piers under skewed-flow conditions.

The Figure 2 illustrates the spatial development of the scour hole and the downstream deposition dune for a representative experimental condition.

2.6. Dimensional analysis

To identify the governing parameters affecting local scour around the twin bridge piers, a dimensional analysis was performed using the Buckingham π theorem. The

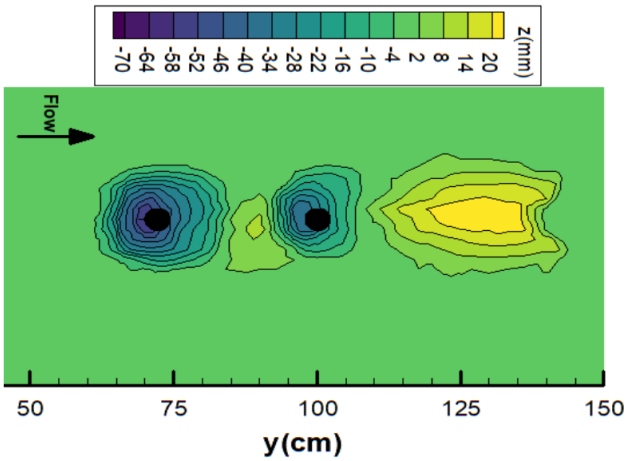


Figure 3.Two-dimensional contour map of bed elevation around the twin bridge piers generated from measured bed-profile data.

The contours lines (Figure 3) represent the bed elevation obtained from the measured bed profiles and interpolated using Surfer software, highlighting the scour hole and deposition patterns.

The use of contour and three-dimensional morphology visualization is consistent with previous scour investigations reported in the literature, such as studies on scour morphology around bridge piers subjected to debris accumulation [34].

equilibrium scour depth $d_s$can be expressed as a function of flow characteristics, sediment properties, and pier geometry:

$$d_s = f(U, y, \rho, \rho_s, g, d_{50}, D, S, \theta) \qquad (1)$$

where $U$is the approach flow velocity, $y$is the flow depth, $D$is the pier diameter, $S$is the spacing between the piers, $d_{50}$is the median sediment size, and $\theta$is the flow attack angle.

Applying dimensional analysis yields the following dimensionless relationship (2):

$$\frac{d_s}{D} = f\left(\frac{y}{D}, \frac{U}{\sqrt{gD}}, \frac{d_{50}}{D}, \frac{S}{D}, \theta\right) \quad (2)$$

In the present experiments, the pier diameter and sediment characteristics were kept constant, while the spacing ratio (S/D)and flow angle (θ)were systematically varied to investigate their effects on scour depth and bed morphology. In the present study, the spacing ratio (S/D) and flow attack angle were selected as the primary varying parameters.

3. Results & Discussion

This section presents the experimental results concerning the variations in scour topology around twin cylindrical piers. The quantitative analysis focuses on the maximum scour depth (d_s), scour hole geometry (length and width), and sediment deposition mound, evaluated across different pier spacings (S/D) and skew angles (θ).

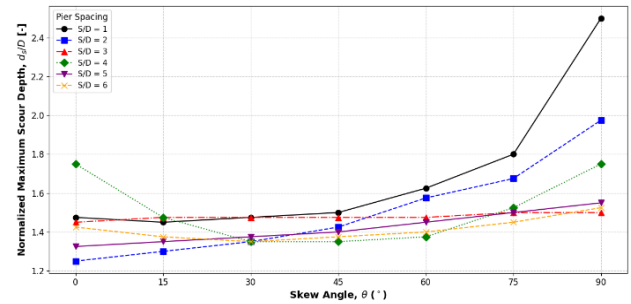
3.1. Maximum Scour Depth Analysis

The absolute maximum scour depth is a critical parameter for bridge safety. In twin-pier configurations, flow interference significantly alters the scouring capacity compared to a single pier.

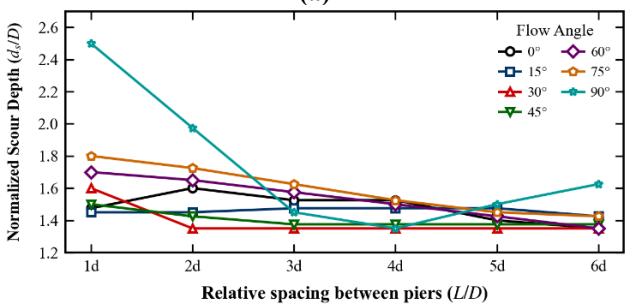
3.1.1. Upstream Pier Scour Characteristics

Figure 4 illustrates the variation of the normalized maximum scour depth (d_s/D) at the upstream pier. For a constant pier spacing, increasing the skew angle from 0° to 90° generally led to an increase in d_s/D. Conversely, at any constant skew angle, increasing the spacing (S/D from 1 to 6) resulted in a gradual decrease in the upstream scour depth.

Discussion: The increase in scour depth with higher skew angles at the upstream pier is primarily due to the broader projected area of the pier group intercepting the flow, which strengthens the primary horseshoe vortex. This observation is consistent with recent findings by Wang, et. Al. [35,44], who demonstrated that greater flow blockage in staggered arrangements amplifies the downflow energy at the leading pier. As spacing increases, the hydrodynamic independence of the upstream pier grows, reducing the "backwater" blockage effect caused by the downstream pier, which explains the slight



(a)



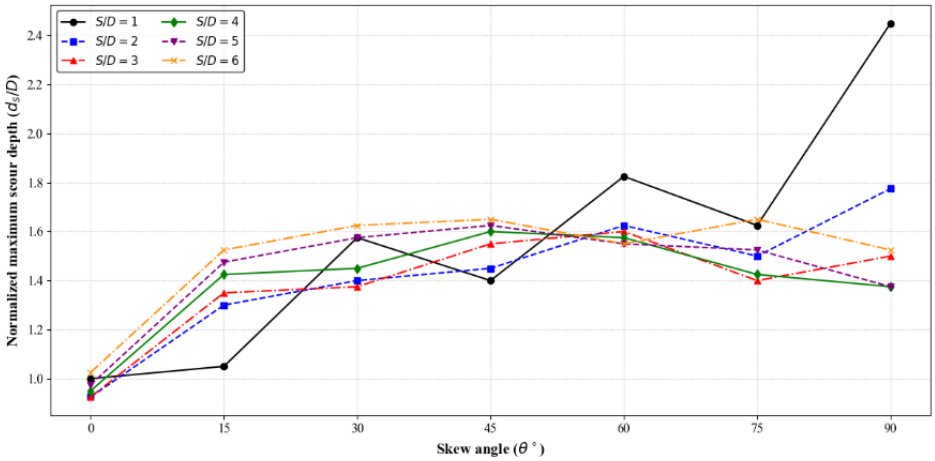
(b)

Figure 4.Variations of the normalized maximum scour depth (ds/D) at the upstream pier: (a) effect of increasing skew angle (θ) at constant pier spacings; (b) effect of increasing pier spacing (L/D) at constant skew angles.

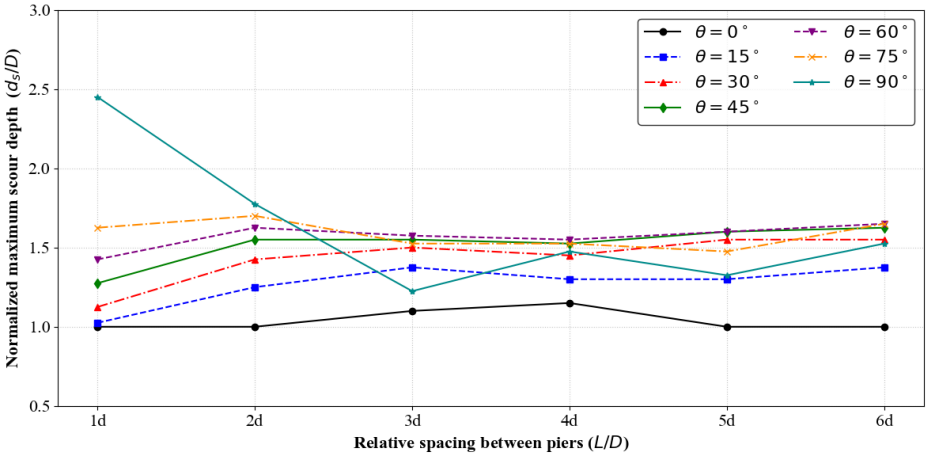
reduction in d_s/D at wider spacings.
For the smallest spacing ratio (S/D = 1), the two piers behave hydraulically as a nearly combined obstruction to the approaching flow. When the flow angle increases toward 75°–90°, the incoming flow directly impinges on the upstream pier while the narrow gap between the piers accelerates the flow and intensifies local turbulence. This condition strengthens the horseshoe vortex system and promotes interaction with wake vortices generated downstream of the upstream pier. The resulting concentration of bed shear stress around the pier base leads to a pronounced increase in scour depth compared with larger spacing ratios.

3.1.2. Downstream Pier Scour and Shielding Effect

The scouring behavior at the downstream pier (Figure 5) was found to be highly non-linear due to complex wake interactions. At tight spacings (S/D=1 and 2) and a 0° angle (tandem arrangement), the downstream pier experienced significantly less scour than the upstream pier due to the shielding effect. However, as the skew angle increased, the downstream pier moved out of the upstream wake region. For spacings larger than $3D$, the scour depth increased with the angle up to 60° but decreased for angles >60°. The non-linear variation of scour depth with spacing ratio indicates that the interaction between adjacent piers changes with pier



(a)



(b)

Figure 5. Variations of the normalized maximum scour depth (d_s/D) at the downstream pier: (a) effect of increasing skew angle (θ) at constant pier spacings; (b) effect of increasing pier spacing (S/D) at constant skew angles.

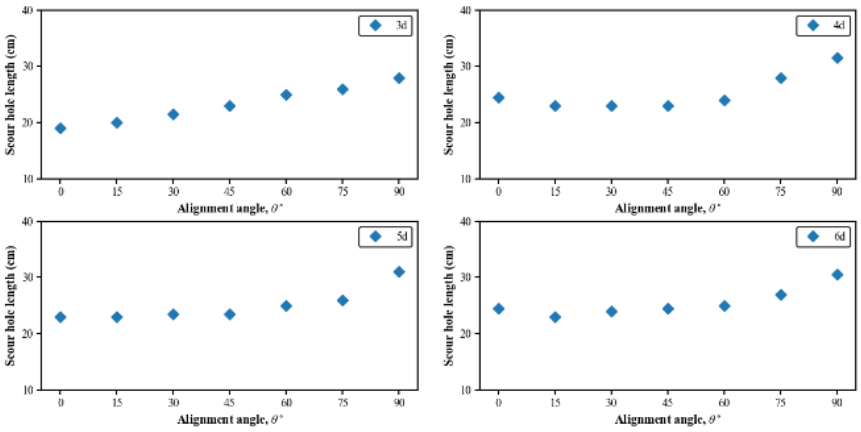
spacing. At smaller spacing ratios, stronger interaction between vortex systems enhances local turbulence intensity and sediment entrainment, increasing scour depth. Beyond a certain spacing, the interference effect weakens and the flow field progressively resembles that around isolated piers, resulting in reduced scour intensity.

Discussion: At intermediate angles (e.g., 15° to 45°) and wider spacings (S/D> 3), a critical flow phenomenon occurs: the flow accelerates as it is channeled between the gap of the twin piers. authors [36,37] recently highlighted this "gap flow channeling" effect, noting that the shed vortices from the upstream pier are swept directly toward the downstream pier, eroding its base more aggressively. This explains why, in the current study, the location of the absolute maximum scour shifted from the upstream pier to the downstream pier at intermediate angles and wider spacings.

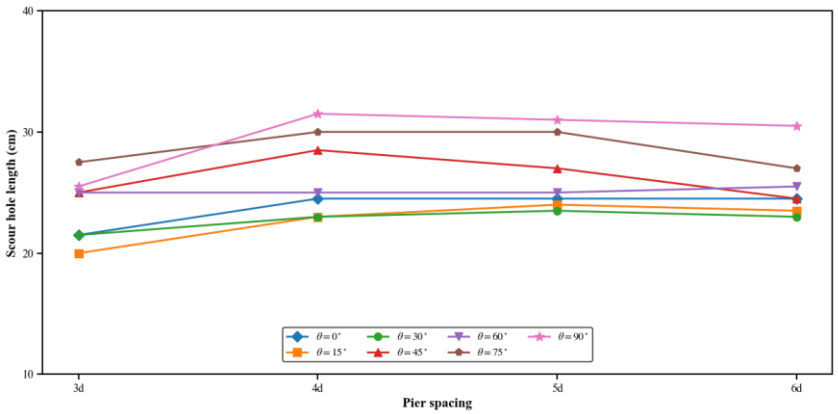
3.2. Scour Hole Morphology (Length and Width)

The spatial extent of the scour holes provides insight into the volume of eroded material. As shown in Figure 6, at narrow spacings ($S/D = 1$ and 2), the individual scour holes of the twin piers completely merged into a single, massive depression. The length and width of this combined hole increased continuously as the skew angle approached 90°.

Discussion: The merging of scour holes at $S/D \leq 2$ indicates that the horseshoe vortex of the downstream pier and the wake vortices of the upstream pier combine into a unified, highly turbulent erosive system. Recent experimental works by Majid and



(a)



(b)

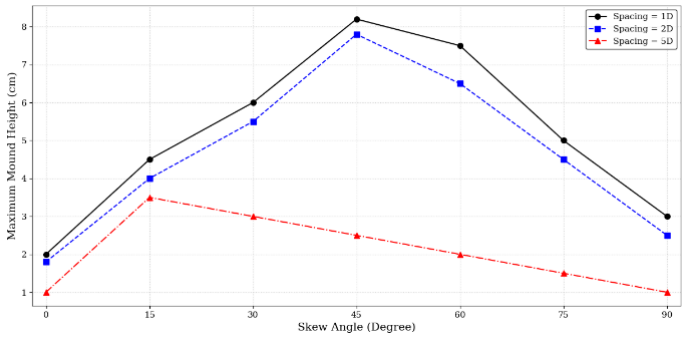
Figure 6.a) Variation of the upstream pier scour hole length with pier spacing for various skew angles. b) Variation of the upstream pier scour hole length with skew angle for different pier spacings.

Ahmad [38] corroborate this, showing that overlapping vortex systems at close proximity exponentially increase the scour hole dimensions. For wider spacings ($S/D \geq 4$), the holes separated, and the upstream scour hole dimensions became relatively stable, indicating diminished interference.

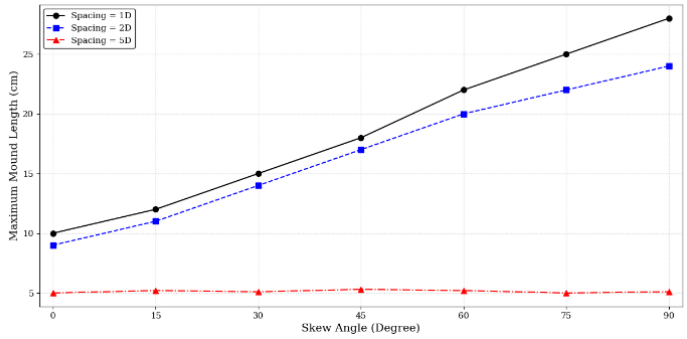
3.3. Sediment Deposition Mound Characteristics

The eroded sediment from the scour holes is transported and deposited downstream, forming a deposition mound (Figure 7). The experimental data revealed that the maximum height of the deposition mound consistently decreased with an increasing skew angle. However, the spatial extent (length and width) of the mound expanded with the skew angle up to intermediate spacings ($4D$ to $5D$).

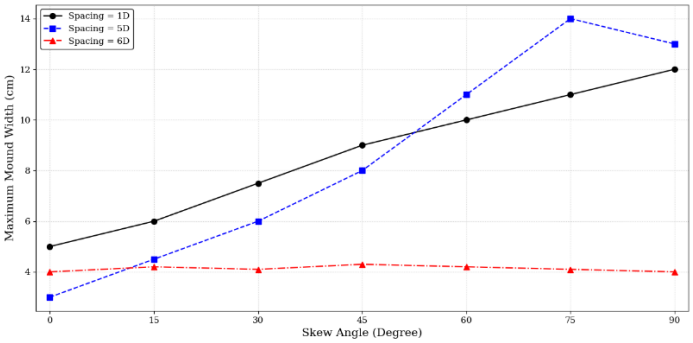
Discussion: The reduction in mound height at higher skew angles suggests a wider distribution of turbulent kinetic energy, which scatters the bedload material over a larger area rather than piling it into a steep dune. The absolute maximum mound dimensions were observed at extreme interference states (e.g., max length at S/D=1, Θ= 90°), underscoring the direct correlation between maximum flow



(a)



(b)



(c)

Figure 7. Variations of maximum sedimentation mound dimensions as a function of skew angle for different pier spacings ($S = 1D, 2D, 5D$: (a) height, (b) length, and (c) width.

blockage and maximum sediment displacement volume, a trend recently discussed in sediment transport models by Yao et al. [39].

At larger skew angles, the scour process appears to be influenced by both the modification of the horseshoe vortex system and stronger flow separation around the piers. The lateral approach flow produces asymmetric vortex structures and enhances downstream wake development, resulting in higher local bed shear stresses and increased sediment transport capacity. Consequently, deeper and more elongated scour holes were observed as the skew angle increased. The observed scour morphology is consistent with mechanisms previously reported for skewed bridge-pier flows.

3.4 Validation of the Experimental Results

To assess the reliability of the experimental observations, the obtained scour characteristics were compared with previously published studies and widely accepted scour prediction approaches for cylindrical bridge piers under clear-water conditions. Such comparisons are commonly used to verify the consistency of laboratory measurements with established hydraulic behavior [1,7].

In the present experiments, the normalized maximum scour depth around the upstream pier generally increased with increasing skew angle. This behavior is consistent with the findings of several previous studies which reported that flow obliquity intensifies the horseshoe vortex system and increases the local bed shear stress around bridge piers [32,33]. As the skew angle increases, the approaching flow interacts more strongly with the pier surface, producing stronger vortical structures and consequently deeper scour holes.

Furthermore, the experimental results indicate that increasing the spacing ratio between the twin piers (S/D) reduces the scour depth around the upstream pier. Similar trends have been reported by researchers investigating flow interference between multiple bridge piers, where close pier spacing amplifies turbulence and vortex interaction, while larger spacing weakens these interference effects [41].

The downstream pier exhibited significantly smaller scour depths at low spacing ratios (S/D = 1–2), which can be attributed to the sheltering effect produced by the upstream pier. This shielding phenomenon reduces the effective flow velocity and turbulence intensity reaching the downstream pier, leading to smaller scour holes. Comparable observations have been reported in experimental studies of tandem bridge piers under clear-water scour conditions [42,43].

Overall, the trends observed in the present study including the influence of skew angle, pier spacing, and flow interference show satisfactory agreement with previous laboratory investigations and established scour mechanisms reported in the literature. This agreement confirms the reliability of the experimental setup, measurement procedure, and the obtained scour data.

4. Conclusions

This study experimentally investigated the three-dimensional scour morphology around twin bridge piers subjected to skewed-flow conditions. The results revealed that flow obliquity significantly affects the development of local scour, the interaction of scour holes between adjacent piers, and the associated sediment deposition patterns. Under skewed approach flow, the scour geometry became increasingly asymmetric, while the location of maximum scour depth shifted toward the downstream side of the pier due to the redistribution of near-bed vortical structures and accelerated flow zones.

The contour maps and reconstructed three-dimensional bed surfaces clearly demonstrated the complex interaction between horseshoe vortices, wake vortices, and pier interference effects. The experiments further showed that the mutual interaction of the twin piers modifies the flow field and produces non-uniform scour

development that cannot be adequately represented using isolated-pier assumptions. The outcomes of this research provide useful reference data for improving the hydraulic design of bridge foundations in alluvial rivers. The findings are particularly relevant for bridge crossings where channel alignment, river curvature, or floodplain conditions generate oblique flow attack angles. Incorporating skew-angle effects into scour assessment procedures may therefore improve bridge safety and reduce the risk of foundation failure during extreme hydraulic events.

Future investigations are recommended to examine a broader range of hydraulic and geometric conditions, including different pier spacings, sediment gradations, flow intensities, and larger skew angles. The integration of laboratory measurements with advanced numerical simulations and field observations would further enhance the applicability of the present findings to prototype-scale river systems. Additional studies on scour countermeasures under skewed-flow conditions are also recommended to develop more reliable and cost-effective protection strategies for bridge infrastructure.

Acknowledgments

The authors would like to thank the Laboratory of Hydraulic Engineering at Bu-Ali Sina University for providing the facilities required to conduct this research.

References

1. Richardson EV, Davis SR. Evaluating scour at bridges. Washington (DC): Federal Highway Administration; 2001. Report No.: FHWA-NHI-01-001.
2. Lagasse PF, Zevenbergen LW, Schall JD, Clopper PE. Bridge scour and stream instability countermeasures: experience, selection, and design guidance. 3rd ed. Washington (DC): Federal Highway Administration; 2001. Report No.: FHWA-NHI-01-003.
3. Kim T, Park J, Lee S. Title of the 2025 article on scour or related topic. J Hydraul Eng. 2025;151(1).
4. Cristopher RA, Cook RA. Prediction of scour depth at bridge abutments. J Bridge Eng. 2014;19(5):04014004. https://doi.org/10.1061/(ASCE)BE.1943-5592.0000554
5. Rashno A, Eghbalzadeh A, Naserbegi A. Scour depth prediction around spur dikes using hybrid ANFIS methods. J Hydroinform. 2016;18(5):822-33. https://doi.org/10.2166/hydro.2016.128
6. Tena AF, Martín-Vide JP, Bladé E. Experimental study on the influence of pier shape on local scour. Water. 2021;13(4):490. https://doi.org/10.3390/w13040490
7. Melville BW, Coleman SE. Bridge scour. Highlands Ranch (CO): Water Resources Publications; 2000.
8. Ettema R, Melville BW, Barkdoll B. Scale effect in pier-scour experiments. J Hydraul Eng. 1998;124(6):639-42.
9. Hannah CR. Scour at pile groups. Christchurch (NZ): Department of Civil Engineering, University of Canterbury; 1978. Report No.: 28-3.
10. Keshavarzi A, Hamidifar H, Ball JE. Bed topography and local scour around twin bridge piers. Water. 2018;10(3):329. https://doi.org/10.3390/w10030329
11. Nandi B, Das S. Developing new equations for maximum scour depth near tandem, side-by-side, and eccentric piers. Can J Civ Eng. 2025;52(6):1030-44.
12. Duan B, Wang D, Qin C, Duan L. Local scour around marine structures: a comprehensive review of influencing factors, prediction methods, and future directions. Buildings. 2025;15(12):2125.
13. Ravanfar SM, Mohammadpour R, Sabzevari T. Experimental study of local scour around non-uniform twin piers. Int J River Basin Manag. 2023:1-16. https://doi.org/10.1080/15715124.2023.2167823
14. Anand A, Beg M. Local scour at group of bridge piers founded in gravel bed in

staggered arrangement. Results Eng. 2024;23:102608.
15. Yu P, Chen J, Xu S, Zhu L, Li J. Local scour evolution characteristics around staggered cylinder piers: numerical simulation based on the self-sustaining model. Ocean Eng. 2025;339:122043.
16. Song F, Wang J, Zhang Z, Cheng T, Li G, Sui J. Local scour around side-by-side double piers in channel bends under ice-covered conditions—an experimental study. Water. 2023;15(13):2317.
17. Yassein HAA, Al-Shukur AHK. Effect of side-by-side bridge pier shape on depth and configuration of local scour. Math Model Eng Probl. 2025;12(6).
18. Devi G, Kumar M, Bhardwaj A. A review on estimation methods of scour depth around bridge pier. In: River dynamics and flood hazards: studies on risk and mitigation. 2022. p. 189-201.
19. Sattariyan M, Daneshfaraz R, Alinejad B, Majedi-Asl M. Laboratory study of scouring around the roughened pile groups in the presence of material harvesting pits and at different Froude numbers. J Hydraul Struct. 2023;8(4):29-44.
20. Mahdian Khalili A, Akbari Dadamahalleh P, Hamidi M. Experimental evaluation of dune formation downstream of pier scour hole with upstream debris accumulation. J Hydraul Struct. 2024;10(1):13-28.
21. Majedi-Asl M, Kouhdaragh M, Fuladipanah M. Mapping scour depth around group bridge pier under controlled conditions. J Hydraul Struct. 2023;8(4):57-72.
22. Dadamahalleh PA, Hamidi M, Khalili AM. Bed sill effect on bridge pier scour with debris obstruction: an experimental investigation. Innov Infrastruct Solut. 2024;9(5):142.
23. Vaghefi M, Ben Mohammad Khajeh S, Safaripour N. Experimental study of the effect of changes in U/Uc on scour hole around vertical-inclined piers in various positions of a sharp 180-degree bend. Model Earth Syst Environ. 2025;11(1):11.
24. Safaripour N, Vaghefi M, Mahmoudi A. Experimental analysis of streamlines around single and double piers with submerged vanes in a sharp U-shaped flume. Adv Bridge Eng. 2025;6(1):13.
25. Eghbalnik L, Vaghefi M, Behroozi AM. Investigation of the effects of the arrangement of triplex inclined-vertical group piers in a sharp bend on the characteristics of scour holes. Iran J Sci Technol Trans Civ Eng. 2023;47(6):3989-97.
26. Moghaddassi N, Vaghefi M, Akbari M. Experimental study: effects of pier position and critical velocity ratio on scour pattern in two consecutive bends under clear water condition. Iran J Sci Technol Trans Civ Eng. 2024;48(5):3761-73.
27. Sattariyan M, Daneshfaraz R, Alinejad B, Majedi-Asl M. Laboratory study of scouring around the roughened pile groups in the presence of material harvesting pits and at different Froude numbers. J Hydraul Struct. 2023;8(4):29-44.
28. Daneshfaraz R, Nezafat H, Abbaszadeh H, Ebadzadeh P, Kuriqi A. Flow-sediment interaction and experimental design of screen plates for scour mitigation downstream of hydraulic structures. Water Pract Technol. 2026;21(2):555-74.
29. Daneshfaraz R, Rezaie M, Aminvash E, Mehrivar E, Sume V, Abraham J, et al. New generation scour control using nano Xanthan-clay composite for bed protection. Innov Infrastruct Solut. 2026;11(1):46.
30. Daneshfaraz R, Mehrivar E, Aminvash E, Rezaie M. Experimental investigation of scouring parameters of the downstream bed of simple and gabion rostral drops. AQUA Water Infrastruct Ecosyst Soc. 2025;74(4):335-48.
31. Chow VT. Open-channel hydraulics. New York (NY): McGraw-Hill; 1959.
32. Raudkivi AJ, Ettema R. Clear-water scour at cylindrical piers. J Hydraul Eng. 1983;109(3):338-50.
33. Melville BW, Coleman SE. Bridge scour. Highlands Ranch (CO): Water Resources Publications; 2000.

34. Khalili AM, Hamidi M, Dadamahalleh PA. Scour morphology around the bridge pier with upstream rectangular debris. In: Proc of 22nd Iranian Conference on Hydraulics; 2023 Nov; Maragheh, Iran. p. 8-9.
35. Wang H, Tang H, Liu X. Flow structure and local scour around tandem and staggered cylindrical piers. Ocean Eng. 2022;245:110464.
36. Zhang H, Chen Y, Li M. Gap flow channeling effect on local scour around twin bridge piers under steady clear-water flow. Coast Eng. 2023;180:104273.
37. Das R, Das S, Mazumdar A. Experimental study on local scour around twin circular piers. J Hydraul Res. 2020;58(4):629-44.
38. Majid ZA, Ahmad S. Experimental study on local scour around staggered and side-by-side bridge piers. J Hydraul Eng. 2021;147(4):04021008.
39. Yao W, Li J, Zhang Y. Sediment deposition and scour hole volume characteristics around complex bridge piers. Water Resour Res. 2021;57(8):e2020WR029415.
40. Vittal N, Kothyari UC, Haghighat M. Clear-water scour around bridge pier group. J Hydraul Eng. 1994;120(11):1309-18.
41. Kothyari UC, Hager WH, Oliveto G. Generalized approach for clear-water scour at bridge foundation elements. J Hydraul Eng. 2007;133(11):1229-40.
42. Hashemi L, Kashefipour SM, Ghomeshi M, Bahrami Yarahmadi M. An experimental investigation of the scour close to twin bridge piers under unsteady flow. Iran J Sci Technol Trans Civ Eng. 2025:1-19.
43. Ataie-Ashtiani B, Beheshti AA. Experimental investigation of clear-water local scour at pile groups. J Hydraul Eng. 2006;132(10):1100-4.
44. Wang C, Yu X, Liang F. A review of bridge scour: mechanism, estimation, monitoring and countermeasures. Nat Hazards. 2017;87(3):1881-906.

© 2026 by the authors. Licensee SCU, Ahvaz, Iran. This article is an open access article distributed under the terms and conditions of the Creative Commons Attribution 4.0 International (CC BY 4.0 license) (http://creativecommons.org/licenses/by/4.0/).

Reduction of Scour Around Bridge Piers using Combined Cylindrical Protector and Riprap

Ferdous Mirsalari [1], Mahmood Shafai Bejestan [*,1], Seyed Mahmoud Kashfipour [1], Mohammad Bahrami Yarahmadi [1] and Kheirollah Khademi [2]

1. Department of Hydraulic Structures, Faculty of Water and Environmental Engineering, Shahid Chamran University of Ahvaz, Ahvaz, Iran
2. Housing and Urban Development Research Center, Tehran, Iran.

***Corresponding Author:**
Mahmood Shafai Bejestan

Email: m-shafaeibejestan@scu.ac.ir
Received: 2026.05.06
Accepted: 2026.07.09
J. Hydraul. Struct., 12(4):91-103
DOI: 10.22055/jhs.2026.51695.1377

ABSTRACT

Local scour around bridge piers, especially during floods, can lead to bridge destruction. The usual method for controlling scour is to use rockfill around bridge footings. Despite proper design, the protective layer gradually becomes unstable and destroyed due to edge erosion. In this study, the use of cylindrical protector, which is a new method for controlling scour around the base, has been investigated to protect the riprap layer. Two series of experiments carried out. first, a control experiment (experiment A) was conducted using a cylindrical pier of 4.5cm in diameter without using any protection. Then, a cylindrical protector (CP) of 13.5 cm in diameter was used as pier protector (experiment B1), the results of which showed that the maximum scour depth decreased by 12.8% compared to experiment A. Subsequent tests included a 4.5 cm radius of riprap covering around the pier (Test B2), a 13.5 cm radius of riprap covering around the protective cylinder only (Test B3), and Test B4 with a 18 cm radius of riprap covering around the pier as well as the CP and was tested under the same flow conditions. The results of these experiments showed that the maximum scour depth was reduced by 81, 31, and 100 percent, respectively, compared to the Test A. The rocks particles were stable throughout the test and edge erosion was negligible. In Test B2, the gravel surface in front of the pier was depressed due to the extrusion of fine bed particles (0.7 mm in diameter) from the pores of the rocks, which was due to the lack of using a layer of filter between the rocks and the sand bed, but no edge erosion was observed. In Tests B2 and B4, negligible edge erosion was observed.

KEYWORDS

Hydraulics, protective cylinder, rock pile, scour, bridge foundation protection.

1. Introduction

Localized scour around bridge piers has been reported to be one of the main causes of bridge failure, with half of all bridge failures in the United States due to scour around bridge piers, and similar results have been reported in Europe and Asia as seen in [1], [2], [3], [4], [5] and [6]. Due to the importance of the issue and the need for prevention of damage, extensive studies have been conducted over the past three decades to find the maximum scour depth in order to predict the necessary measures for the stability of bridges under construction, and at the same time to find methods to stabilize or control (reduce) the scour depth around the piers of existing bridges.

Control methods aim to modify the flow pattern in a way that reduces the strength of the flow components that are the main cause of scour, including sacrificial piles, submerged plates or sills, and upstream diverters [7] and roughening bridge [8]. Stabilization methods that are most commonly used for existing bridges involve the use of materials that are placed on the riverbed around the foundation so that the bed material is not directly under the influence of the flow. These methods include techniques such as rock piles, concrete aprons, gabion mats, articulated concrete blocks, and geobags. Among these methods, riprap covering remains the most widely used measure due to its adaptability and cost-effectiveness over a wide range of hydraulic conditions as demonstrated in [9]. By reducing flow velocity and absorbing turbulence near the bed, riprap covering also acts as an energy dissipator, thereby limiting the development of localized scour as demonstrated in [10], [11] and [12]. If the riprap layer is well designed (including size, shape, grain size, type of arrangement, and appropriate filter), it can both protect the aggregates from erosion and prevent the penetration of the vertical component of velocity into the rock layer and the under washing of the riprap covering as stated by [3], [9], [10], [11], and [13]. However, in certain conditions, the riprap layer can lead to instability of the edge aggregates and sinking into the bed due to edge erosion (erosion of the sedimentary bed around the riprap layer), which, if continued, can lead to failure of the entire riprap layer [11]. A recent laboratory study was conducted by [14] on the effect of riprap covering around single, tandem, and stepped piers on a non-uniform moving bed under clear flow condition. They found that for a single pier, rock guarding eliminated local scour around the bridge pier but resulted in moderate edge scour downstream of the pier. And in all configurations, rock protection reduced the maximum scour depth by an average of 64–67%. A new riprap covering design to reducing bridge pier scour was studies by [6] in which they found that the new method can reduce the depth and volume of scour depth up to 81.0% and 92.3%, respectively, and it was found that quires 18% less riprap material. A new countermeasure including the roughening geometric elements (RGEs) made of materials like wood, plastic, or metal have been found to reduce the maximum scour depth of up to 35% compare to unprotected piers [8]. The combined countermeasures also have been successfully studied by researchers. Combination of collar and Geobag [15], combined riprap and collar [16], Combination of vertical slot and collar showed reduction of 100% in scour depth and combined use of collar plates and vanes as reported in [7].

In this regard, the present study investigates the combined effect of a permeable CP, as a new method of modifying flow pattern, and using riprap cover, as a method of riverbed reinforcement, on the maximum scour depth in front of a single bridge pier under clear water flow condition. By comparing the performance of different riprap covering arrangements around the bridge pier as well as the CP, the best arrangement is introduce.

2. Materials and Methods

2. 1. Experimental setup

The present study was conducted in the Physical Models Laboratory of the Faculty of Water and Environmental Engineering, Shahid Chamran University of Ahvaz, in a rectangular flume with a slope of 0.001, 10 meters long, 76 cm wide, and 60 cm high. The side walls of the flume are made of plexiglass and its skeleton is in metal. Figure (1) - a, schematic view of the flume, Figure (1) – b, view of the position of the stone lining, and Figure (1) - c, plan view of the riprap lining is shown.

The experiments were carried out with the presence of a pier in a 1.7 m long sedimentary bed located at a distance of 2.8 m from the beginning of the flume. The thickness of the sedimentary bed is 18 cm, which is filled with alluvial materials with

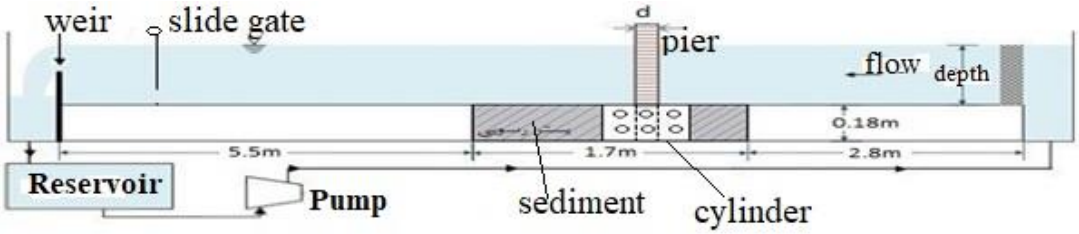
an average size of d_{50} = 0.7 mm. The size of the materials was chosen so that the bed form is not developed. In addition, the geometric standard deviation of the bed sediments ($\sigma = \sqrt{(d_{84}/d_{16})}$) is 1.22, which is consistent with the theory of [17] that the bed sediments are uniform.

In the present study, following the findings of [9] and [18] the basic parameters of the aggregate cover for bridge piers were considered, including the average diameter of aggregate stones (d_{50r}), the thickness of the aggregate layer, and the radius of the aggregate layer surface (b_r) around the pier. The average aggregate diameter (d_{50r}) was calculated using the following equation given in [7] and [18].

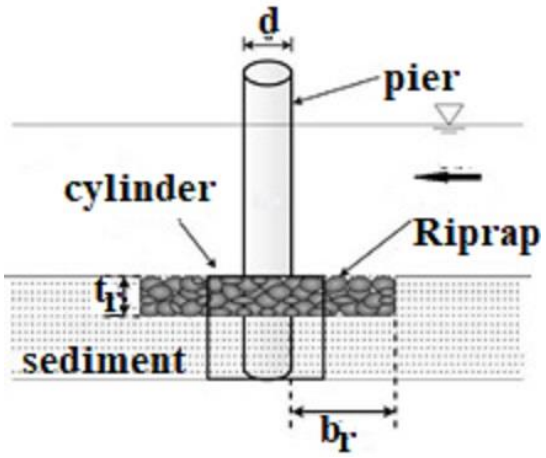
$$d_{50r}=0.692[kV^2/(S_g-1)g] \quad (1)$$

where, k is a coefficient that depends on the shape of the pier and is equal to 1.5 for a cylindrical pier, V is the average velocity of water flow (m/s), S_g is the specific gravity of aggregate (2.6), and g is the acceleration due to gravity (9.81 m/s^2). The experiments of this research were conducted at a constant flow discharge of 0.035 m3/sec and flow depth of 0.15 meters. As a result, considering the flume width (0.76 meters), the average flow velocity was determined to be 0.307 meters per second and by applying a safety factor of 1.2, the average diameter of the size of the stone for riprap layer was determined to be 4.4 mm. In order to prepare the desired granulation, sieves No. 4 and 5 with particle diameters of 4.75 and 4 mm were used. The riprap layer was placed with thickness of 8.8 mm, considering the recommended range of 2 to 3 times the average diameter of median stone size as demonstrated by [7], [12], [19] and [20], the experiments were conducted with three different arrangements of riprap cover with radii b_r = 4.5cm (inside the CP), 13.5 cm (around CP only) and 18 cm (around both pier and CP).

The flume water circulation system is a closed circuit, consisting of an underground tank, pump, valves and pipes. In all



a) Flume section view



b) View of pier CP and riprap layer



c) permeable cylinder(CP)

Figure 1. Experimental apparatus: a) section view of the flume b) View of pier, CP and riprap c) view of the CP

experiments, the constant inlet flow discharge was measured with an electromagnetic flow meter model Mega 3000 manufactured by Iran-Morad Company with an accuracy of 0.25%. At the beginning of the flume, there was a flow stilling tank that reduced the turbulence of the entering flow. At the end of the flume, there was a gate to control the flow depth within the flume. In selecting the diameter of the pier, the side effect of the width of the flume walls on the scour of the bridge pier should be considered. Therefore, according to the recommendation of [5], the ratio of the pier width to the channel width should be a maximum of 0.16. Also, according to the recommendations of [4] the maximum diameter of the pier should be equal to 10% of the flume width. Therefore, a diameter of 4.5 cm was chosen for the pier. Based on the recommendation of [21], two points were also considered for choosing the height of the pier. First, it should not be submerged in water and second, the height of the pier should be less than the flume height so as not obstruct the longitudinal movement of the bed profiler (an instrument for measuring the bed surface profile). Therefore, considering the height of the flume, the height of the pier was considered to be 52 cm (>33 and <60cm). The bridge pier made of Plexiglas was installed at a distance of 1.1 m from the beginning of the sedimentary bed (or 3.9 m from the beginning of the flume) so that a fully developed flow was established before the pier. In these experiments, a permeable CP made of galvanized sheet with a thickness of 0.7 mm, height of 18 cm (equal to the height of bed sediment) and diameter of 3d=13.5 cm with a circular mesh of 0.5 cm in diameter was made. To determine the depth and velocity of the flow, according to [4] and [5] and [18] in order to avoid the effects of the flow depth on the scour depth, the flow depth should be more than three times the width of the pier. Also, according to [18], when the average flow velocity is in the range $V_c > V$ in which V_c is the threshold flow velocity of the bed sediment (is equal to 0.3m/sec in this study), scouring occurs in clear water conditions and if the average flow velocity is more than the V_c, scouring occurs in live bed conditions. Therefore, to establish clear water conditions, initial experiments, without the presence of bridge pier, were conducted at a constant flow discharge and graduate lowering the flow depth to find out the threshold velocity of bed sediment particles. Therefore, the rest of experiments were conducted at a flow discharge of 35 l/s, flow depth of 15 cm, $V/V_c = 0.92$ and Froude number of 0.26.

2. 2 Experimental procedures

At the beginning of each experiment, the sediment surface was first leveled using an iron profile (iron can) measuring 2 × 4 × 280 cm and controlled by a Leica X310 laser meter with an accuracy of ±1 mm. To level the sediment surface, the upstream and downstream parts of the sediment surface were leveled by first tapping the sediment surface and then moving the iron can back and forth simultaneously on both sides. Then, the desired radius for placing riprap stones on the sediment bed was drawn and dug to the desired depth equal to the desired riprap thickness, and then the covering stones were placed around the bridge pier. Then, the sliding gate was completely closed and water entered the flume at a low flow discharge to prevent initial erosion which can make errors in the final scour depth. After a few minutes, the flow discharge was gradually increased till the desired flow discharge is reached and simultaneously the downstream gate was gradually opened till the flow depth reached 15cm. Once the flow was established the flow condition kept constant for few hours and during this time the flow discharge and flow depth was measured periodically and videotaped, using an endoscopic video camera, used to measure the maximum scour depth during the experiment inside the water flow. We also observed any possible movement of rock particles from the sides of the corner of riprap cover. After the experiment duration is over, the

pump was turned off and then the water inside the flume was gradually drained. when the bed sediments are dried enough, the riprap surface and bed topography was measured using a digital bed profiler with accuracy of ±0.001m. A laser meter also was used to determine the scour depth at specific point around the pier. Three-dimensional images and bed topographic maps as well as longitude and transvers bed profile were plotted using MATLAB software.

4. Results and Discussion

The main goal of this study is to investigate the effect of CP on stability of riprap cover. To achieve such goal, different experiments were conducted, as was presented in material and methods, then the maximum scour depth around the pier was measured and analyzed. The percentage variation in maximum scour depth for different arrangements of experiment compare to the control experiment (Experiment A) was calculated using the following equation.

$$R= [(d_{s1}- d_{s2})/d_{s1}] \times 100 \quad (2)$$

In this relation, d_{s1} and d_{s2} are the maximum scour depth for Experiment A and for other Experiments (B1, B2, or B3).

4.1. Experiment A

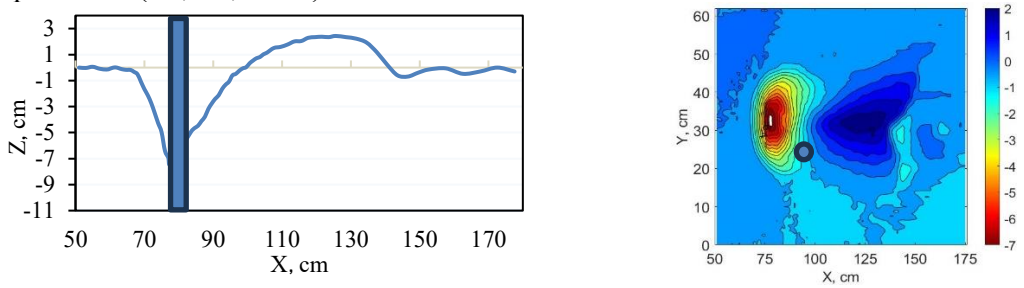
This experiment was conducted to monitor the movement of sediment particles in the vicinity of the bridge pier. The maximum measured scour depth in the front of the pier was used for comparison with the results of other experiments. In this experiment, the scour process started at the initial moments of the experiment and rapidly expanded with the formation of horseshoe vortices. The scour process began symmetrically with respect to the pier axis and sediments were gradually washed from the front and around the pier and accumulated at a short distance downstream of the pier. With the passage of time, the rate of change of scour depth decreased significantly and the scour hole reached almost unchangeable. The duration of this experiment was 12 hours. Figure 2 shows a picture before and after the end of Experiment A.



a) before test b) after test

Figure 2. Bed topography a) before and b) after Experiment A

Figure (3) shows the erosion and sedimentation status of the bed in the Experiment A. In this experiment, the maximum depth of the scour hole closed to the front of the pier was measured to be 7.8 cm.



a) longitudinal bed profile b) bed topography

Figure 3. longitudinal bed profile and bed topography after Experiment A

4.2. Permeable CP Without riprap (Experiment B1)

Recently, CP, as a new measure to control scour around the pier, has been introduced by [22]. Therefore, in this experiment, a permeable CP around the pier was installed so its top lip is at the bed level. Figure 4 shows the conditions before and after the test.

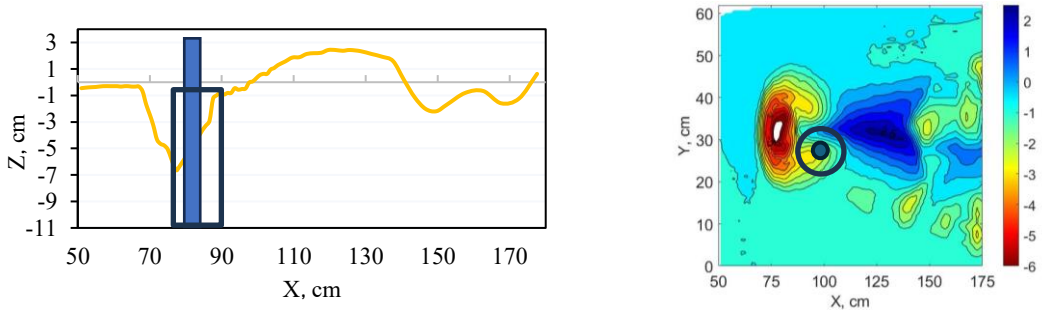
In this experiment, the maximum depth of the scour hole was measured to be 6.8 cm. The installation of the CP reduced the maximum scour depth by 12.8% compared to the Experiment A without CP. Figure (5) shows the longitudinal profile of the sedimentary bed topography in the experiment with CP. This figure also shows the position of the bridge pier and the CP.

The reason for the reduction in the scour depth around the pier can also be stated as follows. The longitudinal flow, when hitting the pier and reduce its kinetic energy, and as a result, creating a reverse pressure gradient, forms a downward vertical flow velocity component in front and sides of the pier, which changes its direction upward when it hits the bed and lifts sediment particles. At the same time, a spiral-shaped flow is formed from the intersection of the downward velocity component and the longitudinal component of the flow velocity. The lifted sediment particles are trapped in this spiral flow and transported downstream. However, due to the presence of CP, firstly, the strength of the spiral flow is reduced, and secondly, these particles are deposited inside the CP. Also, the presence of CP will cause the wake vortex to shift away from behind the pier further downstream, resulting in less scour behind the pier. As seen in Fig.6 During the experiment, erosion of bed material around the CP also is visible (Fig. 6b). However, no edge erosion of the riprap cover can be observed. This is because the rocks are completely compact inside in the CP. Maximum scour in front of CP (maximum of 5.9cm in this experiment) compare to the scour around bridge is about 15% less, although the CD diameter is 4.5 times pier diameter. This is because the maximum height of CP above the bed (5.9 cm) is low compare the pier height (15 cm) and since the near bed flow velocity which attack the CP is low, the strength of downward velocity component is low enough and thus scouring around the CP is low. The results of this study have shown that CP alone, can only reduce the scour depth up to 12.8%. In addition, as can be seen in Fig, 4b, although scouring occurs around the CP although less, it may eventually cause failure of the CP and or bridge pier. Therefore, the present study's aim is to investigate the combined CP with riprap to improve the application of CP for the sake of safety.



a) before test **b) after test**

Figure 4. Bed condition a) before and b) after Experiment B1



a) longitudinal bed profile **b) bed topography**

Figure 5. longitudinal bed profile and bed topography after Experiment B1

4.3. Combined CP and riprap, b_r = 4.5 cm (Experiment B2)

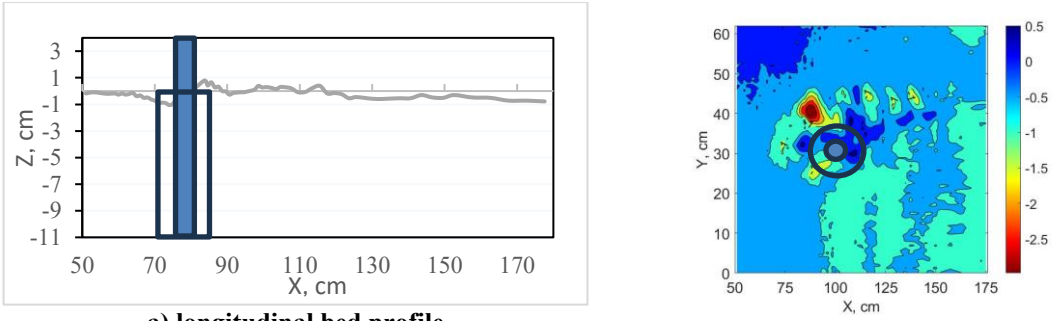
The bed conditions in this experiment before and after the test are shown in Figure 6.

At the end of this experiment, the surface of the stone in front of the pier was lowered by 1.5 cm compared to the control condition without stone. During the experiment, the aggregates did not move around the pier, although a few aggregates had slight jumps, but no horizontal movement was observed. The reason for the decrease in the level of the gravel surface can also be caused by the escape of fine bed particles through the pores of the gravel particles because no filter was used in this experiment. In practice the riprap may failed due to undermining which this type of failure which is called winnowing failure. However, if a suitable filter is used between the gravel layer and the sedimentary bed, it will not be possible for the bed sedimentary particles to escape through the riprap's pores, and practically the level of riprap surface around the pier will remain stable. By comparing with the control test, placing this riprap cover has reduced the maximum scour depth by 81%. Fig. 7b also shows that scour around CP is much lower than in Experiment B1. Figure (7) shows the longitudinal profile of the sedimentary bed and the topography of the sedimentary bed around the pier and CP.



a) before experiment **b) after experiment**

Figure 6. Bed conditions a) before and b) after Experiment B2



a) longitudinal bed profile **b) bed topography**

Figure 7. longitudinal bed profile and bed topography after Experiment B2

The main reason for the reduction of scouring depth was due to the stone covering around the pier, which were designed in the right size and the stone particles did not move. In addition, the presence of aggregates causes the strength of the vertical component to decrease when it reaches the sedimentary bed, and the roughness of the aggregates leads to a decrease in the strength of the spiral flow around the foundation, which reduces the amount of sedimentary particle transport. These factors have also helped to reduce the amount of scour around the CP, so that when compared with the Experiment A, the amount of maximum scour depth 81% reduction. One of the advantages of using CP is, that the riprap material cannot escape from the CP by edge erosion. In comparison with other study [5], the new methods, need less riprap material with almost the same performance.

4.4. Combined CP and Riprap only around the CP, b_r=13.5cm (Experiment B3)

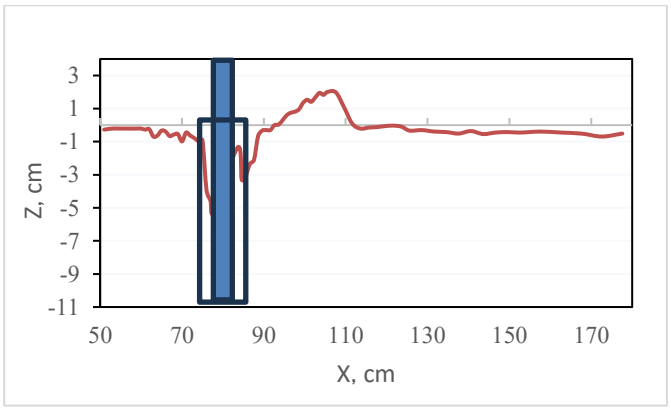
The conditions of this experiment are shown in Figure 8. The layer of crushed stone is placed only around the CP with b_r=13.5cm.

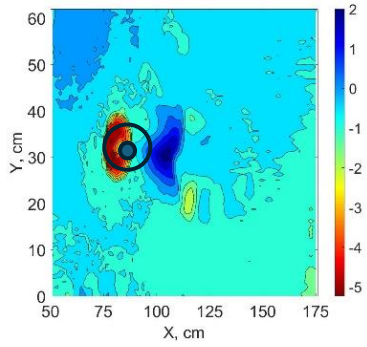
As it is clear from Figure 8, at the end of the experiment, scouring occurred around the pier inside the CP, and the maximum depth of the hole was measured as 5.4 cm in front of the pier. Compared to the Experiment A, the maximum scour depth has decreased by 31%. Figure (9) shows the longitudinal profile of the sedimentary bed and the leveling curves of the sedimentary bed of this experiment.



a) before experiment **b) during experiment** **c) after experiment**

Figure 8. Bed conditions a) before experiment, b) during Experiment and c) after Experiment





a) longitudinal bed profile **b) bed topography**

Figure 9. longitudinal bed profile and bed topography after Experiment B3

The reduction of scouring depth around the pier inside the cylinder by 31% compared to Experiment A, can be due to the decrease in the strength of the vortices due to the presence of roughness caused by the aggregates around the protective cylinder. As it is clear from Figure 8b, the transported sediment is deposited downstream of the CP and on top of the riprap layer. In addition, it can be seen that the bed sediments at the edge of the protective layer have slightly eroded and created a small groove. Comparing experiment B1 with experiment B2 shows that the effect of placing riprap inside the cylinder has a greater effect on reducing the scour depth around the pier, while placing riprap around the cylinder, protects the bed scour around the CP. Therefore, experiment B4 was conducted.

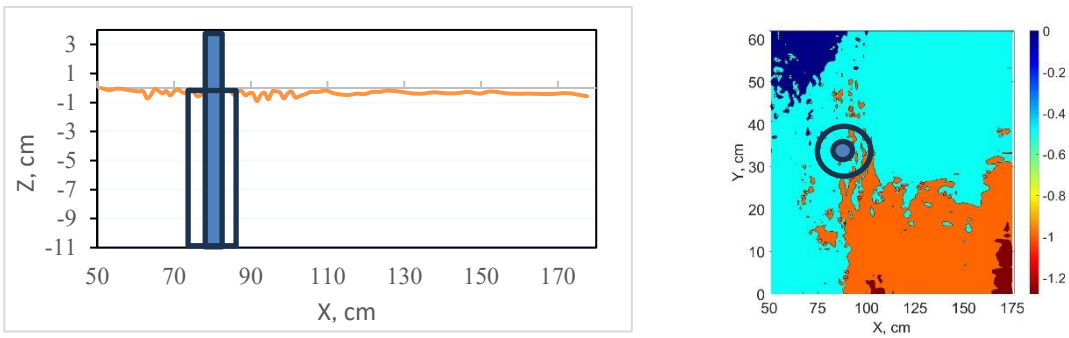


a) before experiment **b) after experiment**

Figure 10. Bed conditions a) before and b) after Experiment B4

4.5. Combined CP and Riprap br=18cm (Test B4)

In this experiment, the stone were placed both inside and around CP. The radius of the covering was 18 cm. The stone surface was the same level as the bed surface. No movement of the stone was observed during the experiment. Figure 10 shows the conditions before and after the experiment. The initial surface of riprap was the same before and after the test. Placing this covering alternative with stone completely eliminated local scour and ensured bed stability both around bridge pier and CP. Little scour downstream of the riprap layer can be observed. Although no edge movement of riprap material is visible here, further scouring can the riprap material to be unstable and collapse into the scour hole which the failure of riprap material may continue till reaches the around CP. In such cases, the riprap movement stopped by CP whilst the riprap inside the CP can safely protect the pier. In Figure (11) - the longitudinal bed topography at the end of the Experiment B4 is shown.



a) longitudinal bed profile **b) bed topography**

Figure 11. longitudinal bed profile and bed topography after Experiment B4

In this arrangement, due to the flow passing over surface area of the crushed stone layer around the pier and CP, the velocity of the flow impinging on the pier and CP decreased, as a result, the strength of the downward and horseshoe vortex decreased compared to the Experiment A.

Although the effect of CP in this experiment is not apparent, as can be seen from the Figure 10b, no particle has moved from around the pier and of course, this is due to the presence of CP. Because in cases of riprap without CP, due to the presence of strong vortices around the pier, finer aggregates can jump upwards and be transported downstream by the spiral vortex. The continuation of these conditions will create larger pores around the pier and ultimately destroy the riprap layer. Whereas as shown in Experiment B1, the stone inside CP are more tightly packed within the CP and cannot move easily. Therefore, the scour depth does not occur.

Table (1) shows the percentage reduction in scour depth around the pier in different alternatives of the riprap coverage in comparison with the Experiment A. Figure 12 shows the effect of combined CP and riprap on the longitudinal profile of the bed. This figure clearly show the reduction of the scour in front of the bridge pier with the installation of CP and the riprap compared to the control experiment (Exp. A). The minimum scour depth around the pier is related to experiment B4 and the highest scour depth is related to experiment B1 (CP without stone cover).

5. Comparison with other studies

Although similar to this study, the use of combination of CP and riprap, has not been published so far (at least to the authors' knowledge), the closest and most recent study on rockfill arrangement types was conducted by [14], where the results of the study are compared with this study, which are shown in Figure 10. According to the diagram in Figure 13 around a CP, with an increase in the ratio of rockfill coverage around the pier to the its diameter (br/d), the percentage of reduction in scour depth around the pier first increases and then with an increase in this ratio, the percentage of reduction will be insignificant. As can be seen, at a b_r/d ratio of 5 according to the results of [14] and the results of 4 experiments of this study, the percentage of reduction is maximized and the coverage radius no longer needs to be more than four times the pier diameter. In this coverage, the possibility of destruction of the rockfill layer due to edge erosion is also minimized.

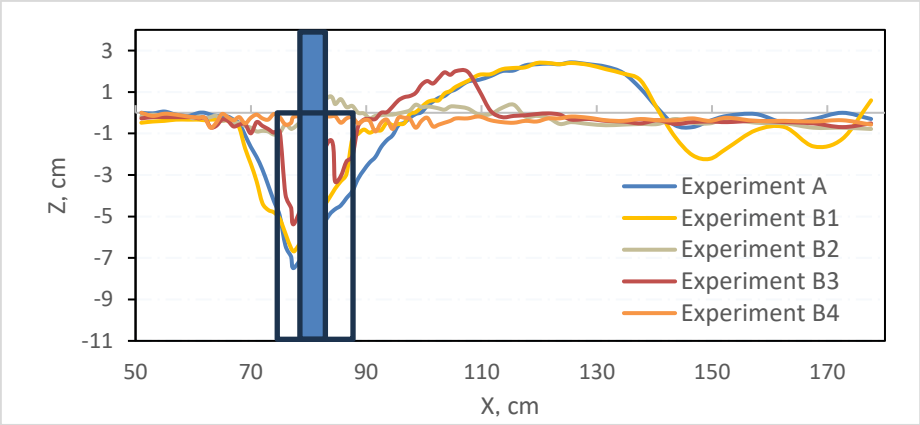


Figure 12. The longitude bed profiles for different experiment

Table 1. Percent reduction of scour depth around pier for different experiments

Experiment B4	Experiment B3	Experiment B2	Experiment B1	Test name
100	31	81	12.8	Percent reduction

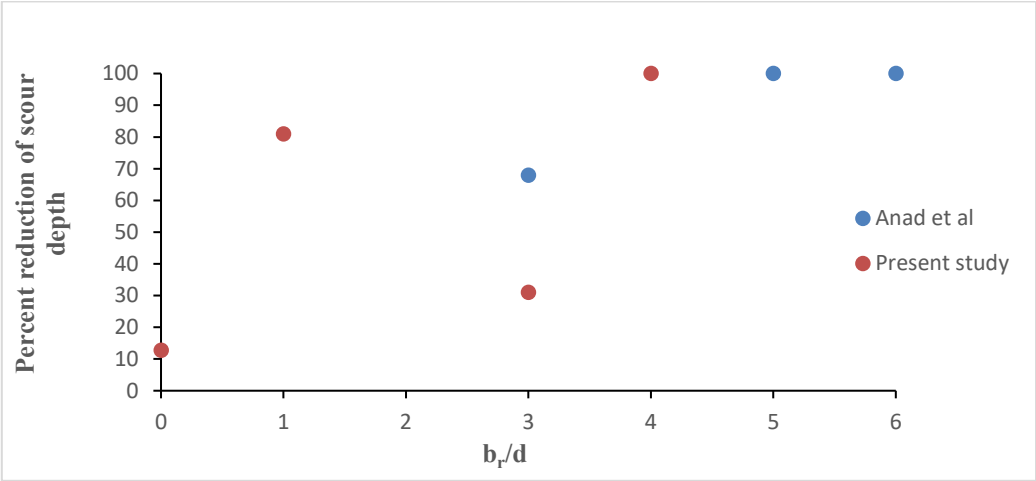


Figure 13. Percent reduction of scour depth around pier versus the ratio of $\frac{b_r}{d}$

6. Conclusion

In this study, the effect of combined installation of cylindrical protective and riprap layer on reducing the maximum scour depth around the pier bridge was investigated. The results show that although the installation of CP alone leads to a reduction in the maximum scour depth of 12.8 percent, the combined use of the CP and riprap can be more efficient. Three riprap arrangements with coverage of a) $b_r/d=1$ (inside the CP), b) $b_r/d=3$ (around the CP), and c) $b_r/d=4$ (around both pier and CP) reduced the maximum scour depth by 81, 31, and 100 %, respectively. The results also showed that the maximum cover radius of riprap layer should not be more than four times the diameter of the pier. In this condition, the amount of damage to the riprap layer from edge erosion is also minimized.

It is notable that riprap particles are quite dense inside CP cause the stone particles not to washed away especially the smaller particles which are close to the pier. In case of riprap without CP, the smaller particles are subject to the down flow velocity component and helicoidal vortices as well as wake vortex and can escape which eventually large pores are developed result in riprap failure due to winnowing. In addition, for the case of riprap without CP, once the edge erosion initiated and move toward the pier causing bridge failure. While for the case of presence of CP, the edge erosion will stop once it reaches to the CP and therefore, the bridge pier will be safe enough.

It should be noted that this paper presents a study with some limitation to introduce a new combined countermeasure against bridge pier scour. Despite the limitations of this study, the use of a combination of protective cylinders and riprap is very promising in reducing scour depth and ensuring bridge pier stability. However, before the results of this research can be used in the field, more studies with larger scales, different flow conditions, different shape and diameter of the pier and shape of CP should be conducted.

Acknowledgements

This research was conducted with financial support from the second author's research grant No. SCU1404.470 and the Khuzestan water Power Authority (KWPA). The Vice Chancellor for Research, Shahid Chamran University of Ahvaz and the director of the research of KWPA are hereby thanked for providing financial support.

Conflict of Interest

The authors declare that they have no conflict of interest.

Author Contributions

All authors contributed to the study conception and design. Material preparation, data collection, and analysis were performed by [M.SH.], [F.M.], [S.M.K], [M.B.Y.] and [K.K.]. The first draft of the manuscript was written by [M.SH.] and all authors commented on previous versions of the manuscript. All authors read and approved the final manuscript.

References

1. Harasti A, Gilja G, Potočki K, Lacko M. Scour at bridge piers protected by the riprap sloping structure: A review. Water. 2021; 13(24): 3606. https://doi.org/10.3390/w13243606
2. Kothyari UC, Garde RJ, Ranga Raju KG. Temporal variation of scour around circular bridge piers. J Hydraul Eng. 1992; 118(8): 1091-106.
3. Melville BW, Coleman SE. Bridge scour. Water Resources Publications. 2000; 550p.
4. Nohani E, Shafai Bejestan M. Experimental study on the stability of riprap at bridge piers in a 180 degree flume bend. Contemporary Engineering sciences. 2012; 5(8): 381-93.
5. Richardson EV, Davis SR. Evaluating scour at bridges (HEC-18). U.S. Federal Highway administration. Washington, D C. 2001.
6. Wardhana K, Hadipriono FC. Analysis of recent bridge failures in the United States. J Perform Constr Facil. 2003; 17 (3): 144-50.
7. Behera RK, Padhi E, Singhal GD. Recent trends in local scour countermeasure for bridge pier. Engineering Science and Technology, an International Journal. 2026; 77: 102367. https://doi.org/10.1016/j.jestch.2026.102367
8. Ahmad A, Khan M, Ajmal M, Sher S, Waseem M, Baig F. Potential of roughening geometric elements as bridge pier local scour countermeasures. Scientific Reports. 2025; 15(1): 8000. https://doi.org/10.1038/s41598-025-92410-0.
9. Melville BW, Sutherland AJ. Design method for local scour at bridge piers. J Hydraul Eng. 1988; 114 (10): 1210-26.
10. Croad RN. Protection from scour of bridge piers using riprap. Transfund New Zealand Research Report No. 82. 1997; 53p.http://worldcat.org/isbn/0478105401
11. Lim FH, Chiew YM. Parametric study of riprap failure around bridge piers. J Hydraul Res. 2001; 39 (1): 61-72. https://doi.org/10.1080/00221680109499803
12. Parola AC. Stability of riprap at bridge piers. J Hydraul Eng. 1993; 119(10): 1080-93. https://doi.org/10.1061/(ASCE)0733-9429(1993)119:10(1080)
13. Valela C, Whittaker CN, Rennie CD, Nistor I, Melville BW. Novel riprap structure for improved bridge pier scour protection. J Hydraul Eng. 2022; 148(3): 04022002. https://doi.org/10.1061/(ASCE)HY.1943-7900.0001967
14. Anand M, Timbadiya PV, Patel PL. Effectiveness of riprap protection for tandem and staggered bridge piers on non-uniform sediment bed. Ocean Engineering. 2026 363 part 2, article 126667, Doi:10.1016/j.oceaneng.2026.126667
15. Akib S, Liana Mamat N, Basser H, Jahangirzadeh A. Reducing local scouring at bridge piles using collars and geobags. Scientific World Journal. 2014; 128635. https://doi.org/10.1155/2014/128635
16. Zarrati AR, Nazariha M, Mashahir MB. Reduction of local scour in the vicinity of bridge pier groups using collars and riprap. J Hydraul Eng. 2006; 132 (2): 154-62.
17. Dey S. Fluvial hydrodynamics. Springer New York. 2024; 893p.
18. Lagasse PF, Zevenbergen LW, Schall JD, Clopper PE. Bridge scour and stream instability countermeasures: experience, selection, and design guidance: third edition. FHWA-NHI-01-003. 2001.
19. Chiew YM, Lim SY. Failure behavior of riprap layer at bridge piers under live-bed conditions. J Hydraul Eng. 2000; 126(1): 43-55.

20. Lauchlan CS, Melville BW. Riprap protection at bridge piers. J Hydraul Eng. 2001; 127(5): 412-18. DOI: 10.1061/(ASCE)0733-9429(2001)127:5(412)
21. Raudkivi AJ, Ettema R. Clear-water scour at cylindrical piers. J Hydraul Eng. 1983; 109 (3): 338-50.
22. Mirsalari F, Shafaei Bajestan M, Kashfipour SM, Bahrami Yarahmadi M, Khademi Kh. Investigating the efficiency of a new cylindrical structure measure aimed at controlling bridge pier scour. Journal of New Approaches in Water Engineering and Environment. 2026; under publication.



© 2026 by the authors. Licensee SCU, Ahvaz, Iran. This article is an open access article distributed under the terms and conditions of the Creative Commons Attribution 4.0 International (CC BY 4.0 license) (http://creativecommons.org/licenses/by/4.0/).

Journal of Hydraulic Structures

Volume 12 – Issue 4 – October 2026

Contents:

01 Local scour downstream of compound weirs under free and submerged flow conditions

Mohamed Abdelrazek Zidan; Ahmed Abouelfetouh; Ahmed Shwaky; Tarek Hemdan; Fahmy Abdelhaleem

14 Meander Bend Evolution and Bank Erosion Modeling of a reach of Brahmaputra River, India using MIKE 21C Model

Kuldeep Pareta; Upasana Pareta

42 Optimization of Static Operating Rule curves for Gated Spillways of Dams Under Flood Conditions

Mohammadreza Masoudimoghaddam; Saman Espahbodinia; Jafar Yazdi; Maedeh Behifar, Jamal Aghayari

60 Risk Analysis of Internal Erosion in Earth Dams Considering Uncertainties in the Permeability Coefficient of Materials

Samane Manafi; Jafar Yazdi

75 Experimental Investigation of Local Scour Around Twin Cylindrical Bridge Piers: Effects of Pier Spacing and Skew Angle

Morteza Shokri; AmirHossein Topal; Majid Fazli

91 Reduction of Scour Around Bridge Piers using Combined Cylindrical Protector and Riprap

Ferdous Mirsalari; Mahmood S. Bajestan; Seyed Mahmood Kashefipour; Mohammad Bahrami Yarahmadi; Kheirollah Khodemi

Shahid Chamran University of Ahvaz